Estimating PM2.5 Concentrations Using 3 km MODIS AOD Products: A Case Study in British Columbia, Canada

by

Yue Gu

A thesis
presented to the University of Waterloo
in fulfillment of the
thesis requirement for the degree of
Master of Science
in
Geography

Waterloo, Ontario, Canada, 2019

AUTHOR'S DECLARATION

I hereby declare that I am the sole author of this thesis. This is a true copy of the thesis, including any required final revisions, as accepted by my examiners.

I understand that my thesis may be made electronically available to the public.

Abstract

PM2.5 refers to fine particles with diameters smaller than 2.5 μm. The rising level of PM2.5 reveals adverse effects on climate change, economic losses, international conflicts, and public health. Exposure to the high level of PM2.5 would increase the risk of premature death, especially for people with weak immune systems, such as children and elder people. The main sources of PM2.5 include combustion of biomass, vehicle and industrial emissions, and wildfire smoke. British Columbia (BC), Canada, with a land area of 944,735 km^2 and 27 regional districts, experienced its record-breaking wildfire season in 2017. However, due to the uneven distribution of PM2.5 ground monitoring stations in BC, PM2.5 concentrations in the rural area are difficult to retrieve. Remote sensing techniques and geographical information systems (GIS) could be used as supplementary tools to estimate PM2.5 concentrations. Aerosol Optical Depth (AOD) has been proven to have a strong correlation with PM2.5. Moderate Resolution Imaging Spectroradiometer (MODIS) provides AOD products in both 3 km and 10 km resolutions. The 3 km MODIS AOD products were released in 2013, and have been widely used to estimate PM2.5 concentrations in several studies.

This study adopted the 3 km Aqua MODIS AOD products to estimate PM2.5 concentrations in BC in the year of 2017 by combining ground station measurements, meteorological and supplementary data. MODIS AOD products were validated with ground-level AErosol RObotic NETwork (AERONET) AOD data. The Multiple Linear Regression (MLR) model, Geographically Weighted Regression (GWR) model, and a novel theoretical model were then conducted to estimate PM2.5 concentrations by integrating MODIS AOD products, ground-level PM2.5 concentrations, meteorological and supplementary data. After comparing the performance of the three models, the GWR model was used to generate annual, seasonal, and monthly spatial distribution maps of PM2.5. The application feasibility of MODIS AOD products in predicting PM2.5 was also examined.

The validation results showed that there was a strong correlation between the MODIS AOD and the AERONET AOD. The GWR model had the best prediction performance, while the MLR generated the worst prediction results. After analyzing the spatial distribution maps of PM2.5 with ground-level PM2.5 distribution maps, it could be concluded that the PM2.5 concentrations estimated by the GWR model almost follow the same trend as ground station measured PM2.5. In addition, PM2.5 concentrations were the highest in summer and August based on the estimation results of seasonal and monthly GWR models. It indicated that the application feasibility of MODIS AOD products in predicting PM2.5 concentrations during BC's wildfire season was high.

Acknowledgements

First and Foremost, I would like to express the deepest appreciation to my supervisor, Professor Dr. Jonathan Li, who provides valuable suggestions and continuous encouragement during my master program. It would be impossible for me to complete this thesis without his insightful suggestions and patient guidance. I feel grateful to have this opportunity to work with him in the past two years.

I would like to thank my thesis committee members, Dr. Michael Chapman, Professor at the Department of Civil Engineering, Ryerson University, Dr. Rebecca K. Saari, Assistant Professor at the Department of Civil and Environmental Engineering, University of Waterloo, and Dr. Yuhong He, Associate Professor at the Department of Geography, University of Toronto Mississauga, for reviewing my thesis, serving as my thesis examining committee, and providing me the constructive comments and suggestions.

Furthermore, I would like to express my thanks to all the members in Mobile Sensing and Geodata Analytics Lab, including Mengge Chen, Weiya Ye, Ying Li, Ming Liu, and Lingfei Ma. I also want to give my special thanks to Ming Liu for her selfless support and valuable suggestions for my thesis. In addition, I would like to acknowledge NASA for providing me MODIS AOD and NDVI products; AERONET team for AERONET AOD data; ECMWF for meteorological data, the Government of BC for ground-level and DEM data. Thanks also go to faculty members and staffs, including Alan Anthony and Susie Castela at the Department of Geography and Environmental Management for their help in the past two years.

Last but not least, I would like to express my deepest gratitude to my parents for their unconditional love, support, and encouragement during my master program. Although my parents are not in Canada, their meanings to me are hard to express in words. I will not be able to finish my thesis without them. I also want to appreciate my friends for accompanying and encouraging me during the hard times in the past two years.

Table of Contents

List of Figures

List of Tables

List of Abbreviations

AATSR	Advanced Along-Track Scanning Radiometers
ABI	Advanced Baseline Imager
ADV	AATSR dual-view
AERONET	AErosol RObotic NETwork
AHI	Advanced Himawari Imager
AIC	Akaike information criterion
ANN	Artificial Neural Network
AOD	Aerosol optical depth
API	Air Pollution Index
AQHI	Air Quality Health Index
AQI	Air Quality Index
AQMS	Air Quality Management System
ASV	AATSR single-view
ATSR-2	Along-Track Scanning Radiometers
AVHRR	Advanced Very High-Resolution Radiometer
BAM	Beta Attenuation Monitoring
BC	British Columbia
BEAR	Bremen Aerosol Retrieval
BoM	Bureau of Meteorology AOD Australian network
BRDF	Bidirectional reflectance distribution function
CAAQS	Canadian Ambient Air Quality Standards
CALIOP	Cloud-Aerosol Lidar with Orthogonal Polarization
CALIPSO	Cloud-Aerosol Lidar and Infrared Pathfinder Satellite Observations
CAMx	Comprehensive Air Quality Model with Extensions
CARSNET	China Aerosol Remote Sensing Network
CCME	Canadian Council of Ministers of the Environment
CMAQ	Community Multiscale Air Quality
CNEM	Chinese National Environmental Monitoring
CO	Carbon Monoxide
CO_2	Carbon Dioxide
COMS	Communication, Ocean, and Meteorological Satellite
CPCB	Central Pollution Control Board
CTM	Chemical Transport Model

CV	Cross validation
DB	Deep Blue
DEM	Digital elevation model
DRAGON	Distributed Regional Aerosol Gridded Observation Network
DT	Dark Target
ECMWF	European Centre for Medium-Range Weather Forecasts
EE	Expected Error
EEA	European Environment Agency
EPA	Environmental Protection Agency
ESA	European Space Agency
ESR	European Skynet Radiometers network
FMF	Fine mode fraction
GAM	Generalized Additive Model
GAW-PFR	Global Atmospheric Watch Precision Filter Radiometer network
GDP	Gross domestic product
GOCI	Geostationary Ocean Color Imager
GOES	Geostationary Operational Environmental Satellite
GWR	Geographically Weighted Regression
HDF-EOS	Hierarchical Data Format-Earth Observing Systems
IDW	Inverse distance weighting
LAADS	Level-1 and Atmosphere Archive and Distribution System
LUR	Land Use Regression
LUT	Look-Up Table
MAIAC	Multiangle Implementation of Atmospheric Correction
MAPE	Mean absolute percentage error
MEM	Mixed-Effect Model
MERIS	MEdium Resolution Imaging Spectrometer
MFRSR	Multifilter Rotating Shadowband Radiometer
MISR	Multi-angle Imaging SpectroRadiometer
MLR	Multiple Linear Regression
MODIS	Moderate Resolution Imaging Spectroradiometer
MSE	Mean absolute value
NAAQS	National Ambient Air Quality Standards
NDVI	Normalized Difference Vegetation Index
NLR	Nonlinear Regression

NO_2	Nitrogen Dioxide
NOAA	National Oceanic and Atmospheric Administration
O_3	Ground-level Ozone
OLI	Operational Land Imager
OMI	Ozone Monitoring Instrument
Pb	Lead
PBLH	Planetary Boundary Layer Height
PFR	Precision Filter Radiometers
PM	Particulate Matter
PM0.1	Particulate Matter (diameter smaller than 0.1 μm)
PM10	Particulate Matter (diameter smaller than 10 μm)
PM2.5	Particulate Matter (diameter smaller than 2.5 μm)
QAC	Quality Assurance
QC	Quality Control
RF	Random Forest
RH	Relative Humidity
RMSE	Root mean square error
SARA	Simplified Aerosol Retrieval Algorithm
SDS	Science Data Sets
SeaWIFS	Sea-Viewing Wide Field-of-View Sensor
SKYNET	SKYradiometer NETwork
S-NPP	Suomi National Polar-orbiting Partnership
SO_2	Sulfur Dioxide
SOAR	SeaWIFS Ocean Aerosol Retrieval
SP	Surface Pressure
SSA	Single scatter albedo
SURFRAD	Surface Radiation Budget Observing network
SVR	Support Vector Regression
TEM	Temperature
TEOM	Tapered Element Oscillating Microbalance
TOA	Top-of-the-atmosphere
TOMS	Total Ozone Monitoring Suite
TSM	Two-stage Model
USGS	U.S. Geological Survey
UW	U Wind Speed

VIF	Variation inflation factor
VIIRS	Visible Infrared Imaging Radiometer Suite
VIS	Visibility
VW	V Wind Speed
WHO	World Health Organization
WRF-Chem	Weather Research and Forecasting Model with Chemistry

Chapter 1 Introduction

1.1 Background

1.1.1 Air Pollution and Major Pollutants

Air pollution has been recognized as one of the most controversial topics in the world, especially in many developing countries, such as China and India (Kanada et al., 2013). It is estimated that around 4.2 million people died as a result of exposure to outdoor air pollution and 3.8 million people died as a result of exposure to indoor air pollution, which contributed to 7.6% and 7.7%, respectively of all deaths in 2016 (WHO, 2017). The common sources that could generate outdoor air pollution include emissions from motor vehicles, fuel combustion, and biomass burning (NSW Government, 2013). By contrast, indoor air pollution is often neglected by most people. In many developing countries, people are still using solid fuels, open fires, and insufficient stoves to cook (EPA, 2017). Air pollution is also major reason for biodiversity loss and respiratory diseases globally (Li et al., 2017).

According to the National Ambient Air Quality Standards (NAAQS) firstly set by the United States Environmental Protection Agency (US EPA), six pollutants include ground-level ozone (O_3), particulate matter (PM), carbon dioxide (CO_2), lead (Pb), sulfur dioxide (SO_2), and nitrogen dioxide (NO_2) are listed as common air pollutants (also known as "criteria air pollutants") (EPA, 2018). It is reported that exposure to those pollutants could lead to health, environmental, and monetary losses (Wang et al., 2014).

1.1.2 Introduction to PM2.5

PM stands for particulate matter, which refers to the combination of all toxic liquid and solid particles with complex compositions and different diameters in the atmosphere (Karagulian et al., 2005; Fuzzi et al., 2015; Raaschou-Nielsen et al., 2017). PM could be divided into three categories depending on the size of particles (i.e., diameters); including coarse particles, fine particles, and ultrafine particles (Grivas et al., 2018). Coarse particles are particles with diameters ranging from 2.5 to 10 μm (such as PM10). Fine particles are particles with diameters 2.5 μm or less (such as PM2.5). Ultrafine particles are fine particles with diameters smaller than 0.1 μm (such as PM0.1) (Zhang et al., 2015). Besides particle size, coarse, fine, and ultrafine particles also differ from the formation process, life expectancy, source, and spatial distribution (Kumar et al., 2008).

PM2.5 comes from both primary and secondary sources. Primary sources include incomplete combustion, vehicle and industrial emissions, dust, wildfire smoke, heating, and cooking. Among these

sources, vehicle emissions could be considered as the most significant primary PM2.5 source (Martin & Graca, 2018). Secondary sources involve some complex chemical reactions of gases (Department for Environment Food & Rural Affairs, 2016). Primary sources are related to both human-made and natural activities, while secondary sources are more related to primary sources (Jayarathne et al., 2018). The components of PM2.5 vary between anthropogenic and natural sources. Dominici et al. (2015) analyzed chemical compositions of PM2.5 in 95 US counties and concluded that sulfate, nitrate, ammonium, elemental carbon, organic carbon, silicon, and sodium ion were chosen to be seven chemical components of PM2.5, since each of the component contributed greater than 1% of PM2.5 mass on a seasonal or yearly basis.

The rising level of PM2.5 reveals adverse effects on climate change, public health, economic losses, and international conflicts. Figure 1.1 summarizes the effects of PM2.5 on different components of the atmosphere. PM2.5 concentrations depend on meteorological conditions, which means there is a significant correlation between climate change and PM2.5 (Tai et al., 2010). With increasing temperature, chemical reactions will also speed up. It takes a shorter time to emit PM2.5, and as a result, climate change will be worse (Hogrefe, 2012). Khanna et al. (2018) conducted an experiment to prove that the visibility is negatively correlated to chemical constituents of PM2.5. Furthermore, PM2.5 might cause acid rain and reduce agricultural productivity because of sulfate aerosols. Normally, high wind velocity and precipitation reduce PM2.5 concentrations. However, urban areas normally have low wind velocity, which makes the PM2.5 level higher than those in rural areas (Martins & Graca, 2018). It is estimated that urban area with high traffic density generated up to 140% higher PM2.5 concentrations than that in suburban or rural areas (Mukherjee & Agrawal, 2018).

The most serious problem of PM2.5 is public health. As a result of climate change and air pollution, the reduction of the healing capacity of natural systems leads to severe health effects (Mukherjee & Agrawal, 2018). Due to its small size, PM2.5 can easily penetrate into the lung deeply and hurt lung function consequently (Xing et al., 2016). It also increases the risk of premature death, especially for people with weak immune system, such as children and elder people (Lu et al., 2019). It is estimated that exposure to PM2.5 leads to death of 9500 people every year, which accounts for the highest mortality rate among three major air pollutants in Canada (the other two are NO_2 and O_3). It occupies 4.3% of baseline mortality (Health Canada, 2017). PM2.5 reveals both short-term and long-term effects on human health. In the short-term, infections of asthma, lung cancer, heart disease, and respiratory inflammation are possible (Lu et al., 2019). In the long-term, the risk of age-specific mortality will increase, as well as premature risk (Feng et

al., 2016). Moreover, Requia et al. (2017) stated that PM2.5 contributes to diabetes and high blood pressure incidence in Canada.

PM2.5 also brings economic losses. For those countries that give their first priority to economic development, the PM2.5-related economic losses are massive. In 2016, China lost USD 101.39 billion to PM2.5-related exposure, which accounts for 0.91% of the national GDP (Maji et al., 2018). India spent over USD 0.5 trillion to offset economic losses that resulted from PM2.5-related public health issues in 2010 (Etchie et al., 2017). The Government of Canada pays billions of dollars each year to cover increased requirement for medical care and the potential risk of premature death (Environment and Climate Change Canada, 2017).

In addition, PM2.5 will also lead to international issues. For example, it is estimated that half of Ontario's PM2.5 comes from the United States (Ontario Ministry of Environment, Conservation and Parks, 2010). Japan, Taiwan, and Hong Kong are significantly affected by high concentrations of PM2.5 during active storm seasons due to the dust that comes from the mainland China (Li, 2016). Those losses are hard to count on real numbers, which makes it difficult to negotiate between different countries/regions.

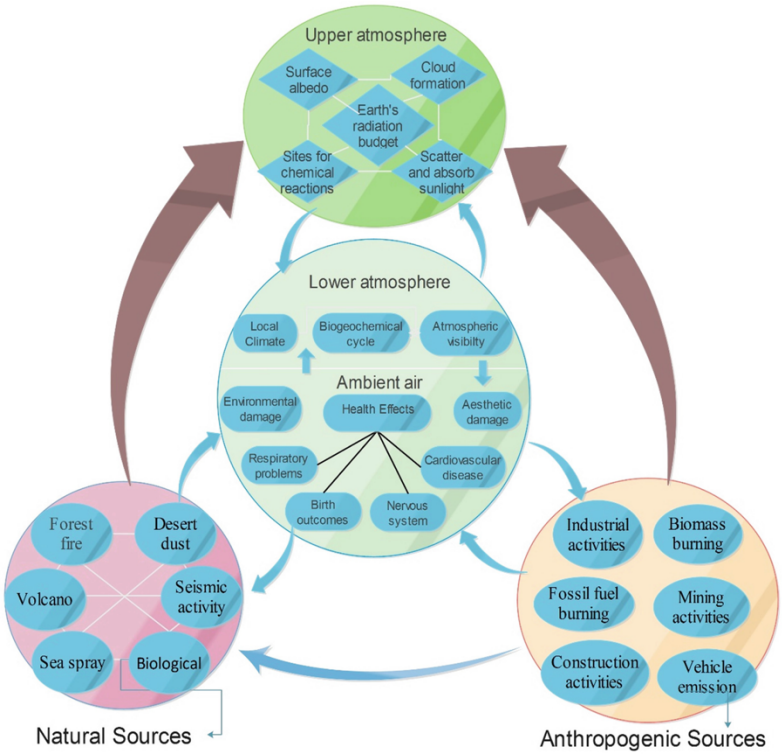

Figure 1.1 Effects of PM2.5 on different components of the atmosphere (Source: Mukherjee & Agrawal, 2018)

1.1.3 Global PM2.5 Standards and Regulations

Since substantial evidence has demonstrated that PM2.5 is extremely harmful to health and is responsible for haze pollution, it is essential to propose guidelines towards PM2.5. From a global perspective, different countries/regions have diverse standards and regulations based on national conditions and variations in PM2.5 levels (Wu et al., 2017). World Health Organization (WHO) has established guidelines for PM2.5 as reference standards (WHO, 2018). Government organizations are the primary sources to provide reliable and accurate PM2.5 recordings, such as Chinese National Environmental Monitoring (CNEM) in China, EPA in United States, European Environment Agency (EEA) in Europe, Central Pollution Control Board (CPCB) in India, and Air Quality Management System (AQMS) in Canada (Mukherjee & Agrawal, 2018). Table 1.1 summarizes the current guidelines of PM2.5 levels for main countries and organizations. These values are proposed based on the degree of toxicity, economic status, length of monitoring time, geographic information, and emission sources (Mukherjee & Agrawal, 2018). PM2.5 concentrations exceed the guideline values are suggested to be toxic and harmful for health.

Canadian Ambient Air Quality Standards (CAAQS) was firstly established by the Canadian Council of Ministers of the Environment (CCME) in 1999. The old 2015 standards were reviewed in 2012, and for PM2.5 were 28 $\mu g/m^3$ daily and 10 $\mu g/m^3$ yearly. The new 2020 standards were reviewed in 2015, and the latest standards for daily and annual PM2.5 are 27 $\mu g/m^3$ and 8.8 $\mu g/m^3$, respectively. Some regions even have stricter regulations towards PM2.5. For example, the daily and annual standards for PM2.5 in BC are 25 $\mu g/m^3$ and 6 $\mu g/m^3$, respectively (Ministry of Environment, 2018).

Table 1.1 PM2.5 Guidelines in selected countries/organizations (Source: AirNow, 2018)

Country/Organization	Daily (24-hour) ($\mu g/m^3$)	Annual ($\mu g/m^3$)	Issued Year	Guidelines
WHO	25	10	2005	Air Quality Guidelines Global
United States	35	12	2015	National Ambient Air Quality Standards (NAAQS)
China	35	15	2012	Ambient Air Quality Standards
India	60	40	2009	National Ambient Air Quality Standards
European Union	N/A	25	2013	European Commission Air Quality Standards
Australia	25	8	2002	National Environment Protection Measure for Ambient Air Quality (Air NEPM)
Canada	28 (2015)	10 (2015)	2012	Canadian Ambient Air Quality Standards (CAAQS)
	27 (2020)	8.8 (2020)	2015	

From a global perspective, Asia consists of countries with high population density and high level of polluted areas (Figure 1.2). It is reported that PM2.5 levels in India are five times higher than WHO standards. Mongolia and China contribute the highest averaged annual PM2.5 levels, which are 64 $\mu g/m^3$ and 41 $\mu g/m^3$, respectively. Japan is the only country in Asia that has lower PM2.5 concentrations than the WHO mean annual standard. Europe generates less PM2.5 than other continents because of the usage of green resources, idle reduction, and less populated. Similarly, North America also suffers less from PM2.5,

except Mexico. Mexico has 2.5 times higher PM2.5 levels than the WHO mean annual standard. South America performs better than that in Asia. Most countries except Peru have PM2.5 levels around 30 μg/m^3. However, it needs to be alerted that PM2.5 levels are increasing year by year. Africa is hard to analyze due to lack of data. Based on the available information, PM2.5 levels in Africa exceed the WHO mean annual standard because of biomass combustion and poor road conditions.

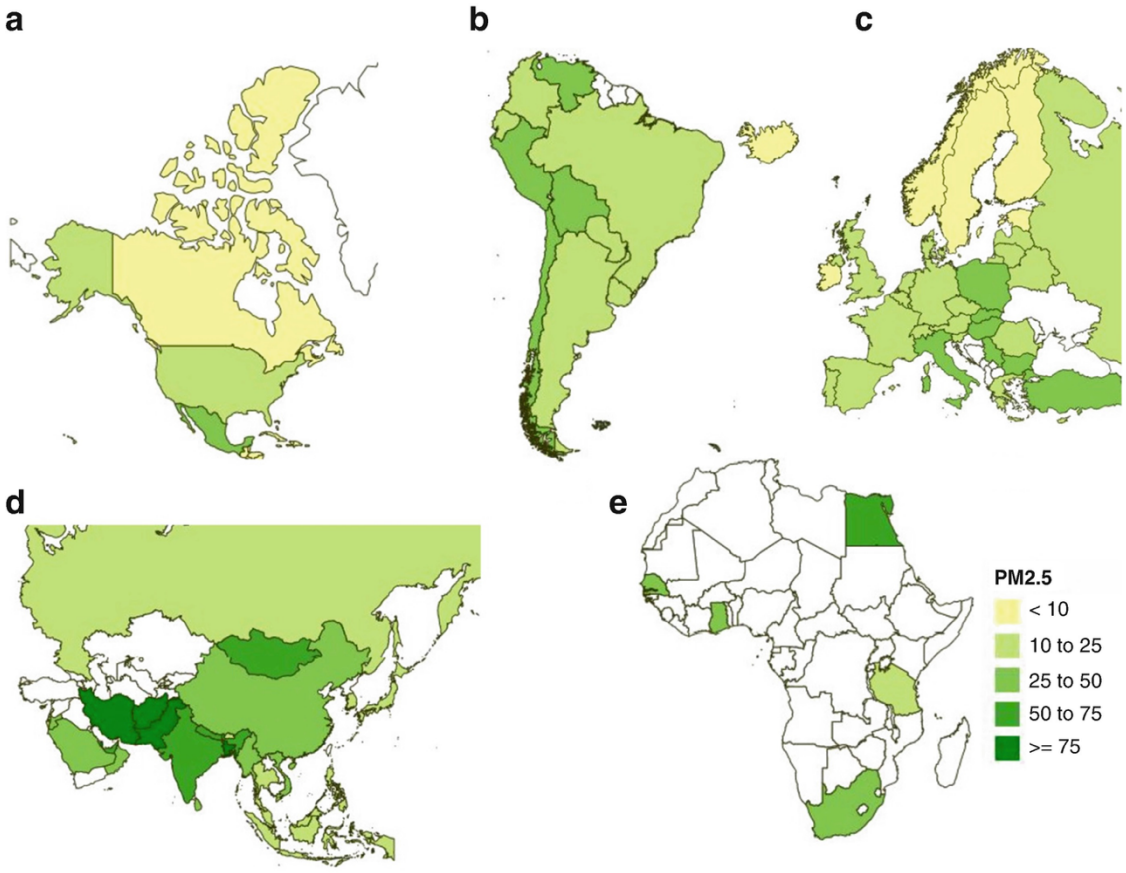

Figure 1.2 Distribution of PM2.5 levels (μg/m^3) in different continents: (a) North America, (b) South America, (c) Europe, (d) Asia, and (e) Africa (Source: Mukherjee & Agrawal, 2018).

1.1.4 Aerosol Optical Depth and PM2.5

Aerosols are the suspension of liquid or solid particles in air (Kulkarni et al., 2011). Smoke from wildfires, gas emissions from factories, and volcanic ash are all examples of aerosols (NASA earth observatory, n.d.). Aerosol optical depth (AOD) refers to the degree of aerosols that changes the path of light scattering, reflection, and absorption in the atmosphere (Mohamad, 2015; Gupta et al., 2018). The range of AOD varies between 0 and 1. AOD less than 0.1 indicates an excellent atmospheric condition with maximum visibility;

while a value of 1 indicates a hazy air condition with low visibility (NASA earth observatory, n.d.). AOD normally represents the difference between the total optical depth and the molecular scattering (Kazadzis et al., 2018). Figure 1.3 shows an example of the comparison between AOD distribution and fireplaces in August 2017, which could be concluded that fires play a vital role in aerosols.

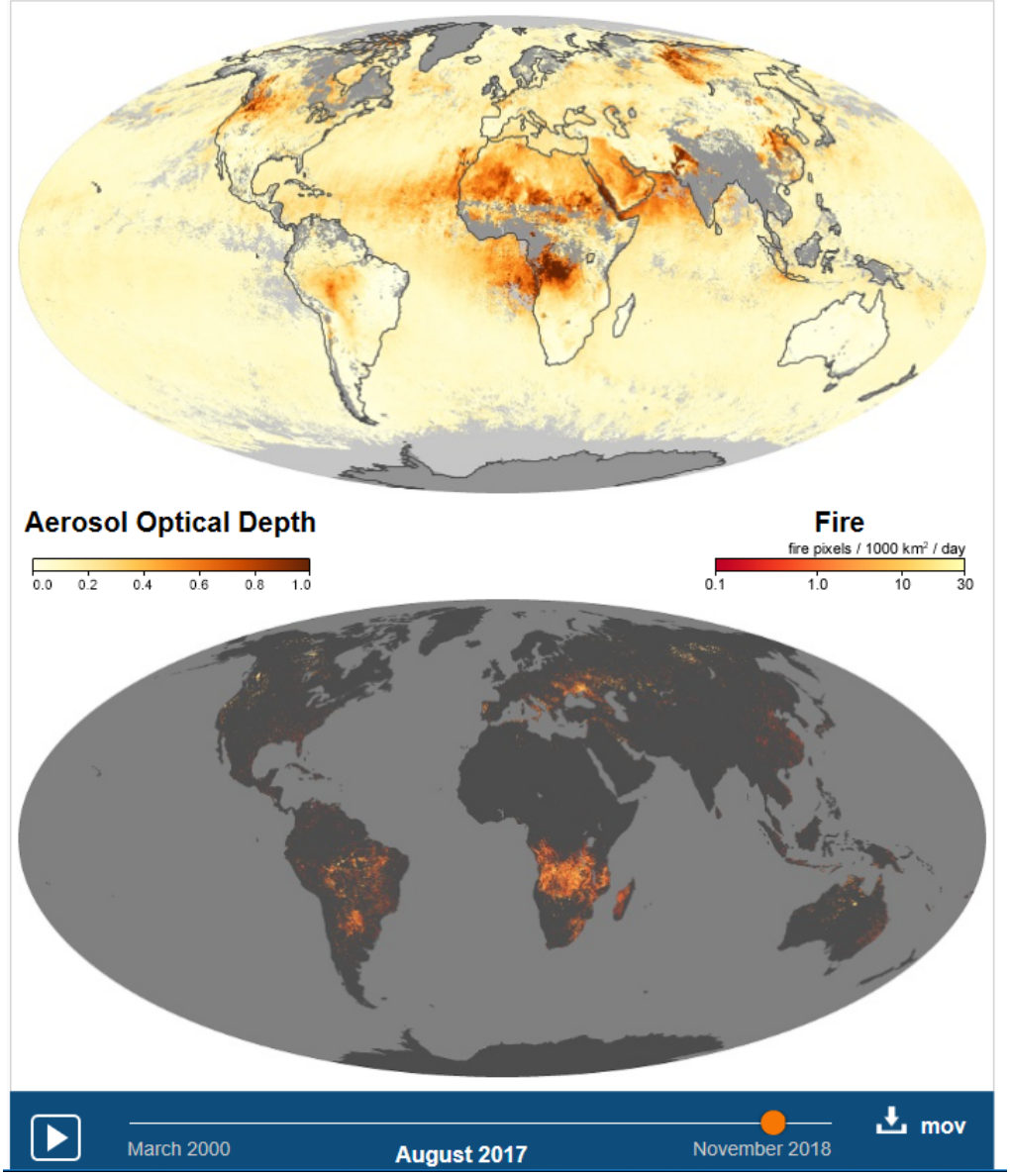

Figure 1.3 Comparison between AOD distribution and fireplaces in August 2017 (Source: NASA earth observatory, n.d.)

AOD is recognized as a good indicator of PM2.5 levels, and is used to predict PM2.5 concentrations (Shao et al., 2017). Numerous studies have proven that there is a strong positive correlation between AOD and ground-measured PM2.5 concentrations (Chu, 2006; Gupta et al., 2006; Kumar et al., 2007; Yang et al., 2018). Therefore, satellite-retrieved AOD is commonly used to estimate PM2.5 levels. Multiple satellite sensors are available for AOD retrieval, the most widely used is Moderate Resolution Imaging Spectroradiometer (MODIS). The Dark Target (DT) and the Deep Blue (DB) algorithms are adopted by MODIS to retrieve AOD. Numerous PM2.5 estimation models are available to predict PM2.5 concentrations using the satellite AOD, such as the Multiple Linear Regression (MLR), the Mixed-Effect Model (MEM), the Chemical Transport Model (CTM), the Geographically Weighted Regression (GWR), and novel theoretical models.

1.1.5 Comparison between Ground-based and Satellite-based PM2.5 Measurements

Most PM2.5 concentration information was collected from ground stations, since it is direct and accurate. However, it also reveals a few limitations. Firstly, the distribution of ground stations is uneven (Lee et al., 2016). Most stations are located within a certain distance, which limits the monitoring in a relatively small area (Lee et al., 2016). The United States has the most extensive monitoring program, but less than 30% of its counties have one or more ground stations (Hu et al., 2013). Therefore, the results of PM2.5-related exposure studies will be affected and bias will exist due to the lack of geographical and demographical information (Liu et al., 2005). Secondly, PM2.5 displays complicated temporal and spatial variation in different regions, which makes it difficult to provide continuous monitoring (Zhang & Cao, 2015). For example, PM2.5 was absent in China's national monitoring system before 2013 (Chu et al., 2016). In addition, the maintenance of ground stations is time-consuming and costly (Li, 2016).

Remote sensing techniques offer a cost-effective way to monitor PM2.5 by providing complete temporal and spatial information (Hu et al., 2014). It could be implemented as a supplementary tool for ground-level monitoring network (Ma et al., 2014). Also, it has higher feasibility. For example, in some developing countries with severe air pollution but lack of the sufficient number of ground stations, using satellite remote sensing techniques would be an optimal choice (Li, 2016). Moreover, satellite data is easier to access compared to ground station data. China's PM2.5 data was confidential before 2014 (Li, 2014). As mentioned in Section 1.1.4, most studies utilized satellite-retrieved AOD to estimate PM2.5 concentrations. However, it also brings some shortcomings. The results of estimation vary in different regions due to weather conditions, such as clouds, precipitation, wind, and snow, which might generate inaccurate PM2.5 concentrations (Chu et al., 2016). In addition, the correlation between PM2.5 and AOD is unstable, since

PM2.5 concentrations are measured near the surface, whereas AOD represents the aerosol distribution in the entire atmosphere (Xie et al., 2015). Therefore, it is prudent to combine ground station-based monitoring data and satellite remote sensing techniques in order to generate the most accurate outcomes.

1.1.6 Wildfires in British Columbia

Wildfires lead to forest disturbance, loss of biodiversity and damage of ecosystem service for humans (Pew & Larsen, 2001). Wildfire smoke is increasingly recognized as a significant source of air pollution and will result in public health issues (Black et al., 2017). In the past few decades, although air pollution in Canada has been well controlled due to proper regulation, fine particulate emissions from wildfires show upward trends since climate change aggravates the frequency and likelihood of wildfires (Black et al., 2017). It is estimated that approximately 40% of total particulate emissions were the result of wildfires, and over two million hectares of forest were burnt annually in Canada (Gralewicz et al., 2012; Black et al., 2017).

The composition of wildfire-generated PM2.5 is different from other sources of air pollution. According to Urbanski (2013), chemical components found in the particulate wildfire event are determined by the type of tree species burned, weather conditions, burning conditions, forest age, and landscape patterns. Wildfire smoke contributes the most to particulate air pollution. It is found that PM2.5 and ultrafine particles are the dominant wildfire-generated particles of wildfire smoke, while coarse particles are less produced (Gralewicz et al., 2012). Compared to coarse particles, PM2.5 and ultrafine particles have a slower velocity of stabilization and further distance of dispersal from the source (Wang et al., 2014). For instance, in 2015, PM2.5 concentrations exceeded NAAQS in Maryland due to a severe wildfire in Canada (Dreessen et al., 2016). As described before, the constituents of wildfire smoke depend on the type of vegetation (softwood or hardwood) and burning conditions (wet or dry) (Black et al., 2017). Exposure to wildfire smoke will lead to several health-related consequences. In wildfire smoke-affected areas, both hospital admissions and emergency rooms visit increase within a short time (Beverly & Bothwell, 2011). In addition, several studies have proven that the long-term impact of PM2.5 in wildfire smoke is related to respiratory health risks and cardiovascular diseases (Kunzli et al., 2006; Bell & Adams, 2008; Liu et al., 2017). Therefore, PM2.5 has been continuous monitored due to its unique characteristics.

The record-breaking wildfire season began on July 6, 2017 in British Columbia (BC), Canada. The main reasons are lightning and anthropogenic reasons. It is estimated that around 65,000 people were evacuated during the wildfire season, and the total cost was CAD 563 million (Ghnoussoub,

2017). It has been recorded as the worst wildfire season in BC's history. The Government of British Columbia did not relieve the provincial state of emergency until September 15, 2017. In total, approximately 120,000 hectares of forests were burnt, which accounts for 1.3% of the total BC area.

1.2 Objectives of the Thesis

Overall, the main purpose of this thesis is to predict PM2.5 concentrations using 3 km MODIS AOD products and PM2.5 estimation models in British Columbia (BC), Canada in 2017. The specific objectives of this thesis include:

1) to validate MODIS AOD measurements with ground-based AOD measurements,

2) to compare the performance of MLR, GWR, and a novel theoretical model in predicting PM2.5,

3) to analyze PM2.5 distributions on annual, seasonal, and monthly scales, and

4) to examine the application feasibility of MODIS AOD products during the wildfire season in BC.

1.3 Structure of the Thesis

The thesis is structured as following:

Chapter 1 provides a general introduction of the topic of this study, such as some background information, objectives, and structure of the thesis.

Chapter 2 reviews some relevant work related to PM2.5 monitoring, AOD retrieval methods, and models used to estimate PM2.5.

Chapter 3 introduces the study area, and the datasets used in this study.

Chapter 4 describes the methodology of this study, including MODIS AOD validation, data preprocessing, model construction, and output analysis.

Chapter 5 presents the main results and discussions of the study.

Chapter 6 concludes the thesis, analyzes some limitations of the study, and provides some recommendations for future studies.

Chapter 2 Background and Related Studies

Chapter 2 presents some literature review regarding relevant topics. Section 2.1 reviews ground-based PM2.5 measurements. Section 2.2 reviews AOD retrieval methods. Section 2.3 discusses the PM2.5-AOD estimation models. Section 2.4 reviews wildfire and PM2.5 studies in Canada. And at last, a summary of the chapter is provided in Section 2.5.

2.1 Ground-based PM2.5 Measurements

2.1.1 Air Quality Monitoring Programs

In order to monitoring and improve air quality, a large number of air quality monitoring programs have been established by countries and regions all over the world. Table 2.1 lists some of the main air quality monitoring programs in major countries/regions. China as one of the most polluted countries in the world, has implemented various programs to prevent and control its severe air quality (Hernandez, 2015). In the early 2000s, the Air Pollution Index (API) was utilized by the Chinese government to analyze the concentrations of different pollutants, including SO_2, NO_2, and PM10 in 42 cities (Li et al., 2012). In 2012, a new indicator named Air Quality Index (AQI) was introduced by China's Ministry of Ecology and Environment, which PM2.5 was recorded for the first time (Jiang et al., 2015).

Canada has both national, provincial, and regional monitoring programs. Table 2.2 presents all current active air quality monitoring programs in Canada. The National Air Pollution Surveillance (NAPS) program was established in 1969 and aims to provide accurate and long-term air quality data in populated areas of Canada (Dabek-Zlotorzynska et al., 2011). Particulate matters (PM2.5 and PM10) were monitored since 1984. Currently, there are 286 monitoring sites across Canada under this program. SO_2, NO_2, O_3, PM2.5, PM10, and carbon monoxide (CO) are continuously monitored (Environment and Natural Resources, 2013). These measurements are adopted by provinces and Environment Canada to report the AQI and the Air Quality Health Index (AQHI), respectively. Ontario (ON), BC, Alberta (AB), Québec (QC), and Newfoundland and Labrador (NL) have their own programs on the provincial scale (Air Quality Ontario; British Columbia Air Quality; Air Quality Health Index – Alberta Environment and Sustainable Resource Development; Province of Québec – Air Quality Index; Department of Environment and Conservation, Newfoundland and Labrador) (AirNow, 2018). In addition, Montreal and Metro Vancouver also have their own monitoring programs (Ville de Montreal-Air; Metro Vancouver Air Quality).

Table 2.1 Air quality programs in major countries/regions (Source: AirNow System, 2018)

Country/Region	Air Quality Program Name
China	Current Air Pollution Index (API)
	Shanghai Environment Monitoring Center (SEMC)
Taiwan	Current PSI
Indonesia	US Embassy Air Quality Index
Thailand	Regional Air Quality Data
Australia	Air Quality Index for Western Australia
New Zealand	New Zealand Ministry for the Environment – Air Quality
France	Airparif
Germany	Umweltbundesamt (UBA) – Current Concentrations of air pollutants in Germany
Spain	Castilla-La Mancha
Poland	Polish Provincial Air Quality Directory
United Kingdom	UK-AIR daily Quality Index
	The London Air Quality Network
	AirText – London forecast
United States	Environmental Protection Agency (EPA)'s AirNow System
Mexico	Gobierno del Estada de Jalisco – Calidad del Aire
Brazil	Qualidade do Ar – Sao Paulo
Columbia	Medelin – Colombia Air Quality Information System (SIATA)

Table 2.2 Active air quality programs in Canada (Source: AirNow System, 2018)

Air Quality Program Name	Scale
Canada Air Quality –AQI Maps	National
Canadian Air and Precipitation Monitoring Network (CAPMoN)	National
Environment Canada Air Quality Index	National
Air Quality Health Index – Alberta Environment and Sustainable Resource Development	Provincial
Air Quality Ontario	Provincial
British Columbia Air Quality	Provincial
Province of Québec – Air Quality Index	Provincial
Ministere du Developpement durable, de l'Environnement et des Parcs du Québec	Provincial
Department of Environment and Conservation, Newfoundland and Labrador	Provincial
Metro Vancouver Air Quality	Regional
Ville de Montreal – Air	Regional

2.1.2 Devices/Methods Used for Ground-level PM 2.5 Monitoring

Ground-level monitoring of PM2.5 is based on stations' recordings. Most stations adopt two common devices to measure concentrations of PM2.5. The first one is the Tapered Element Oscillating Microbalance (TEOM). It was designed by EPA to detect aerosol particles through their mass concentrations (Karagulian et al., 2012). The sample air goes through the filter membranes and PM2.5 accumulates during this process. Then, the frequency of oscillation changes as the mass is added. As a result, the instrument is able to calculate and output PM2.5 on a continuous basis (EPA, 2005). Figure 2.1 displays the operation of TEOM.

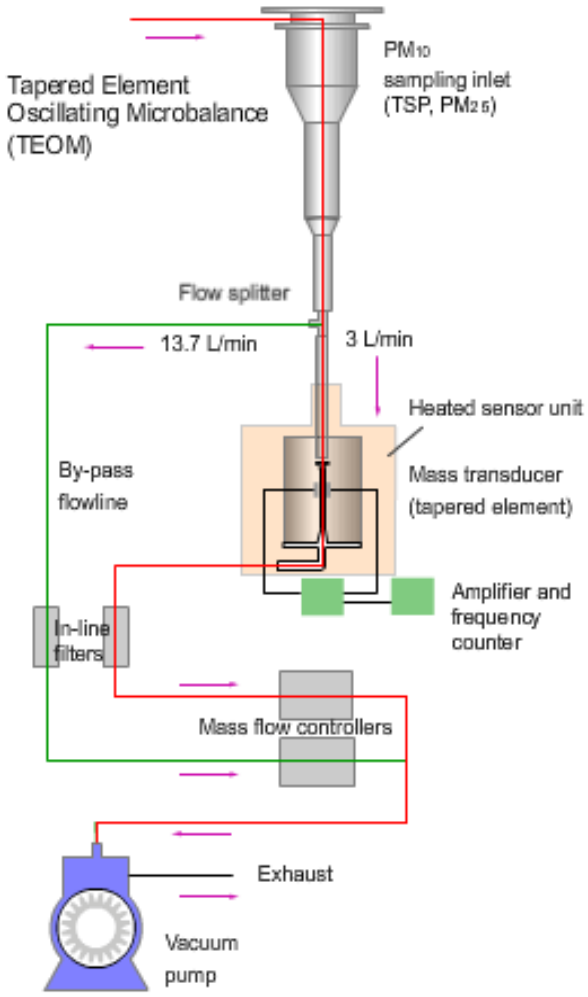

Figure 2.1 Operation of the TEOM (Source: Queensland Government, 2017)

TEOM was widely used for PM2.5 and PM10 monitoring after its first application in 1981, and is seen an ideal instrument for continuous monitoring of PM2.5 since it is easy to operate (Grover et al., 2005). Due to its high sensitivity to aerosol particles, TEOM is useful in urban areas (Jerez et al., 2006). In addition, it does not require the change of filters, which allows it to provide the peak value of PM2.5 during the day (Queensland Government, 2017). However, TEOM is not suitable for nanoparticles since it can only filter particles with a size between 1 and 10 μm (Sofowote et al., 2014). The operation of the TEOM is the same for all ground stations in the world. TEOM was used to monitor PM2.5 in Ontario, Canada between 2002 and 2012 and then replaced by SHARP 5030 to improve the accuracy of measurements in cold months (Su

et al., 2018). SHARP 5030 monitors PM2.5 combining light scattering photometry and beta (Su et al., 2018).

The second device is called Beta Attenuation Monitoring (BAM). The principle of BAM is to absorb beta radiation from the extraction of solid particles through air flow (Hauck et al., 2004). There are some reasons that might lead to overestimation of PM2.5 using BAM. Firstly, the glass fiber filters will absorb acid gas, so the final result will be inaccurate. Also, aerosol particles contain water content, which will create bias as well (Schweizer et al., 2016). Therefore, it needs attention to avoid such problems when using BAM. According to Watson et al. (2012), BAM is most suitable for short-term monitoring in haze areas. Most ground stations in BC use BAM 1020 as their measurement devices since it needs less maintenance than the TEOM (Environment and Climate Change Canada, 2016).

The gravimetric method is a quantitative method that determines the concentrations based on the mass before and after air goes through the filter (Ayers et al., 1999). The common problem while measuring the concentrations of PM2.5 and PM10 is the losses of semi-volatile matter (Zhu et al., 2011), Wang et al. (2016) compared the performance between the gravimetric method and the standard method when evaluating real-time fine particle matter concentrations in Beijing, and found that the gravimetric method displayed better results for particles with a larger size, such as PM10.

2.2 AOD Retrieval Methods

AOD retrieval methods could be divided into two categories, which are ground-level AOD measurements and satellite remote sensing-based measurements. By using ground instruments, the result of AOD retrievals will be more accurate and the temporal resolution is higher than that of satellite-based measurements (Lee et al., 2010). However, the uneven geographical distribution is a limitation of ground-based AOD measurements (Kumar et al., 2011). Satellite methods have wider spatial coverage, which could retrieve AOD in many places that are lack of monitoring networks (Lee et al., 2010).

2.2.1 Ground-level AOD Measurements

The principle of AOD retrieval on the ground is based on the spectral transmission of direct solar radiation (Kazadzis et al., 2018). AErosol RObotic NETwork (AERONET) is a global ground-based monitoring network that consists of hundreds of instruments to provide information about aerosol properties (NASA Goddard Space Flight Center, n.d.). It has been providing free-access, long-term, and continuous monitoring of AOD for over 25 years. Currently, there are 801 AERONET stations on every continent, which makes it the biggest aerosol monitoring network in the world (Figure 2.2). AERONET AOD products

include three levels, which are Level 1.0 (unscreened), Level 1.5 (cloud-cleared), and Level 2.0 (cloud-cleared and quality-assured) (Smirnov et al., 2011). AERONET AOD has been widely measured from the ground using CIMEL Electronique CE-318 sun-sky radiometer (Chen et al., 2019). This instrument measures direct sun radiation with a 1.2° full field-of-view every 15 minutes at 440, 675, 870, 940, and 1020 nominal wavelengths (nm) (Holben et al., 1998) (Figure 2.3). The purpose of CE-318 sun-sky radiometer is to observe both direct and scattered sunlight, and collect aerosol information (such as size distribution and optical thickness) (Sano et al., 2003). AOD retrieved from AERONET is extensively applied for satellite-derived AOD validation due to its low uncertainty (~0.01-0.02) (Kahn et al., 2010).

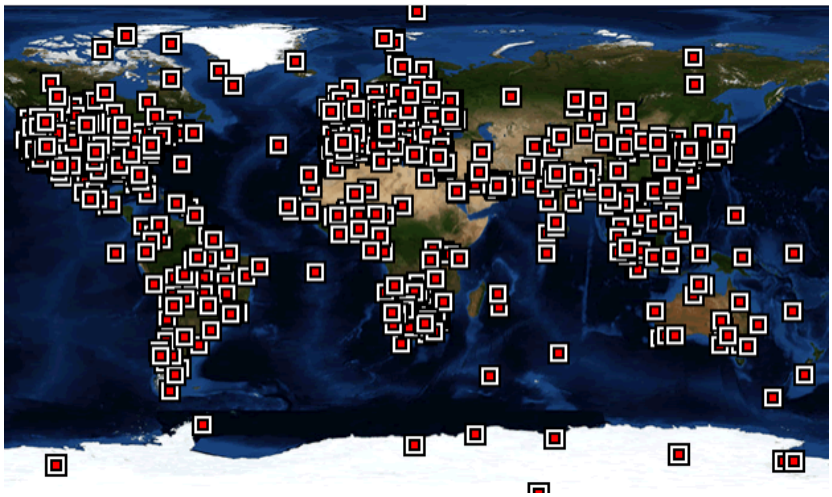

Figure 2.2 Distribution of AERONET sites (Source: NASA Goddard Space Flight Center, n.d.)

Figure 2.3 CIMEL Electronique CE-318 sun-sky radiometer used by AERONET (Source: NASA Goddard Space Flight Center, n.d.)

AEROCAN is the Canadian sub-network of AERONET, which was built 20 years ago and currently has 20 sites around Canada (Sioris et al., 2017). AEROCAN is valuable for long-term ground level AOD monitoring due to its design of photometers and regular maintenance (Sioris et al., 2017). In addition, AEROCAN is able to detect AOD especially in the case of wildfires or desert dust, which makes it a perfect supplementary sub-network for both AERONET and NAPS on the national scale (Freemantle et al., 2005).

SKYNET stands for the SKYradiometer NETwork, which is a global surface-based network of AOD measurements with the headquarter in Osaka, Japan (Campanelli et al., 2016). There are 60 sites in the SKYNET worldwide at present, and most of them are located in the Asia-Pacific region (Campanelli et al., 2016). The PREDE/POM sun-sky radiometer is the standard instrument for SKYNET with a 1° full field-of-view (Sano et al., 2003) (Figure 2.4). SKYNET has a higher frequency of AOD measurements than AERONET, and the time resolution is 1 minute (Pre-TECT, 2016). The biggest difference between the two main equipment in AERONET and SKYNET is that CIMEL uses two sensors to conduct direct and diffuse measurements, while PREDE uses the same sensor (Che et al., 2008). In 2010, the European Skynet Radiometers network (ESR) was established as a sub-network of SKYNET. ESR consists of 18 sites that are located in Europe, the United States, and Antarctica. Figure 2.5 displays the distribution of SKYNET and its sub-network ESR sites in the world. The yellow dots represent the sites of SKYNET, and the red dots represent the sites of ESR.

Figure 2.4 PREDE-POM sky-radiometer adopted by SKYNET (Source: Pre-TECT, 2016)

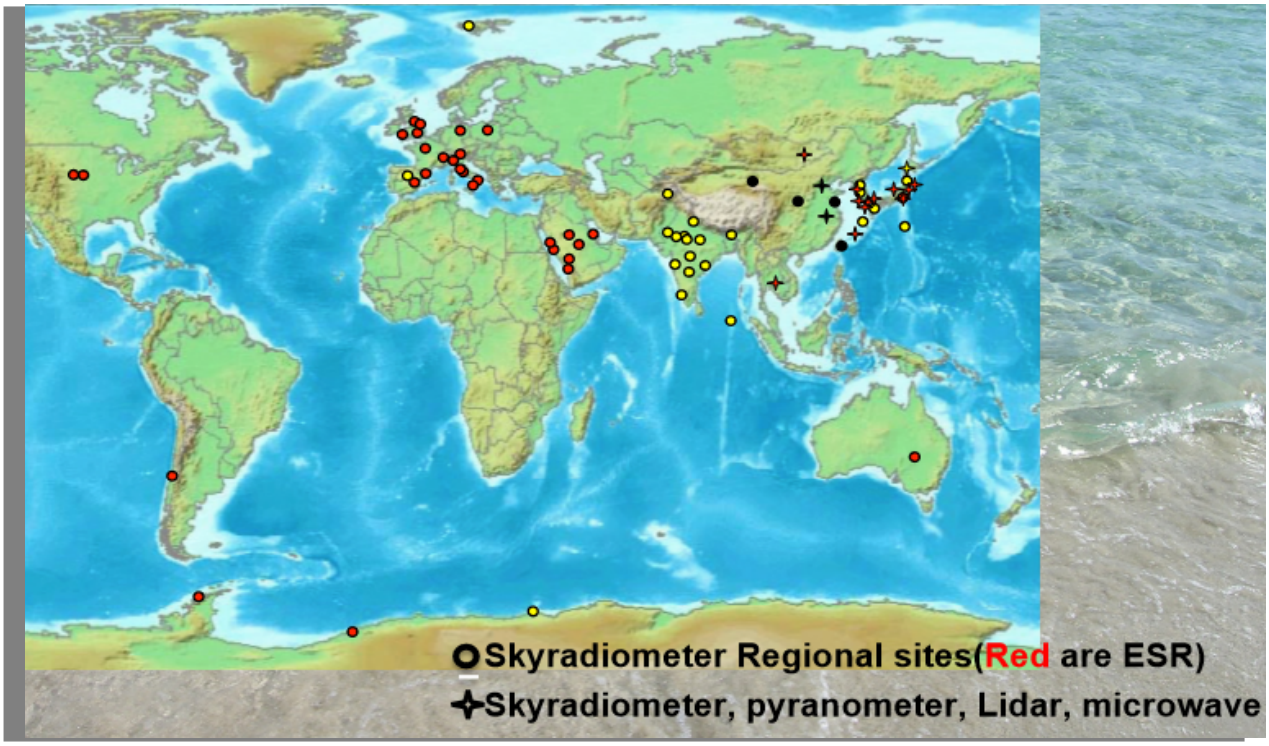

Figure 2.5 Distribution of SKYNET sites worldwide (Source: Pre-TECT, 2016)

Other than AERONET and SKYNET, there are a few other AOD monitoring networks on either small or large scales. Global Atmospheric Watch Precision Filter Radiometer network (GAW-PFR) has 12 sites and uses Precision Filter Radiometers (PFR) for AOD measurements (Nyeki et al., 2015). PFR has a 2.5° full field-of-view with 4 independent channels (Campanelli et al., 2016). Bureau of Meteorology AOD Australian network (BoM) is operated to solve the problem due to the lack of aerosol understanding in the Australian continent (Mitchell & Forgan, 2003). Surface Radiation Budget Observing network (SURFRAD) was established in 1995 for the United States as a supplementary tool for atmospheric research (Augustine et al., 2000). The Multifilter Rotating Shadowband Radiometer (MFRSR) is used to record aerosol characterization by SURFRAD (Lee et al., 2010). It measures total solar irradiances at six wavelengths (415, 500, 615, 673, 870, and 940 nm) (Lee et al., 2010). Distributed Regional Aerosol Gridded Observation Network (DRAGON) and China Aerosol Remote Sensing Network (CARSNET) are regional networks, which focus on Korea and China, respectively (Holben et al., 2011). In addition, light detection and ranging (LiDAR) technology has been used for AOD measurements in recent years (Chan, 2009).

2.2.2 Satellite-based AOD Measurements

Remote sensing techniques have been increasingly utilized to obtain AOD since the 1970s due to its wide spatial coverage (Yang et al., 2018). The satellite sensors used to retrieve AOD rely on the light reflectance and scattering of light, while ground-based sun-sky photometers could point at the sun directly and derive AOD through the attenuation of solar incidents (Remer et al., 2005). Several issues need to be considered regarding satellite-based AOD measurements, such as the sensor calibration accuracy; inadequate temporal or spatial coverage due to insufficient sampling; differences between algorithms; adequate data recording time intervals; and drawbacks of record time drift (Hsu et al., 2012). Some commonly used satellite sensors/instruments are briefly introduced in the following section (Table 2.3).

The Advanced Very High Resolution Radiometer (AVHRR) was the earliest sensor used to generate aerosol products aboard the Tiros-N satellite/National Oceanic and Atmospheric Administration (NOAA) since 1978 (Gao et al., 2016). AVHRR was firstly used to provide AOD information over oceans, and the algorithms were developed to retrieve AOD information over land (Hsu et al., 2017). AVHRR provides a longer length of data recording time than later sensors. Due to the lack of shortwave infrared bands (e.g. 2.1 μm), it is challenging for AVHRR to retrieve AOD over land (Mei et al., 2014). In addition, the surface reflectance is less sensitive to aerosol changes over land, which makes the retrieval of AOD becomes more difficult (Hauser et al., 2004). Mei et al. (2014) retrieved AOD over land surfaces in Northeastern China by combing Dark Target (DT) and simplified Look-Up Table (LUT) method adopted from the Bremen Aerosol Retrieval (BAER) algorithm. The result showed that 71.8% of the points located within the identity line compare to ground-based recordings. This method could be applied to sensors without 2.1 μm band (Mei et al., 2014). Similarly, the Total Ozone Monitoring Suite (TOMS) and Ozone Monitoring Instrument (OMI) have been monitoring aerosol properties over three decades (Fan et al., 2017).

The dual view Along-Track Scanning Radiometers (ATSR-2) and the Advanced Along-Track Scanning Radiometers (AATSR) was on service to obtain AOD over oceans and land from 1995 to 2012 (de Leeuw et al., 2018). AATSR has two viewing angles (forward 55° and nadir), which allows it to accumulate the effects on top-of-the-atmosphere (TOA) radiation (de Leeuw et al., 2016). However, according to de Leeuw et al. (2016), during the operation of ATSR-2 and AATSR, the cloud shadow is a major problem, which needs some cloud post-processing procedure to eliminate the effects of clouds.

The MEdium Resolution Imaging Spectrometer (MERIS) was the main instrument of the European Space Agency (ESA)'s Envisat-1 satellite, which was launched in 2002 and ended its mission in 2012. MERIS and AATSR belong to the same satellite. MERIS has a 68.5° field-of-view and 15 bands available

for selection based on ground demand (LADDS DAAC, 2018a). Kaskaoutis et al. (2010) used MERIS AOD products to compare with ground-based AOD measurements over the urban area (cloud-free).

The Multi-angle Imaging SpectroRadiometer (MISR) is an instrument on NASA's Terra satellite, and has been used to acquire AOD data since early 2000 (Garay et al., 2017). MISR has nine distinct zenith angles. The spatial resolution of MISR AOD product is 17.6 km, which represents a 16 × 16 pixel window with 1.1 km resolution in four narrow spectral bands (446, 558, 672, and 866 nm) including visible and near-infrared wavelengths (Garay et al., 2017). Due to MISR's independence on radiometric surface properties, it has been applied in landforms with high reflectance (such as deserts) (Martonchik et al., 2004). It is estimated that the uncertainty of the MISR AOD product is 0.08 compared to ground-based AERONET measurements over desert sites (Martonchik et al., 2004).

The Sea-Viewing Wide Field-of-View Sensor (SeaWiFS) was a satellite sensor on NASA's OrbView-2 satellite with eight spectral bands ranging from 412 to 865 nm operated from 1997 to 2010 (EARTHDATA, n.d.). Due to SeaWiFS's low uncertainty regarding sensor calibration, it is also suitable for AOD measurements in the visible and near-infrared wavelengths (Hsu et al., 2012). Hsu et al. (2012) adopted a new AOD retrieval method to examine patterns and trends of AOD on both regional and global basis over land and the ocean during SeaWiFS's mission time. The results exhibited a slightly positive trend for averaged AOD over the global ocean (Hsu et al., 2012).

The Visible Infrared Imaging Radiometer Suite (VIIRS) is one of five main instruments of Suomi National Polar-orbiting Partnership (S-NPP), and was launched in 2011. It was designed to meet the requirement of high spatial resolution with respect to AOD retrieval (Xiao et al., 2016). VIIRS is a new generation satellite sensor with 22 spectral bands ranging from 0.412 to 12.05 μm (Liu et al., 2014). VIIRS AOD products are divided into three categories based on quality flags, including high, degraded, and low (Xiao et al., 2016). Liu et al. (2014) concluded that VIIRS products overestimated AOD results over the vegetated area and underestimated results over the soil-dominated terrain.

Some novel sensors are adapted for AOD retrieval in recent years. The Cloud-Aerosol Lidar with Orthogonal Polarization (CALIOP) aboard the Cloud-Aerosol Lidar and Infrared Pathfinder Satellite Observations (CALIPSO), was utilized for AOD retrieval in 2012 for the first time (Bartlett et al., 2013). CALIPSO combines both active LiDAR equipment and passive infrared and visible imagers (NASA, 2018). The Operational Land Imager (OLI) aboard the Landsat 8 has been used to retrieve AOD over urban areas supported by MODIS bidirectional reflectance distribution function (BRDF)/Albedo data recently (Tian et al., 2018).

Table 2.3 Summary of commonly used sensors for AOD retrievals

Sensor	Satellite	Spectral Range (μm)	Number of Spectral Bands	Spatial Resolution (km)	Temporal Resolution (day)	Launch Year	Status	Orbit Type	Organization
AVHRR	TIROS-N	0.58 - 12.50	4	1.1	0.5	1978	Operational	Sun synchronous	US: NOAA
TOMS	NIMBUS-7	0.31 - 0.38	4	50	1 - 2	1978	Non-operational	Sun synchronous	US: NASA
SeaWIFS	Orbview-2	0.40 - 0.89	8	1.1/4.5	1	1997	Non-operational	Sun synchronous	US: NASA
MISR	Terra	0.45 - 0.87	4	0.275	2 - 9	1999	Operational	Sun synchronous	US: NASA
MODIS	Aqua/Terra	0.41 - 14.39	36	0.25/0.50/1.00	1 - 2	1999	Operational	Sun synchronous	US: NASA
AATSR	ENVISAT	0.56 - 12.0	7	1	35	2002	Non-operational	Sun synchronous	Europe: ESA
MERIS	ENVISAT-1	0.39 - 1.04	15	0.3	3	2002	Non-operational	Sun synchronous	Europe: ESA
OMI	AURA	0.27 - 0.50	3	13 × 25	1	2004	Operational	Sun synchronous	US: NASA
CALIOP	CALIPSO	N/A	N/A	5	5.92 seconds	2006	Operational	Sun synchronous	US: NASA
GOCI	COMS	0.41 - 0.87	8	0.5	1 hour	2010	Operational	Geostationary	Korea: KARI
VIIRS	Suomi NPP	0.41 - 12.0	22	0.75	1	2011	Operational	Sun synchronous	US: NASA
OLI	Landsat 8	0.43 - 1.38	9	0.015/0.03	16	2013	Operational	Sun synchronous	US: NASA
AHI	Himawari-8	0.47 - 13.3	16	0.5/1/2	10 min	2014	Operational	Geostationary	Japan: JMA
ABI	GOES-R	0.45 - 13.6	16	0.5/1/2	5 - 15 min	2016	Operational	Geostationary	US: NOAA

The Moderate Resolution Imaging Spectroradiometer (MODIS) is the most widely used satellite sensor to retrieve AOD. MODIS was launched aboard NASA's Terra and Aqua satellites in 1999 and 2002, respectively (Remer et al., 2005). The Terra (descending node from north to south) and Aqua (ascending node from south to north) cross the equator at 10:30 a.m. and 1:30 p.m. local time, respectively (National Snow & Ice Data Center, n.d.). MODIS has 36 spectral bands between 0.41 and 14.39 μm. Aerosol observations make use of seven bands ranging from 0.47 to 2.13 μm (between near-UV and mid-VIS channel) (Wang et al., 2017). Table 2.4 displays the band combination for MODIS. MODIS has three spatial resolutions, 250 m (band 1-2), 500 m (band 3-7), and 1000 m (band 8 -36) (Remer et al., 2005). MODIS has a swath of 2330 km, which allows it to provide global coverage in every one to two days (National Snow & Ice Data Center, n.d.). MODIS has relatively high spatial resolution and sufficient spectral diversity to derive aerosol properties (Remer et al., 2005). Chu et al. (2002) found that the expected error of MODIS AOD measurement is $\pm 0.05 \pm 0.2\tau_a$ (AERONET-based AOD) over land at 550 nm wavelength.

The current MODIS AOD product over land is called Collection 6.1 (061), which is an upgrade version of Collection 6 (C6) for all three levels of Atmosphere Team products (MODIS Atmosphere, 2017). MODIS derives AOD based on the DT and DB algorithms at 10 km spatial resolution (Nichol & Bilal, 2016). Tian et al. (2018) compared MODIS C6.1 and C6 aerosol products over Beijing, China and found that MODIS C6.1 DT products performed better than the C6 DT products; while MODIS C6.1 DB products had the same performance as C6 DB products. In addition, the DB algorithm generated better results in urban area then the DT algorithm according to the research of Tian et al. (2018) as well. For Collection 5 (C5) and other earlier collections, only 10 km aerosol products were available. The 10 km aerosol products were designed for climate change initially. In 2013, in order to meet the requirement of air pollution monitoring and high resolution in the fine-scale study area, a new aerosol product was released using the DT algorithm at 3 km spatial resolution (LAADS DAAC, 2018b). Xie et al. (2015) estimated PM 2.5 concentrations in Beijing using 3 km MODIS AOD products, and the results showed a good performance in predicting models.

Table 2.4 Band combinations for MODIS (Source: NASA MODIS, n.d.)

Primary Use	Band	Bandwidth (Band 1-19: nm Band 20-36: μm)	Spectral Radiance (W/m^2 -μm-sr)	Spatial Resolution (m)
Land/Cloud/Aerosols Boundaries	1	620 - 670	21.8	250
	2	841 - 876	24.7	
Land/Cloud/Aerosols Properties	3	459 - 479	35.3	500
	4	545 - 565	29.0	
	5	1230 - 1250	5.4	
	6	1628 - 1652	7.3	
	7	2105 - 2155	1.0	
Ocean Color/ Phytoplankton/ Biogeochemistry	8	405 - 420	44.9	1000
	9	438 - 448	41.9	
	10	483 - 493	32.1	
	11	526 - 536	27.9	
	12	546 - 556	21.0	
	13	662 - 672	9.5	
	14	673 - 683	8.7	
	15	743 - 753	10.2	
	16	862 - 877	6.2	
Atmospheric Water Vapor	17	890 - 920	10.0	
	18	931 - 941	3.6	
	19	915 - 965	15.0	
Surface/Cloud Temperature	20	3.660 - 3.840	0.45(300K)	
	21	3.929 - 3.989	2.38(335K)	
	22	3.929 - 3.989	0.67(300K)	
	23	4.020 - 4.080	0.79(300K)	
Atmospheric Temperature	24	4.433 - 4.498	0.17(250K)	
	25	4.482 - 4.549	0.59(275K)	
Cirrus Clouds Water Vapor	26	1.360 - 1.390	6.00	
	27	6.535 - 6.895	1.16(240K)	
	28	7.175 - 7.475	2.18(250K)	
Cloud Properties	29	8.400 - 8.700	9.58(300K)	
Ozone	30	9.580 - 9.880	3.69(250K)	
Surface/Cloud Temperature	31	10.780 - 11.280	9.55(300K)	
	32	11.770 - 12.270	8.94(300K)	
Cloud Top Altitude	33	13.185 - 13.485	4.52(260K)	
	34	13.485 - 13.785	3.76(250K)	
	35	13.785 - 14.085	3.11(240K)	
	36	14.085 - 14.385	2.08(220K)	

In addition to polar-orbiting satellites, imaging instruments on geostationary satellites are also adopted for AOD retrievals (Figure 2.6). The Geostationary Ocean Color Imager (GOCI) is the first geostationary image sensor aboard the Communication, Ocean, and Meteorological Satellite (COMS) of South Korea, and was on service since 2010 (Xiao et al., 2016). GOCI has eight spectral bands and concentrates in East Asia. It collects AOD information eight times per day and the values of AOD range from -0.1 to 5.0 (Xiao et al., 2016). Previous studies have proven that GOCI AOD products had well-calibrated linear regression with AERONET AOD products in East Asia (Park et al., 2014; Choi et al., 2016). The Advanced Himawari Imager (AHI) abroad the Himawari-8 geostationary weather satellite (launched in 2014), which has 16 spectral channels, with spatial resolutions ranging between 0.5 and 2 km, and temporal resolution between 10 and 25 minutes (Yang et al., 2018). AHI focuses on the Asia-Pacific region and aims to on service for 15 years (Yang et al., 2018). In western countries, the Advanced Baseline Imager (ABI) on board the Geostationary Operational Environmental Satellite (GOES) has the same spectral and spatial design as AHI, and is planned to be used for AOD retrieval as well in the future (GOES-R series, n.d.).

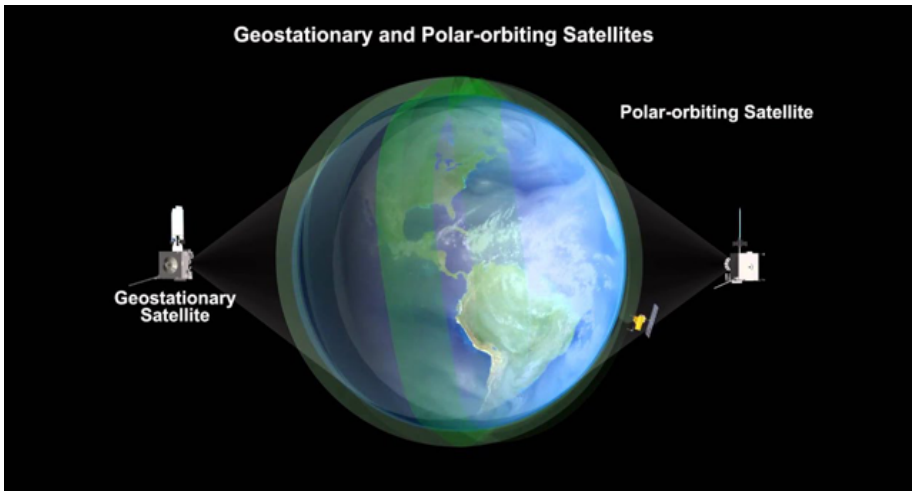

Figure 2.6 Differences between polar-orbiting and geostationary satellite (Source: Hong Kong Observatory, 2016)

2.2.3 AOD Retrieval Algorithms from Satellite Datasets

2.2.3.1 Overview

Several algorithms have been implemented for AOD retrieval from satellite sensor datasets, such as the AATSR dual-view (ADV) algorithm, the AATSR single-view (ASV) algorithm, the SeaWIFS Ocean Aersol Retrieval (SOAR) algorithm, the Simplifed Aerosol Retrieval Algorithm (SARA), the Multiangle Implementation of Atmospheric Correction (MAIAC) algorithm, the DT algorithm, and the DB algorithm.

The AATSR dual-view (ADV) algorithm and the AATSR single-view (ASV) algorithm are used by AATSR to retrieve aerosol properties over land and the ocean, respectively. The principle of ADV is to split the atmosphere and the surface using measured TOA (Kolmonen et al., 2016). ASV uses an ocean reflectance model to reduce the disparity between the observed and modelled TOA reflectance (Kolmonen et al., 2016). ADV and ASV are commonly used to retrieve AOD from AASTR data. Sundstrom et al. (2012) retrieved AOD in China using ADV and the results were satisfying.

The SeaWIFS Ocean Aerosol Retrieval (SOAR) algorithm was initially developed to retrieve AOD over ocean for SeaWIFS by Sayer et al. (2012). SOAR could be divided into three steps, including cloud pixels identification; AOD retrieval; and coarse resolution aggregation (Sayer et al., 2012). SOAR has been validated to use as a supplementary tool for VIIRS and MODIS AOD retrieval over land in recent years Sayer et al., 2018).

The Simplified Aerosol Retrieval Algorithm (SARA) was developed by Bilal et al. (2013) for MODIS. SARA assumes the surface is Lambertian, and at the same time, SSA and Asymmetric Function do not vary on the day of retrieval (Bilal et al., 2013). The biggest advantage of SARA is that it does not require the use of a look up table (LUT). However, SARA requires ground-based AOD information from AERONET or any supplementary source related to the study area, which might limit the spatial extent of the research area (Bilal et al., 2013). Zhang et al. (2019) implemented an updated version of SARA to retrieve AOD in Beijing from AHI datasets, and results showed that the latest SARAHI algorithm is suitable for regional AOD retrieval.

The Multiangle Implementation of Atmospheric Correction (MAIAC) is a novel algorithm that combines time series and image processing to generate accurate aerosol properties (Lyapustin & Wang, 2012). The principle of MAIAC is to use the sliding window technique to conduct the time series analysis, which is different from conventional AOD retrieval algorithms (Lyapustin & Wang, 2012). Currently, DT and DB are the most used algorithms for MODIS. MAIAC will be implemented in the future step by step.

2.2.3.2 Dark Target Algorithm

The DT and the DB algorithms are the two widely used algorithms for MODIS to retrieve AOD. There are two types of DT, which are implemented to retrieve AOD over land and over ocean, respectively (Wang et al., 2019). The spatial resolution of the standard DT product for MODIS is 10 km (Bilal et al., 2018). Since the low resolution cannot meet the requirements of city-scale study, a new 3 km DT product was released in the C6 as a supplementary product (Fan et al., 2017).

The general principle of the 10 km DT product is to utilize a stable linear regression between two visible bands (0.47 and 0.66 μm) and the shortwave infrared band (2.13 μm) to collect surface reflectance over dark surfaces (Fan et al., 2017). Figure 2.7 shows the flowchart of DT algorithms. Pixels are selected using TOA reflectance between 0.47 and 0.66 μm in the 2.13 μm band. Then, selected pixels are organized into nominal 10 km × 10 km retrieval boxes with 20 × 20 pixels per box at 500 m resolution (10 km at nadir). Bright pixels (such as cloud, snow and ice) are masked, and water and land pixels are separated during this process. For the rest of pixels in the retrieval box, the darkest 20% and the brightest 50% pixels will be discarded to eliminate possibly contaminated pixels and to reduce uncertainty. The remaining 30% of pixels will be used for AOD retrieval path. The minimum dark target pixels required in each box is 12 over land or 11 over ocean (and more for high quality). If the number of dark target pixels is insufficient, there will be no aerosol retrievals in the box (Remer et al., 2005; Safarpour et al., 2014; Bilal et al., 2018).

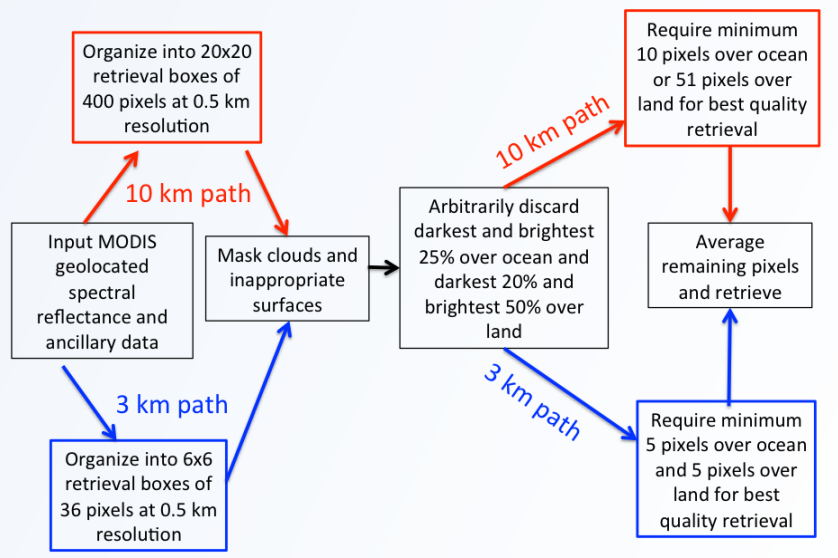

Figure 2.7 Flowchart of 10 km (red) and 3 km (blue) DT algorithms of AOD retrievals (Source: Dark Target Aerosol Retrieval Algorithm, n.d.)

The 3 km DT product has the same retrieval method as the 10 km product, except for the selection of dark target pixels and the number of pixels arranged in each retrieval box. Pixels are selected using the TOA reflectance between 0.47 and 0.66 μm in the 2.13 μm band. Selected pixels are organized into nominal 3 km × 3 km retrieval boxes with 6 × 6 pixels per box at 500 m resolution. In addition, the minimum dark target pixels required in each box is 6 over land or 5 over ocean (Lyapustin et al., 2010). Therefore, the 3 km DT product generates noisier product than the 10 km DT product because fewer pixels contribute during the retrieval process (Bilal et al., 2018). Previous studies have proven that the 3 km DT product underestimated the surface reflectance and misused the aerosol models, which result in more inaccurate results than the 10 km DT product (Munchak et al., 2013; Livingston et al., 2014).

2.2.3.3 Deep Blue Algorithm

Although DT has become the most widely used algorithm for satellite-based MODIS AOD retrievals due to its high accuracy on the surfaces with low reflectance (such as water and vegetated area), it still has drawbacks over bright surfaces (Fan et al., 2017). Therefore, a new algorithm called Deep Blue (DB) was introduced by Hsu et al. (2004) for MODIS to retrieve AOD over bright surfaces. The first generation of DB only allows it to derive AOD over bright surfaces. In 2013, an enhanced version of DB was released by Hsu et al. (2013), which could be used to retrieve AOD over both bright and dark surfaces. DB is only used for land retrieval, and only 10 km product is available (NASA, n.d.). DT uses 500 m pixels, while DB uses 1 km pixels during the retrieval process. DB utilizes surface reflectance in the blue bands to record surface signal and spectral reflectance ratios (NASA, n.d.).

The DB algorithm could be divided into four main steps (Figure 2.8). Firstly, the Rayleigh correction is applied to account for surface pressure variation, and cloud screening is performed by evaluating spatial autocorrelation and absorbing aerosol index values within a 3 × 3 pixel box (Safarpour et al., 2014). Secondly, cloud-free and snow-free pixels are selected using TOA reflectance at 0.41, 0.49, and 0.65 μm based on the geolocation at nominal 1 km × 1 km retrieval boxes (Sayer et al., 2013). Thirdly, comparing values between surface reflectance at 0.41, 0.49, and 0.65 μm and those stored in the LUT. Pixels with the best match will be retrieved using the maximum likelihood method. Lastly, AOD and single scatter albedo (SSA) are retrieved. Each 1 km × 1 km retrieval box is then averaged to 10 km × 10 km scale (Sayer et al., 2013; Safarpour et al., 2014). The DB algorithm has been validated with previous studies, and it is commonly recognized that the 10 km DB product achieves higher accuracy than the 10 km DT product especially over surfaces with high reflectance (Sayer et al., 2014; Tao et al., 2015; Bilal et al., 2017).

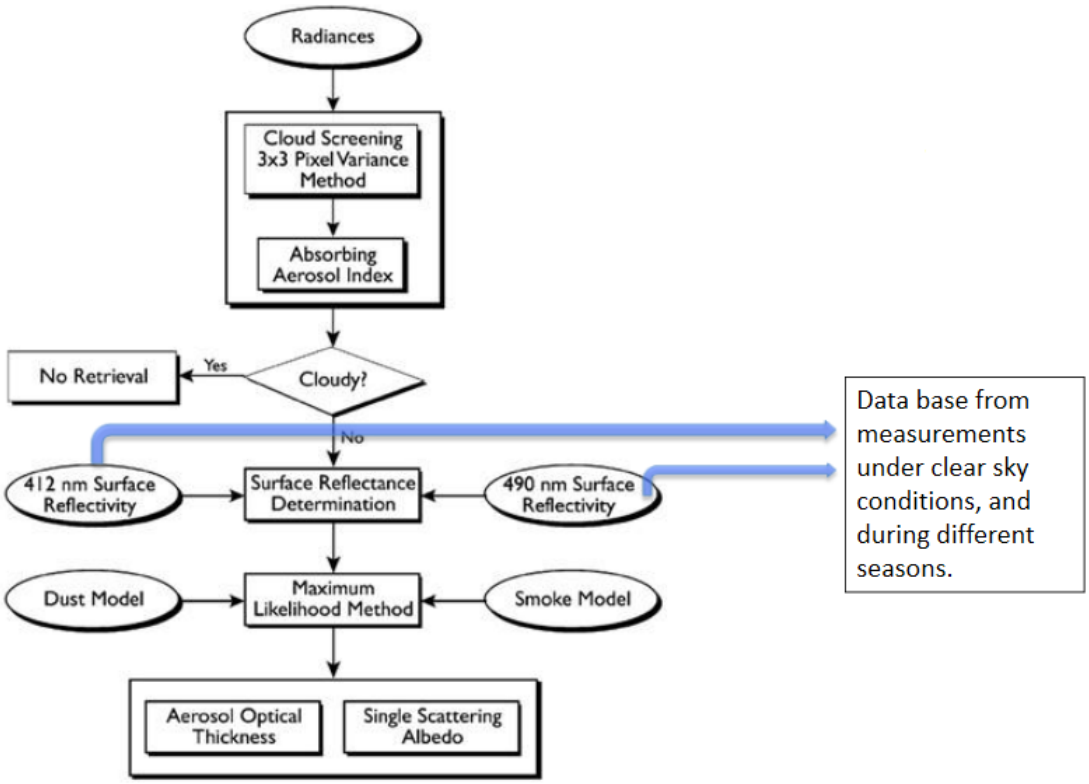

Figure 2.8 The DB AOD retrieval algorithm (Source: Hsu et al., 2004)

2.3 PM2.5-AOD Estimation Models

2.3.1 Input Variables

Before selecting PM2.5-AOD estimation models, it is important to choose relevant variables into the models. Previous studies have implemented meteorological and supplementary variables (such as socio-economic, land use and transportation information) for model construction. It is found that variables associated with PM2.5 could change within a short time (Mirzaei et al., 2018).

Meteorological factors are found to have significant impacts on the formation and dispersion of PM2.5. PM2.5 could disperse by wind advection. When the wind speed is low (below 3 m/s), PM2.5 will be blown away within a certain range. However, higher wind speed will accelerate the movement of PM2.5 within a certain time (Wang & Ogawa, 2015). It is found that a rising relative humidity will enhance the absorption of PM2.5 in the atmosphere, and thereby increasing atmospheric PM2.5 levels (Zhang & Jiang, 2018). In addition, the higher temperature might change surface pressure and affect the chemical reactions between gases in the atmosphere, which accelerates the generation of the secondary ions. Precipitation can

reduce PM2.5 levels by wet composition, since PM2.5 and small particles can be effectively removed during the process of precipitation (Wang & Ogawa, 2015). Furthermore, the amount of PM2.5 transported depends on the different wind directions (Wang & Ogawa, 2015). Also, PM2.5 will result in a low visibility due to the adsorption and scattering of lights (Li, 2016). Planetary boundary layer height (PBLH) is the lowest height of the atmosphere, and is considered as a significant variable for the formation of PM2.5 (Du et al., 2013). Qu et al. (2017) found that PBLH has a positive correlation with relative humidity. If the relative humidity is high, then the PBLH and PM2.5 concentrations would be high as well. The more stable the PBLH is, the higher PM2.5 concentrations will be (Qu et al., 2017).

Except for meteorological factors, socio-economic and land use information are important to the study of PM2.5 concentrations since human activities have caused serious impacts on PM2.5. Therefore, socio-economic factors such as population and gross domestic product (GDP), land use/land cover information, road networks, and transportation data are used as indicators to conduct models (Yang et al., 2017; Jiang et al., 2018).

2.3.2 Simulation-based Models

Chu et al. (2016) reviewed 116 journal articles related to PM2.5-AOD prediction models, and summarized the four widely used models were: Multiple Linear Regression (MLR), Mixed-Effect Model (MEM), Chemical Transport Model (CTM), and Geographically Weighted Regression (GWR). Among those models, CTM is the simulation-based model, whereas the other three are all statistical models (Table 2.5).

Simulation-based models are based on a global 3D chemical transport model (CTM) for atmospheric composition driven by meteorological input from the Goddard Earth Observing System (GEOS) of the NASA Global Modeling and Assimilation Office (GEOS-Chem). Later in 2006, CTM was firstly proposed by van Donkelaaar et al. (2006) by combining AOD composition and emission patterns. The principle of CTM is to simulate the transmission of PM2.5 and predict its potential concentration (Zhang et al., 2018). The Community Multiscale Air Quality (CMAQ) model, the Comprehensive Air Quality Model with Extensions (CAMx), and the Weather Research and Forecasting Model with Chemistry (WRF-Chem) are three commonly used third-generation CTMs to estimate PM2.5 concentrations.

CMAQ takes complicated chemical and physical processes into consideration, and describes the integration of the atmosphere. As a result, meteorological factors, spatial and temporal distributions, and PM2.5 evolution processes could be obtained using CMAQ (Zhang et al., 2018). CAMx integrates various variables into a single system utilized by the air-mass model to simulate the distribution of PM2.5

(Wagstrom & Pandis, 2011). WRF-Chem is the latest CTM model so far. The biggest difference between WRF-Chem and other CTM models is that the meteorological and transmission mode is completely matched on both spatial and temporal scales (Molders et al., 2012). All these three CTMs are widely applied to estimate PM2.5 in some studies (Grell et al., 2005; Wu et al., 2013; Zhang et al., 2018).

CTM could be used for a large spatial coverage especially on a global scale. It is able to integrate chemical and physical processes for modeling (Murray et al., 2018). In addition, CTM allows PM2.5 predictions without ground station-based PM2.5 data, which makes it highly applicable in areas lacking ground monitoring stations. (Zheng et al., 2016). However, CTM costs high expense, and it is time-consuming for collecting required chemical and physical information (van Donkelaar et al., 2010). Furthermore, CTM requires emission data, which will result in the situation of insufficient data in some less developed countries (van Donkelaar et al., 2014).

2.3.3 Statistical Models

The general expression of a simple two-variable linear equation is shown by:

$$\boldsymbol{PM2.5 = C + M \times AOD} \tag{2-1}$$

where *PM2.5* is the ground-level PM2.5 concentration, *AOD* is the MODIS AOD at 550 nm, *M* is the coefficient of AOD, and C is the intercept (Gupta & Christopher, 2009). In this model, PM2.5 is treated as the dependent variable, and AOD is the independent variable. Wang and Christopher (2003) conducted a linear regression model in the United States, and indicated that the correlation between satellite-derived AOD and PM2.5 is good. Since PM2.5 is affected by various factors other than AOD, the following Multiple Linear Regression (MLR) model was proposed to predict PM2.5 by inputting meteorological variables into the model:

$$PM2.5 = C_1 + C_2 \times AOD + C_3 \times V_3 + ...+ C_n \times V_n \tag{2-2}$$

where *PM2.5* is the ground-level PM2.5 concentration, AOD is the MODIS AOD at 550 nm, C_1 is the intercept of MLR, whereas C_2 - C_n represents the coefficients of corresponding predictor variables including AOD and V_3 - V_n (such as RH, temperature, PBLH, wind speed, precipitation, etc.). Liu et al. (2005) used MLR to estimate PM2.5 in the eastern United States and found that R^2 varied among different landscapes. They also pointed out that the selection of input meteorological factors needs further discussion due to low R^2 values. In order to improve the model performance, MLR normally adopted other than the simple linear regression model. However, the meteorological data used by MLR has relatively low accuracy and

resolution; and is not suitable for regional studies (Chu et al., 2016). In addition, some important variables are missing from the model, such as seasonal and regional variation (Han et al., 2015).

Most statistical models assume global geographic uniformity and ignore the spatial and local variability, which lead to inaccurate PM2.5 predictions because of the non-stationary correlation between PM2.5 and AOD (Li, 2016). The Geographically Weighted Regression (GWR) model was proposed to take local variations into consideration so that the coefficients in the model could be estimated in specific locations rather than on a global scale (Brunsdon et al., 1996). GWR can be expressed as:

$$PM2.5_{ij} = C_{0,ij} + C_{1,ij}AOD_{ij} + C_{2,ij}V_{2,ij} + C_{3,ij}V_{3,ij} + \ldots\ldots + C_{n,ij}V_{n,ij} \quad (2\text{-}3)$$

where $PM2.5_{ij}$ is the ground-level PM2.5 concentration at location i on day j, $C_{0,ij}$ is the intercept at location i on day j, AOD_{ij} is the MODIS AOD at 550 nm at location on a day j, and $C_{2,ij}$ to $C_{n,ij}$ are coefficients of corresponding independent variables $V_{2,ij}$ to $V_{n,ij}$ at a location on day j (Brunsdon et al., 1996). Hu et al. (2011) put AOD, meteorological variables and land use information into GWR model to predict PM2.5 in North America. The result exhibited an R^2 value of 0.706, which indicated a successful implementation of GWR. The most important step when operating a GWR model is to choose the appropriate bandwidth, which could be selected using cross validation (CV) or Akaike information criterion (AIC) (Zhang et al., 2018). The GWR model could generate higher R^2 values than the MLR and the CTM under certain conditions (Chu et al., 2016). Since the construction of the GWR relies on the ground-level monitoring data, it would be insufficient in the area with limited monitoring stations (Chu et al., 2016).

Mixed-Effect Model (MEM) generates PM2.5 using random intercepts and slopes instead of calculating PM2.5-AOD slopes for each day (Lee et al., 2011). MEM can be expressed as:

$$PM2.5_{ij} = (\alpha + u_j) + (\beta + v_j) \times AOD_{ij} + s_i + \varepsilon_{ij} \quad (u_j\, v_j) \sim N[(00), \sum] \quad (2\text{-}4)$$

where $PM2.5_{ij}$ is the ground-level PM2.5 concentration at location i on day j, AOD_{ij} is the MODIS AOD at 550 nm at location i on day j, α and u_j are fixed and random intercepts corresponding to fixed β and random v_j slopes, respectively, s_i is the random intercept at location I, ε_{ij} is the error term at location i on day j, and $\sum$ is the variance-covariance matrix for the day-specific random effects (Lee et al., 2011). By adding random effects into MEM model, it is possible to explain the daily PM2.5-AOD variation (Kloog et al., 2011). A limitation of MEM is that due to the lack of ground monitoring stations, the requirement of Kriging might not be met, which will lead to inaccurate results (Chu et al., 2016).

Table 2.5 Summary of commonly used PM2.5-AOD estimation models

Type	Model	Strength	Weakness	Reference
Simulation-based Model	GEOS-CHEM	Integrate chemical and physical processes for modelling; Allow PM2.5 predictions without ground station-based PM2.5 data	High expense; Time-consuming; Complex operation	Liu et al. (2004)
	CMAQ			Zhang et al. (2018)
	CAMx			Wagstrom & Pandis (2011)
	WRF-Chem			Molders et al. (2012)
Statistical Model	Multiple Linear Regression (MLR)	More factors are taken into consideration	Low accuracy and resolution meteorological data used by MLR, not suitable for regional studies	Liu et al. (2005)
	Geographically Weighted Regression (GWR)	take local variations into consideration	insufficient in area with limited monitoring stations	Brunsdon et al. (1996)
	Mixed Effects Model (MEM)	By adding random effects into MEM model, it is possible to explain daily PM2.5-AOD variation	Some information is hard to collect	Lee et al. (2011)
	Land Use Regression (LUR)	It is often used to analyze air pollution in densely populated area	Low temporal resolution; Not suitable for short-term study	Mirzaei et al. (2018)
	Nonlinear Regression (NLR)	Be able to describe non-linear relationship between variables; computing intensity does not exist	Limited spatial or seasonal variations	Cobourn (2010)
	Generalized Additive Model (GAM)	Be able to describe non-linear relationship between variables	Local diversity is not considered	Li et al. (2017)
	Two-stage Model (TSM)	Combine advantages of two models	Inaccurate results of first stage model will lead to major bias for the second stage model	Hu et al. (2014)
Machine Learning-based Model	BP Artificial Neural Network (ANN)	It is suitable for a set of observation data with no clear descriptive theory	High probability of computing intensity	Wu et al. (2011)
	Random Forests (RF)			Breiman (2001)
	Support Vector Regression (SVR)			
Theoretical Model		Aerosol characteristics are taken into account	Relatively low accuracy since models are built based on assumptions	Li et al. (2015)

In addition to the models mentioned above, various models are developed based on the spatial variation. Land use regression (LUR) model integrates land cover, population, and traffic information to estimate PM2.5 concentrations (Mao et al., 2011). LUR is often used to analyze air pollution in a densely populated area. LUR can be expressed as:

$$PM2.5_i = \beta_0 + \Sigma \beta_k x_{ik} + \varepsilon_i \quad (2\text{-}5)$$

where *PM2.5* is the ground-level PM2.5 concentration at location i, x is the independent variables (Mirzaei et al., 2018). Mirzaei et al. (2018) estimated PM2.5 in Alberta during the wildfire season using LUR, and the results showed model performance was highly related to PM2.5 concentrations. Nonlinear regression model and Generalized Additive Model (GAM) allow nonlinear regression between independent and dependent variables (Liu et al., 2007). However, those models are proven to have lower R^2 values. Therefore, optimization and integration of those models are implemented to improve model performance. For instance, two stage model (TSM) is used in several studies to predict PM2.5. Furthermore, artificial neural networks (ANN) and machine learning regression models, such as BP ANN-based analysis, random forests (RF), and support vector regression (SVR) methods are utilized to estimate PM2.5 in order to reduce uncertainties of statistical models by simulating biological neutral networks using computer algorithms (Chen et al., 2014).

Statistical models normally generate high R^2 in predicting PM2.5 concentrations. However, the overestimation of low PM2.5 concentrations or the underestimation of high PM2.5 concentrations happen sometimes, because statistical models are difficult to predict random events (Gupta et al., 2009).

2.3.4 Theoretical Models

Theoretical models are based on the theoretical relationship between PM2.5 and various AOD parameters (such as meteorological and physical parameters). Theoretical models take aerosol properties into consideration. However, theoretical models are difficult to implement, because it is hard to find a fixed physical correlation between PM2.5 and AOD. In addition, since theoretical models are based on assumptions, the accuracy of the model is relatively low. Lin et al. (2015) generated an indicator to describe the absorptive humidity growth rather than using a traditional humidity effect to estimate PM2.5. Zhang and Li (2015) utilized the statistical relationships between meteorological variables to evaluate the physical correlations among different optical-masses. Liu (2018) proposed a new theoretical model which put particle radius into considerations. Liu's model improved the AOD coverage, and could be implemented on a large scale (national) since it did not require parameters with regional characteristics.

2.4 Wildfire and PM2.5 Studies in Canada

PM2.5-AOD estimation studies have been conducted in Canada since the 21th century (Table 2.6). Wallace and Kanaroglou (2007) adopted the MLR model combined with MODIS and MISR AOD data to investigate PM2.5 concentrations in southern Ontario. Temperature, wind speed, and relative humidity were also used as predictors of PM2.5. It generated an R^2 of 0.76 for this study. Tian and Chen (2010) built a semi-empirical model to predict hourly PM2.5 concentrations in southern Ontario using MODIS AOD and meteorological data. The R^2 of the model was 0.65, which means the model was able to explain 65% variability in PM2.5. Hystad et al. (2011) used the LUR model to estimate PM2.5 concentrations in seven Canadian cities, and the R^2 was only 0.46. Hystad et al. (2012) estimated PM2.5 concentrations using the CTM model, and generated a higher R^2 of 0.67. Crouse et al. (2016) also implemented the CTM model combining MODIS, MISR, and SeaWIFS AOD to estimate PM2.5 concentrations in Canada, which generated an R^2 of 0.58. Stieb et al. (2016) examined the impacts of PM2.5 using the LUR model on a national scale in Canada, and computed an R^2 of 0.59. Wang et al. (2016) analyzed ground-level PM2.5 in the City of Montreal using the one of the CTM models (GEOS-Chem), and achieved an R^2 of 0.86.

Table 2.6 Summary of PM2.5 studies conducted in Canada in recent years

Reference	Study Area and Period	Source of AOD	PM2.5-AOD Model	R^2
Wallace and Kanaroglou, 2017	Southern Ontario, 2005	MODIS, MISR	MLR	0.76
Tian et al., 2010	Southern Ontario, 2004	MODIS	Semi-empirical model	0.65
Hystad et al., 2011	National scale, 2006	MODIS, MISR	LUR	0.46
Hystad et al., 2012	National scale, 1975-1994	MODIS, MISR	CTM	0.67
Crouse et al., 2016	National scale, 2001-2010	MODIS, MISR, SeaWIFS	CTM	0.58
Stieb et al., 2016	National scale, 1999-2008	MODIS	LUR	0.59
Wang et al., 2016	Montreal, 2009	MODIS	CTM	0.86

As discussed in Section 1.1.6, wildfire is a major source of PM2.5 in Canada. Several studies have been conducted to examine the relationship between wildfire and PM2.5. Sofowote and Dempsey (2015) analyzed three wildfire events in July of 2011, 2012, and 2013 to identify the major source of high PM2.5 concentrations during the study period. It is found that the regions with active fires tend to display higher PM2.5 concentrations by examining the near-real-time ground-level PM2.5 data. In order to explore the health impact of wildfire smoke, Mirzaei et al. (2018) integrated the LUR model and MODIS AOD products to estimate PM2.5 concentrations in southern Alberta, Canada affected by wildfires in the northwest of the United States in the summer of 2015. They distinguished PM2.5 from other sources by dividing the study period into three sub-periods, including pre-fire, during-fire, and post-fire. NDVI, AOD products from MODIS and OMI, meteorological predictors (relative humidity, temperature, and wind speed), distance to the source of fire, and land use of industrial roads were utilized to build the model. The R^2 of the LUR model was 0.50 for this study. An important contribution of this study was that it could evaluate PM2.5-related health impacts before and after wildfire by analyzing estimated PM2.5 distribution maps. In 2019, Mirzaei et al. (2019) used the OLS and the GWR model to estimate PM2.5 concentrations in Alberta affected by wildfires derived from BC in August 2017. Other than AOD and meteorological variables, numerous variables were taken into consideration, such as distance from fire in BC, and road length around each ground station. The R^2 values of the OLS and the GWR model were 0.74 and 0.84, respectively. The results indicated that the GWR model generated more accurate results than the OLS model. In addition, this study was also valuable for further studies to assess the health impact of wildfire plumes.

2.5 Chapter Summary

Air quality monitoring networks have been established in many countries to regulate air pollutants, including PM2.5. However, the distribution of PM2.5 ground monitoring stations is uneven. Therefore, remote sensing techniques have been implemented to predict PM2.5 concentrations. Previous studies have proven the existence of a strong correlation between PM2.5 and AOD. As a result, satellite-derived AOD is used to estimate PM2.5 since the 1970s. Various sensors and algorithms have been used to retrieve AOD, and the most widely used is MODIS, which adopts DT and DB algorithms to retrieve AOD. Ground-level AERONET AOD is used to validate MODIS AOD. Simulation-based and statistical models are utilized to estimate PM2.5 using AOD as the independent variable. Meteorological, socio-economic, land use/land cover, traffic, and other supplementary variables are taken into considerations when conducting the models. Several studies related to wildfire and PM2.5 were conducted in Canada before, which proves the research necessity of PM2.5 concentrations during the wildfire.

Chapter 3 Study Area and Data

3.1 Study Area

British Columbia (BC) is the westernmost province of Canada, which located between the Pacific Ocean and the Rocky Mountain. BC is composed of 27 regional districts, with a total estimated population of 5.016 million in 2018, which is the third populous province in Canada after Ontario and Quebec.

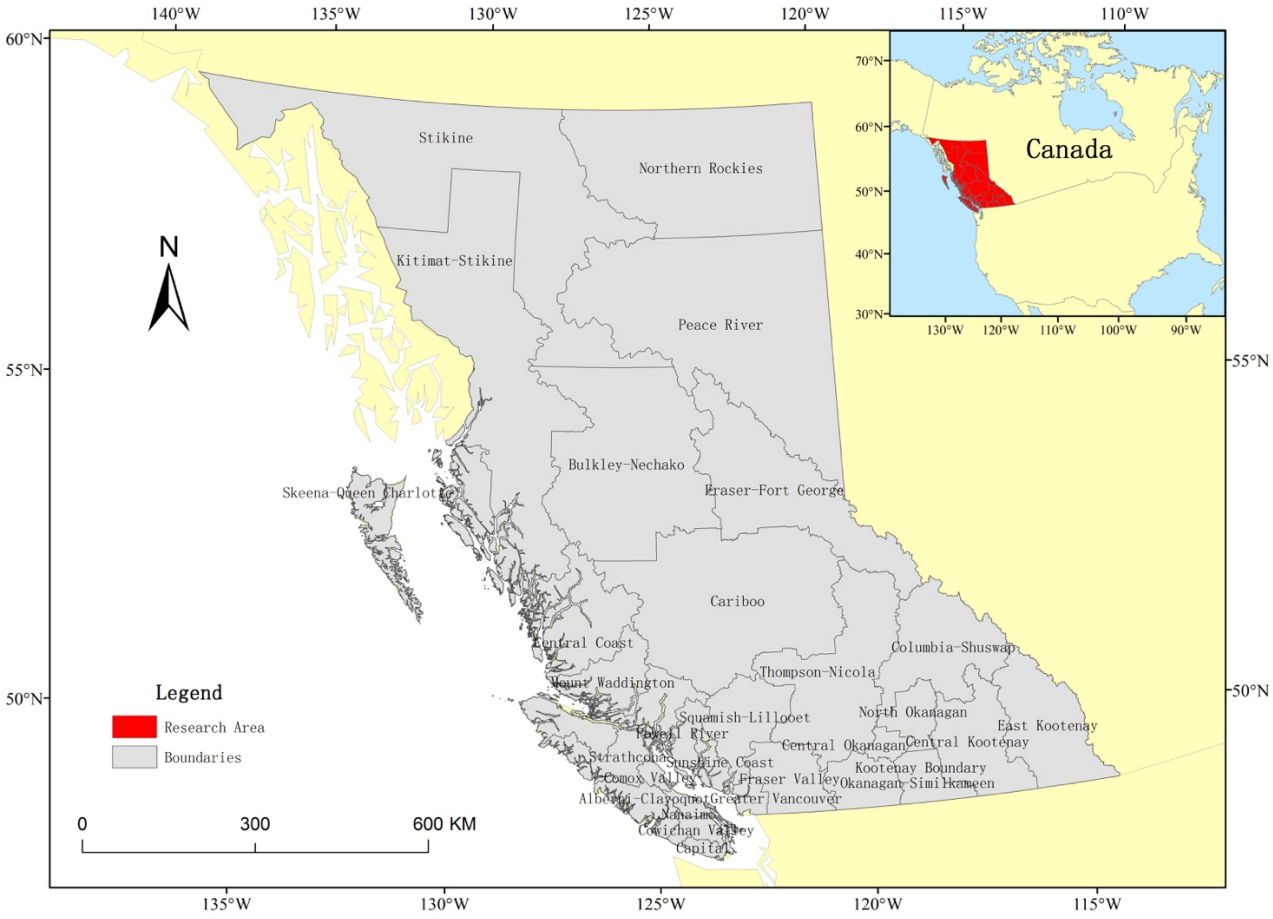

Figure 3.1 Study area

Figure 3.1 displays the geographical location of BC. The total area of BC is 944,735 km^2, which is ranked as the fifth largest province in Canada. The latitude and longitude of BC are 53° 43' 36.0084" North and 127° 38' 51.4356" West, respectively. The west part of BC is bounded to the Pacific Ocean. The northern, eastern, and southern regions of BC are bordered by the Yukon and Alaska, Alberta, and the

United States., respectively. It is reported that BC has experienced a rapid population growth in the past three years due to its pleasant climate and diverse culture. Some places in BC even have the highest population density in Canada, such as the City of Vancouver. BC is famous for its rich natural resources, mountainous terrain, abundant forests, unique coastline, and numerous water resources (Ministry of Forest, n.d). Around 70% of BC's total area is covered by mountains, and forests account for 60% among the mountainous area (Figure 3.2). The agricultural area only occupies 5% of BC's total area. Therefore, BC's economy mainly relies on the logging industry and tourism (Ministry of Forest, n.d.). Due to both natural (such as lightning) and human-caused reasons, wildfires in BC have been increasing year by year. Details of BC's wildfires in 2017 are introduced in Section 1.1.6.

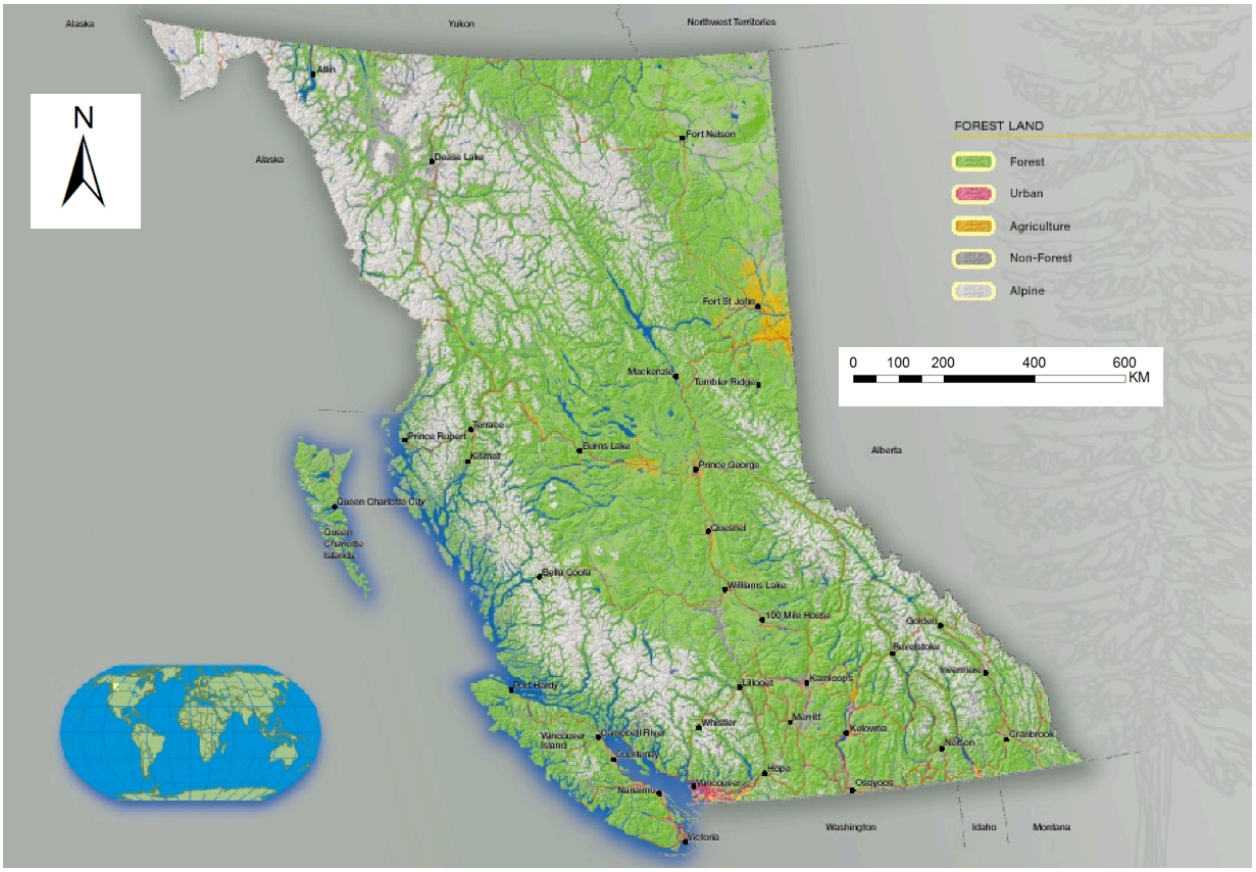

Figure 3.2 Forest cover in British Columbia (Source: Ministry of Forest, n.d.)

3.2 Data

3.2.1 MODIS AOD Data

The 3 km MODIS Level-2 aerosol products were obtained from Level-1 and Atmosphere Archive and Distribution System (LAADS) (https://ladsweb.modaps.eosdis.nasa.gov). Both MODIS-Aqua and MODIS-Terra provide aerosol products in 3 km and 10 km resolutions, and their products are recognized as MYD04 and MOD04, respectively. It has been proven that compared to the Terra MODIS, the Aqua MODIS reveals small calibration changes (Wang, 2017). Therefore, only MODIS-Aqua products were used in this study. The Aqua passes the study area around 13:30 at local time. In addition, since BC is a relatively smaller scale (regional), the new-released 3 km MODIS AOD products in 2013 were suitable for study. Normally the 3 km products are able to display more details of AOD variations. The reasons of blank grids in images include cloud, snow, ice cover, and mistakes of the retrieval algorithm itself. Those blank grids could be identified using the true color image. Furthermore, 60% of BC's total area is covered by forests, the DT algorithm was adopted to retrieve AOD over dark surfaces rather than the DB. As a result, the 3 km MODIS-Aqua DT products at 550 nm were used for this study. The retrieval procedure of the DT algorithm has been introduced in Section 2.2.3.2.

MODIS AOD products are stored as Hierarchical Data Format-Earth Observing Systems (HDF-EOS). Normally, a MODIS HDF dataset is comprised of several Science Data Sets (SDS) with different levels of Quality Assurance (QAC) flags. QAC was designed by NASA to describe the quality of MODIS AOD datasets. QAC ranges from 0 to 3 in MODIS C6.1 (Table 3.1). QAC = 3 represents the highest quality products over land. Therefore, for this study, only products with QAC = 3 were used (SDS name: 'Optical_Depth_Land_And_Ocean').

Table 3.1 QAC flags of MODIS AOD products

QAC Flags	QAC Confidence
0	Bad or No Confidence
1	Marginal
2	Good
3	Very Good

3.2.2 AERONET AOD Data

AERONET AOD products were generated to validate MODIS AOD retrievals, since AERONET AOD has five times higher accuracy than the satellite-derived AOD (https://aeronet.gsfc.nasa.gov). There are four AERONET sites in BC, but only two of them were operational during the study period (Table 3.2). Thus, AERONET AOD from Kelowna_UAS and Saturn_Island sites were utilized to validate MODIS AOD data.

Table 3.2 AERONET Sites in BC

Site	Latitude	Longitude	Operational Dates
Kelowna_UAS	49.941N	119.400W	1 January 2004 - 31 December 2018
Saturn_Island	48.775N	123.128W	1 January 1997 - present
Lochiel	49.028N	22.602W	1 January 2001 - 31 December 2001
Kelowna	49.955N	119.373W	1 January 2018 - present

AERONET includes three levels of AOD products: Level 1.0 (unscreened), Level 1.5 (cloud-screened and quality controlled), and Level 2.0 (cloud-screened and quality-assured). Pre-field and post-field calibration were applied to Level 2.0 AERONET AOD data. In this study, only Level 2.0 AERONET AOD products were adopted as the reference data to evaluate MODIS AOD retrievals.

3.2.3 Ground-level PM2.5 Data

BC's hourly ground-level PM2.5 measurements in 2017 were acquired from 66 ground stations through the BC Open Data Catalogue (https://catalogue.data.gov.bc.ca/dataset). BAM1020 is the main instrument to measure PM2.5 in these stations. Figure 3.4 displays the distribution of these ground stations, as well as their annual averages of PM2.5 concentrations during the study period. It can be seen that most ground stations are concentrated in urban areas, and the distribution is extremely uneven between different regions. Most forest regions lack ground monitoring stations, which makes it difficult to measure PM2.5 during the wildfire season.

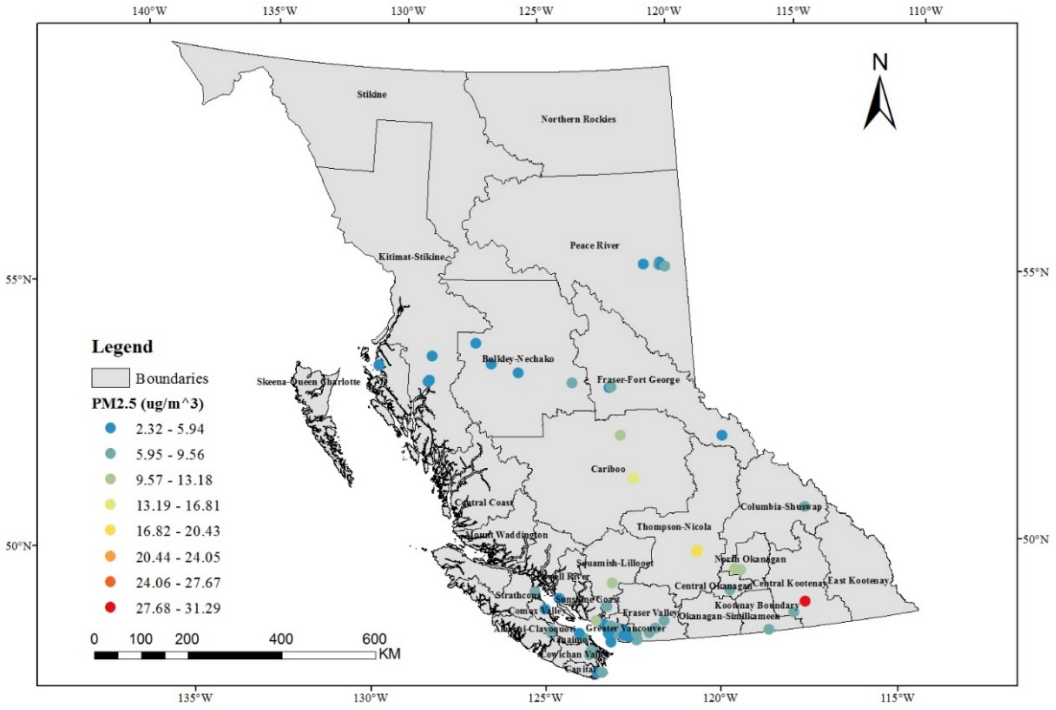

Figure 3.3 Distribution of PM2.5 ground monitoring stations and their annual PM2.5 concentrations in BC during the study period

According to the CAAQS standard, the annual national standard for PM2.5 is 10 μg/m^3. And the standard in BC is stricter, the annual standard for PM2.5 is 6 μg/m^3. Most area in BC meets the national standard, but fail to meet the regional standard. Wildfires are considered to be responsible for a high level of PM2.5 in BC. Details of these ground stations include station name, station ID, longitude, latitude, and annual mean PM2.5 concentrations are introduced in Appendix A. Ground-level PM2.5 datasets used in this study were verified by BC's Ministry of Environment, and have been validated through a Quality Assurance (QA) or Quality Control (QC) process. In order to match Aqua's passing time at 13:30, averaged PM2.5 concentrations between 13:00 and 14:00 were extracted.

3.2.4 Meteorological Data

Meteorological data include planetary boundary layer height (PBLH), relative humidity, surface pressure, u wind speed, v wind speed, temperature, and visibility were incorporated in this study. PBLH, relative humidity, surface pressure, u wind speed, v wind speed, and temperature datasets were generated from the European Centre for Medium-Range Weather Forecasts (ECMWF) reanalysis datasets (ERA-Interim)

(https://apps.ecmwf.int/datasets/data/interim-full-daily). Visibility datasets were acquired from the NCEP ADP Global Surface Observational Weather Data (https://rda.ucar.edu/datasets/ds461.0/). Table 3.3 summarizes the meteorological data used in this study.

The ERA-Interim contains both analysis and forecast datasets. Analysis datasets are provided in four different times at 00:00, 06:00, 12:00, and 18:00. Forecast datasets are available at 00:00 and 12:00 with different steps to choose from. Step 3 means only forecast datasets could be generated starting from either 00:00 or 12:00 with 3 hours forecast, which means datasets at 03:00 or 15:00 will be collected. Step 0 represents the real-time analysis dataset. For this study, in order to match the MODIS AOD product acquired at 13:30, all meteorological datasets were acquired at 12:00. Since Step 0 datasets for PBLH, relative humidity, and visibility were not available, Step 3 datasets were generated for these three variables, which records their values at 15:00. The spatial resolution for meteorological data is 0.125º. Figure 3.5 displays the spatial annual mean values of these meteorological factors.

Table 3.3 Descriptions of meteorological data used in this study

Meteorological Factors	Unit	Acquired Time	Spatial Resolution	Step	Description
Planetary Boundary Layer Height	m	12:00	0.125°	3	The depth of atmosphere next to the Earth's surface
Relative Humidity	%				Relatively humidity at 1000 hPa pressure level
Surface Pressure	Pa			0	Pressure of the atmosphere on the land surface
U Wind Speed	m/s				Horizontal air moving speed at 10 meters towards the east
V Wind Speed	m/s				Horizontal air moving speed at 10 meters towards the north
Temperature	K				Temperature in the atmosphere at 2 meters
Visibility	m			3	Visibility on the surface

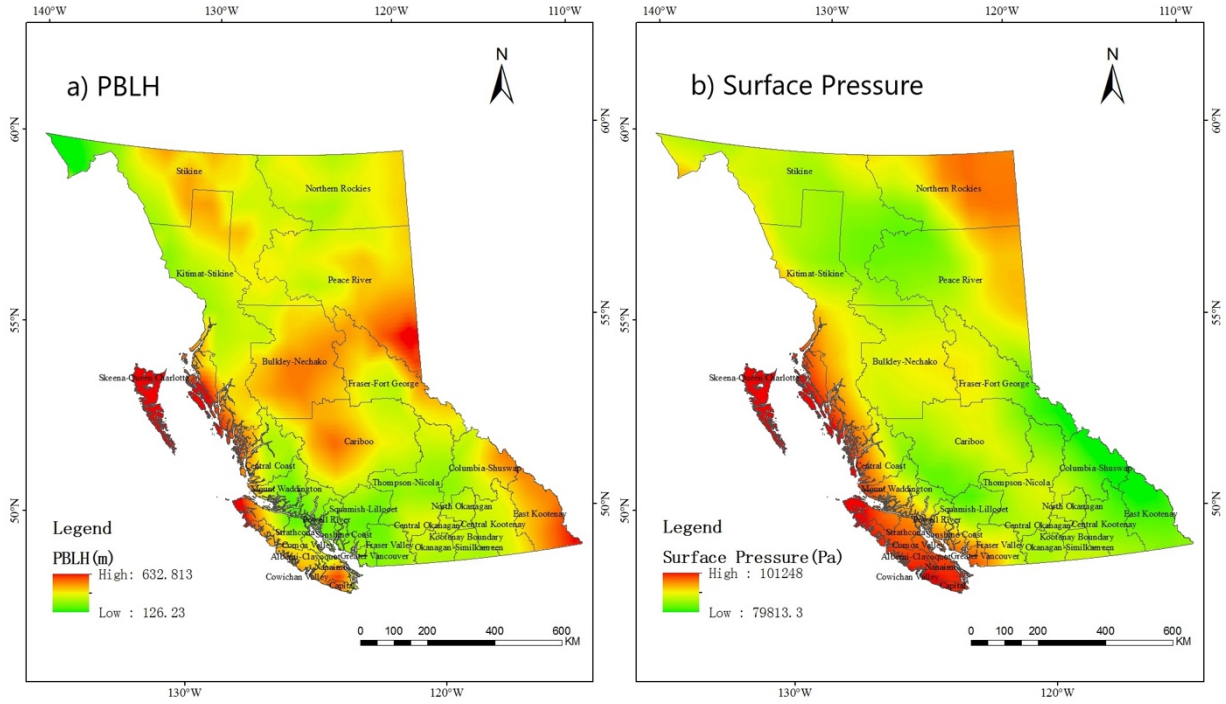
a) PBLH
b) Surface Pressure
c) Temperature
d) Relative Humidity
N
140°W
130°W
120°W
110°W
60°N
55°N
50°N
Stikine
Northern Rockies
Kitimat-Stikine
Peace River
Bulkley-Nechako
Fraser-Fort George
Cariboo
Central Coast
Columbia-Shuswap
Thompson-Nicola
Mount Waddington
Squamish-Lillooet
North Okanagan
East Kootenay
Powell River
Central Okanagan
Central Kootenay
Strathcona
Sunshine Coast
Kootenay Boundary
Comox Valley
Fraser Valley
Okanagan-Similkameen
Alberni-Clayoquot
Greater Vancouver
Nanaimo
Cowichan Valley
Capital
Legend
PBLH(m)
High: 632.813
Low : 126.23
Surface Pressure(Pa)
High : 101248
Low : 79813.3
Temperature(K)
High : 284.072
Low : 267.764
Relative Humidity(%)
High : 93.3583
Low : 79.3098
0 100 200 400 600
KM

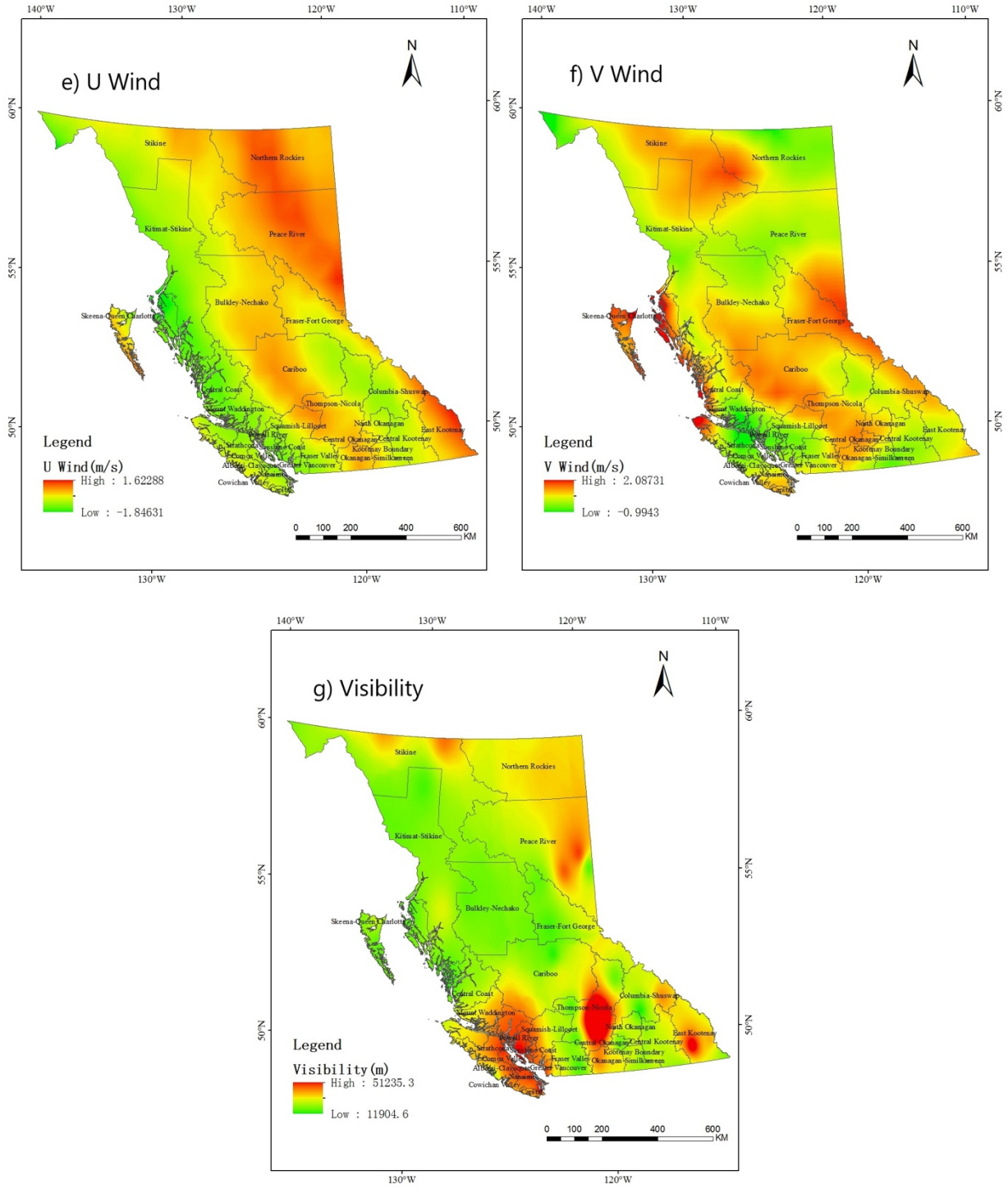

Figure 3.4 Spatial annual mean distributions of seven meteorological factors used in this study: (a) PBLH, (b) surface pressure, (c) temperature, (d) relative humidity, (e) u wind speed, (f) v wind speed, and (g) visibility

As shown in Figure 3.4, the average PBLH ranges from 126 m to 632 m, the highest values are distributed on the island and coastal areas. Most area in BC has high relative humidity with 90% in values. The lowest u wind and v wind speed are both negative (-1.85 m/s and -0.99 m/s respectively). A negative value of the wind speed means the wind is from the opposite direction. The distribution of the surface pressure and the temperature is similar to the PBLH, since the highest values are clustered around the island and coastal regions (101248 Pa and 284.07 K, respectively). For the visibility, it shows that the lows values are concentrated on regions covered by forests.

3.2.5 Supplementary Data

Various supplementary datasets were generated in this study for analysis. Monthly NDVI products (MYD13C2) were acquired from the U.S. Geological Survey (USGS) (https://earthexplorer.usgs.gov/). Since the vegetation cover does not change frequently, instead of using the 16-day NDVI products, monthly NDVI products with 0.05° resolution were selected for this study. The 1 km resolution elevation data were derived from the DEMs provided by Natural Resources Canada (https://open.canada.ca/data). Figure 3.5 displays the spatial distribution of these two datasets.

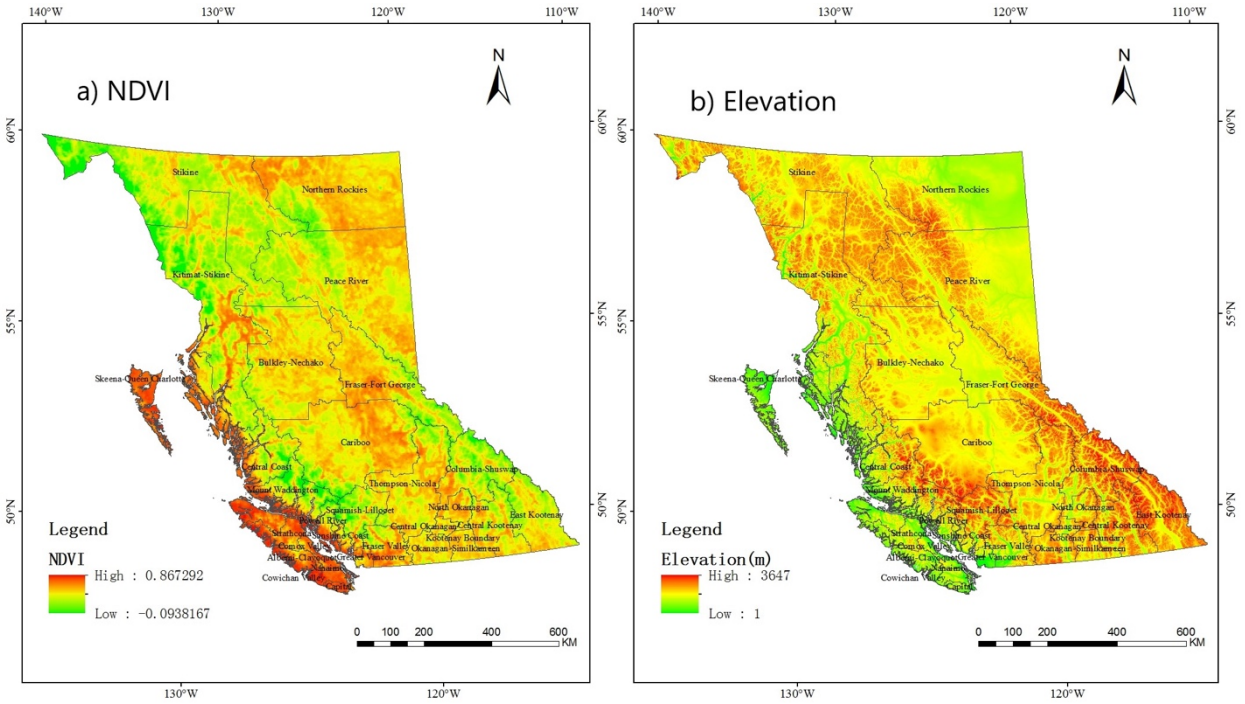

Figure 3.5 Spatial distribution of supplementary factors used in this study: (a) NDVI and (b) elevation

In addition, the 2017 active wildfire distribution map during the wildfire season in BC was obtained from BC Wildfire Service to validate the application feasibility of MODIS AOD products and PM2.5-AOD models regarding wildfires (https://governmentofbc.maps.arcgis.com).

3.3 Chapter Summary

Overall, since forest area accounts for 60% of BC's total area, wildfires have always been a serious problem due to both natural and anthropogenic reasons. The smoke from wildfires releases air pollutants and is harmful to human health and air quality. The 3 km MODIS AOD products were used to conduct PM2.5-AOD models by combining ground monitoring PM2.5 data, meteorological data, and supplementary data. The active wildfire map in BC was also acquired as supporting documents for this study.

Chapter 4 Methodology

Chapter 4 presents the methodology of this study. Section 4.1 provides an overview of the methodology, as well as the workflow chart. Section 4.2 presents the MODIS AOD validation method. Section 4.3 explains the process of data preprocessing. Section 4.4 explains how the models will be built. Section 4.5 describes the output analysis. Section 4.6 summarizes the chapter.

4.1 Overview of the Methodology

The methodology of this study could be divided into four parts, including MODIS AOD validation, data preprocessing, model construction, and output analysis. Figure 4.1 displays the workflow of the methodology. The first part is the MODIS AOD validation. AERONET AOD was used to validate with MODIS AOD after temporal and spatial matching. For the second part of the methodology, all datasets were preprocessed including projection, clipping, and resampling. The ground-level PM2.5 measurements were then used to match with MODIS AOD, meteorological variables, and supplementary data. After the removal of invalid matchings, the third step is the construction of models. The output of the second step were used to build models. The MLR, the GWR, and a theoretical model were conducted. Validations were implemented for each model. Then, the comparison between the three models was generated. The model with the best prediction performance was used to build monthly and seasonal models. Lastly, the output of the models was analyzed, as well as the application feasibility of MODIS AOD during the wildfire season in BC.

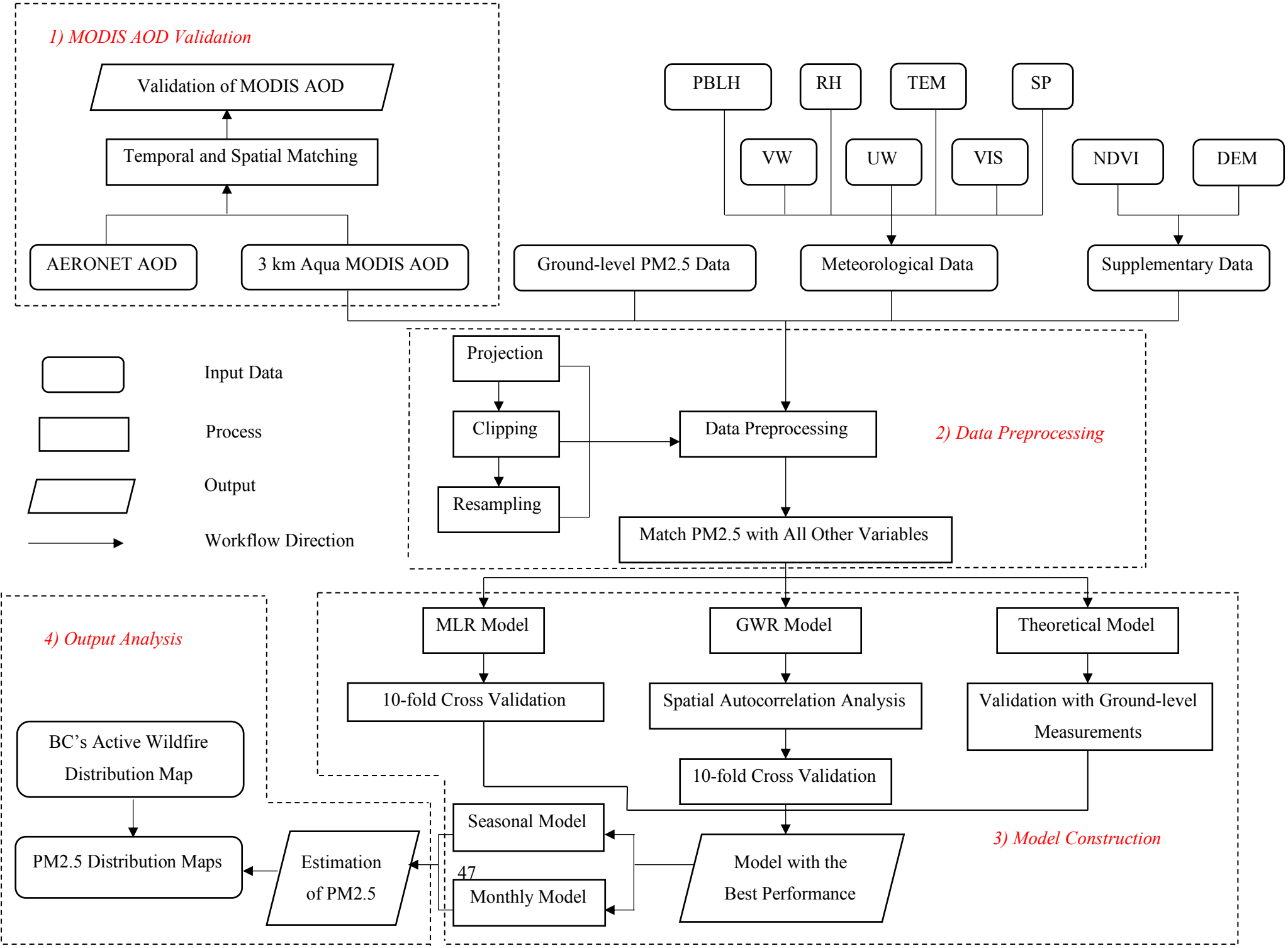

Figure 4.1 Workflow of the methodology

4.2 MODIS AOD Validation

AERONET AOD was used to validate MODIS AOD. MODIS AOD was retrieved at 550 nm wavelength. However, AERONET AOD was measured at 1640, 1020, 870, 675, 500, 380 and 340 nm wavelength in Kelowna_UAS and Saturn_Island sites. Thus, AERONET AOD was interpolated at 550 nm to match MODIS AOD's retrieval wavelength. The 675 nm wavelength was not used due to the failure of filters at BC's sites. According to Ångström (1964), aerosols satisfy the Junge distribution without the effect of the water vapour. The equation between AOD and wavelength could be expressed using the Ångström formula:

$$\tau(\lambda) = \beta\lambda^{-\alpha} \tag{4-1}$$

where $\tau(\lambda)$ is the AOD at wavelength λ; α is the Ångström exponent, which has a negative correlation with the radius of aerosols; β is the atmospheric turbidity coefficient, which is affected by the total number of aerosols and the spectral distribution. Assuming there are no water vapor effects at wavelength λ_1 and λ_2, Equations (4-2) and (4-3) could be generated according to Eq. (4-1):

$$\tau(\lambda_1) = \beta\lambda_1^{-\alpha} \tag{4-2}$$

$$\tau(\lambda_2) = \beta\lambda_2^{-\alpha} \tag{4-3}$$

Based on (4-2) and (4-3), the following equation is computed:

$$\alpha_{\lambda 1\text{-}\lambda 2} = -\frac{ln\,(\tau(\lambda 1)/\,\tau(\lambda 2))}{ln\,(\lambda 1/\,\lambda 2)} \tag{4-4}$$

where $\alpha_{\lambda 1\text{-}\lambda 2}$ is the Ångström component between wavelength λ_1 and λ_2. If λ_1, λ_2, and $\alpha_{\lambda 1\text{-}\lambda 2}$ are known, the AOD at any wavelength (λ') between λ_1 and λ_2 could be calculated using the interpolation:

$$\tau_{\lambda'} = \tau_{\lambda 1}\left(\frac{\lambda'}{\lambda 1}\right)^{-\alpha_{\lambda 1\text{-}\lambda 2}} \tag{4-5}$$

In this study, AERONET AOD at 500 nm was provided in both sites. The Ångström exponent between wavelength 440 nm and 870 nm ($\alpha_{440\text{-}870}$) was used to interpolate AOD at wavelength 550 nm:

$$\tau_{550} = \tau_{500}\left(\frac{550}{500}\right)^{-\alpha_{440\text{-}870}} \tag{4-6}$$

Since AERONET AOD and MODIS AOD have different spatial and temporal resolution, it is necessary to match them on both spatial and temporal scales before the validation. Based on previous studies, the averaged MODIS AOD within a 5 × 5 pixel window (15 km × 15 km) centered on AERONET AOD stations was extracted (Ichoku et al., 2002). For temporal matching, AERONET AOD ±30 min of

Aqua's overpassing time was used. Since MODIS AOD could not be collected every day due to cloud cover, and AERONET AOD products are not available every day during Aqua's overpassing time, therefore, after spatial and temporal matching, there were 55 collocations in the Kelowna_UAS site. For the Saturn-Island site, there was no collocation available during the study period. After checking with Google Map, it turned out that the Saturn_Island site was situated on an island in the Pacific Ocean. It is possible that MODIS AOD products used in this study might not cover this small island. It might be covered in the ocean product instead of the land product. Therefore, only 55 collocations in the Kelowna_UAS site were used for the validation.

A regression line was generated to represent the validation result between the MODIS AOD and the AERONET AOD:

$$\tau_{MODIS} = s \times \tau_{AERONET} + i \tag{4-7}$$

where τ_{MODIS} and $\tau_{AERONET}$ are the values of MODIS and AERONET AOD, s and i are the slope and intercept of the regression line, respectively. The Expected Error (EE) line was recognized as an important indicator to examine the accuracy of MODIS AOD products (Levy et al., 2010). The EE of the 3 km DT algorithm MODIS AOD product in C6.1 was defined the following equation by NASA (Wang et al., 2017):

$$EE = \pm (0.05 + 0.2\tau_{AERONET}) \tag{4-8}$$

In addition, the correlation coefficient R, the root mean square error (RMSE), and the mean absolute error (MSE) were used to evaluate the validation result:

$$RMSE = \sqrt{\frac{1}{n}\sum_{i=1}^{n}(\tau_{MODIS_i} - \tau_{AERONET_i})^2} \tag{4-9}$$

$$MAE = \frac{1}{n}\sum_{i=1}^{n} | \tau_{MODIS_i} - \tau_{AERONET_i} | \tag{4-10}$$

4.3 Data Preprocessing

Firstly, all raster datasets were projected, mosaicked, and clipped for the further research. The geographical coordinates used in this study were unified as *WGS84*. As stated in Chapter 4, datasets were acquired based on the Aqua's overpassing time in order to ensure temporal matching. Daily visibility datasets were stored as text files; thus, these text files were converted into raster datasets using the inverse distance weighting (IDW) interpolation method. Since satellite data, meteorological data, and supplementary data have different resolutions, therefore, the next step is to resample meteorological and supplementary datasets to 3 km using the bilinear interpolation in ArcGIS 10.6.1. After resampling, MODIS AOD, meteorological,

and supplementary data were used to match the ground-level PM2.5 monitoring data in a 5 × 5 pixel window centered on the ground stations. The averaged values of all variables in these pixels were extracted. Pixels with no AOD data matched were considered as invalid data and were removed. There were 1914 lines of valid recordings after the matching and removal.

4.4 Model Construction

4.4.1 Multiple Linear Regression Model

The MLR model used in this study could be expressed as:

$$PM2.5 = C_1 + C_{AOD} \times AOD + C_{PBLH} \times PBLH + C_{RH} \times RH + C_{TEM} \times TEM + C_{SP} \times SP + C_{UW} \times UW + C_{VW} \times VW + C_{VIS} \times VIS + C_{NDVI} \times NDVI + C_{DEM} \times DEM \quad (4\text{-}11)$$

where $PM2.5$ is the ground-level PM2.5 concentrations; C_1 is the intercept of the equation; C_{AOD}, C_{PBLH}, C_{RH}, C_{TEM}, C_{SP}, C_{UW}, C_{VW}, C_{VIS}, C_{NDVI}, C_{DEM} are the coefficients of their corresponding independent variables; AOD is the MODIS AOD values; $PBLH$ is the value of the planetary boundary layer height; RH is the value of the relative humidity; TEM is the value of the temperature; SP is the value of the surface pressure; UW and VW are values of the u wind speed and the v wind speed, respectively; VIS is the value of the visibility; $NDVI$ is the value of the NDVI; and DEM is the value of the elevation.

The SPSS software was used to conduct the MLR model. Satellite-retrieved PM2.5 concentrations using the MLR model was validated with PM2.5 concentrations from ground stations. A 10-fold cross validation was conducted to examine if the model was over-fitted. The datasets were divided into 10 folds, and each fold contained 10% of the data. Then one fold was used for validation, and the rest nine folds were used as training datasets. This process repeated for each fold.

The model with the highest accuracy and performance was used to generate PM2.5 distribution maps on annual, seasonal, and monthly scales. In this study, March, April, and May were defined as spring; June, July, and August were defined as summer; September, October, and November were defined as fall; and December, January, and February were defined as winter.

R^2 is an important indicator to describe the fitness of the statistical model, which could be expressed as:

$$R^2 = 1 - \frac{SS_{Regression}}{SS_{Total}} \quad (4\text{-}12)$$

where $SS_{Regression}$ is the sum squared regression error, and SS_{Total} is the sum squared total error.

4.4.2 Geographically Weighted Regression Model

Instead of assuming the coefficients are constant globally, the GWR model takes spatial variations among parameters into account. The daily conventional GWR model could be expressed as:

$$PM2.5_{ij} = C_{0,ij} + C_{AOD,ij}AOD_{ij} + C_{PBLH,ij}PBLH_{ij} + C_{RH,ij}RH_{ij} + C_{TEM,ij}TEM_{ij} + C_{SP,ij}SP_{ij} + C_{UW,ij}UW_{ij}$$
$$+ C_{VW,ij}VW_{ij} + C_{VIS,ij}VIS_{ij} + C_{NDVI,ij}NDVI_{ij} + C_{DEM,ij}DEM_{ij} \quad (4\text{-}13)$$

where $PM2.5_{ij}$ is the ground-level PM2.5 concentrations at location i on day j; $C_{0,ij}$ is the intercept of the equation at location i on day j; $C_{AOD,ij}$, C_{PBLHij}, C_{RHij}, $C_{TEM,ij}$ $C_{SP,ij}$, $C_{UW,ij}$, $C_{VW,ij}$, $C_{VIS,ij}$, $C_{NDVI,ij}$, and $C_{DEM,ij}$ are the coefficients of their corresponding independent variables at location i on day j; AOD_{ij} is the MODIS AOD value at location i on day j; $PBLH_{ij}$ is the value of the planetary boundary layer height at location i on day j; RH_{ij} is the value of the relative humidity at location i on day j; TEM_{ij} is the value of the temperature at location i on day j; SP_{ij} is the value of the surface pressure at location i on day j; UW_{ij} and VW_{ij} are values of the u wind speed and the v wind speed at location i on day j, respectively; VIS_{ij} is the value of the visibility at location i on day j; $NDVI_{ij}$ is the value of the NDVI at location i on day j; and DEM_{ij} is the value of the elevation at location i on day j.

The GWR4 is a Microsoft Windows-based application software, which was designed by Japanese Professor Tomoki Nakayafor for conducting and calibrating GWR models (Li, 2016). The Gaussian model type was selected for this study. The other two types Poisson and Logistic are based on count and binary rather than numerical responses. The adaptive kernel was adopted due to the uneven distribution of ground stations. The golden section search method was chosen to search for the optimal bandwidth size automatically, since bandwidth size selection is considered to be the most significant step of the GWR model. AIC was used for bandwidth selection. AICc was adopted in this study, which is the small sample bias corrected AIC. AIC could provide information for the quality of the model, as well as its performance relative to other models. In general, a lower value of AIC represents a better model quality. Therefore, a global regression model was also conducted using the same input data to compare its performance with the GWR model.

The spatial autocorrelation analysis was conducted in ArcGIS using the residuals of the GWR model. Moran's I was used to describe the spatial autocorrelation. The values of Moran's I ranging from -1 to 1. A positive value represents the existence of a positive spatial autocorrelation, while a negative value represents the existence of a negative spatial autocorrelation. A value of 0 means no spatial autocorrelation exists. The ideal Moran's value for a well-fitted GWR model's residuals should be close to 0 (Li, 2016).

After building the GWR model, a 10-fold cross validation was also conducted to examine if the GWR model was over-fitted, the process was the same as the MLR model.

4.4.3 Theoretical Model

In this study, a theoretical model proposed by Liu (2018) was used to compare with the other two statistical models (MLR and GWR). The theoretical model was conducted based on AOD, PBLH, relative humidity (RH), and visibility (VIS). According to previous studies, PBLH and RH have strong effects on AOD, which need to be removed during the process of PM2.5 retrievals. The equation for the AOD using corrected PBLH and RH could be expressed as:

$$AOD_f^* = \frac{AOD_f}{PBLH \times f(RH)} \tag{4-14}$$

where AOD_f is the fine-mode AOD, which is calculated by the MODIS AOD and fine mode fraction (FMF); Due to the high uncertainty of MODIS FMF observations and the geographic scope of this study, it is acceptable to assume FMF as a constant (0.44) according to previous study (Sorek-Hamer et al., 2017). $PBLH$ is the value of the planetary boundary layer height and $f(RH)$ is the hygroscopic growth function.

The hygroscopic growth function is used to describe the effects of RH on the extinction coefficient, and could be considered as the function of RH (Che et al., 2007). Based on the aerosol size distribution and optical characteristics, the equation for the theoretical model could be expressed as (Liu, 2018):

$$PM_f = \frac{AOD \times FMF}{PBLH \times f(RH)} \times \frac{4\pi\rho(r_g)^3 exp\ (9/2ln^2\sigma_g)}{3(3.912/VIS)} \tag{4-15}$$

where AOD is the value of the MODIS AOD; FMF is the constant value of the fine mode fraction (0.44); $PBLH$ is the value of the planetary boundary layer height; $f(RH)$ is the hygroscopic growth function based on the research of Che et al. (2007) in North America; ρ is a constant of the particle mass density (1.5 g/cm^3); r_g is the radius of aerosol particles with a constant value of 0.298; σ_g is the constant geometric standard deviation (2 μm); and VIS is the value of the visibility. The PM2.5 concentrations generated by this model were validated with the ground-level PM2.5 concentrations.

4.5 Output Analysis

The model with the best performance was used to build monthly and seasonal models. Statistical results including R^2, RMSE, and MAPE were generated for all models for comparison. Box-plots for seasonal and monthly models were conducted to analyze the performance of each model based on the data distribution

and outliers. PM2.5 estimation maps on annual, seasonal, and monthly scales were also generated to validate and compare with ground-level PM2.5 concentrations. BC's wildfire distribution map in August was used to examine the application feasibility of MODIS AOD products during the wildfire season.

4.6 Chapter Summary

This chapter summarizes the methodology of this study. Firstly, MODIS AOD products were validated with AERONET AOD. Then, data preprocessing including projection, clipping, and resampling were conducted. After that, PM2.5 data was matched with MODIS AOD, meteorological, and supplementary data to extract valid lines of data used for the model construction. The MLR, the GWR, and the theoretical model were then conducted for the comparison. The model with the highest accuracy was used to generate spatial distribution maps of PM2.5. Ground-level PM2.5 maps were also utilized to compare with satellite-derived PM2.5. In addition, BC's wildfire active map in 2017 was used to compare with PM2.5 distribution maps generated by the optimal model visually.

Chapter 5 Results and Discussion

Chapter 5 presents the results and discussions of this study. Section 5.1 displays the results of MODIS AOD validation. Section 5.2 reports the results of the MLR model. Section 5.3 discusses the results of the GWR model. Section 5.4 displays the results of the theoretical model. Section 5.5 compares the results of three models. Section 5.6 shows the PM2.5 distribution maps on annual, seasonal, and monthly scales. Section 5.7 provides a summary of the chapter.

5.1 Results of MODIS AOD Validation

As stated in Section 4.2, after temporal and spatial matching, there were 55 collocations in the Kelowna_UAS site. No collocation was generated in the Saturn-Island site since it is located on a small island in the Pacific Ocean, where has a high probability of cloud cover during most time of the year. As a result, no collocation could be collected for the Saturn_Island site. Thus, no MODIS AOD was matched with AERONET AOD in the Saturn_Island site in this study.

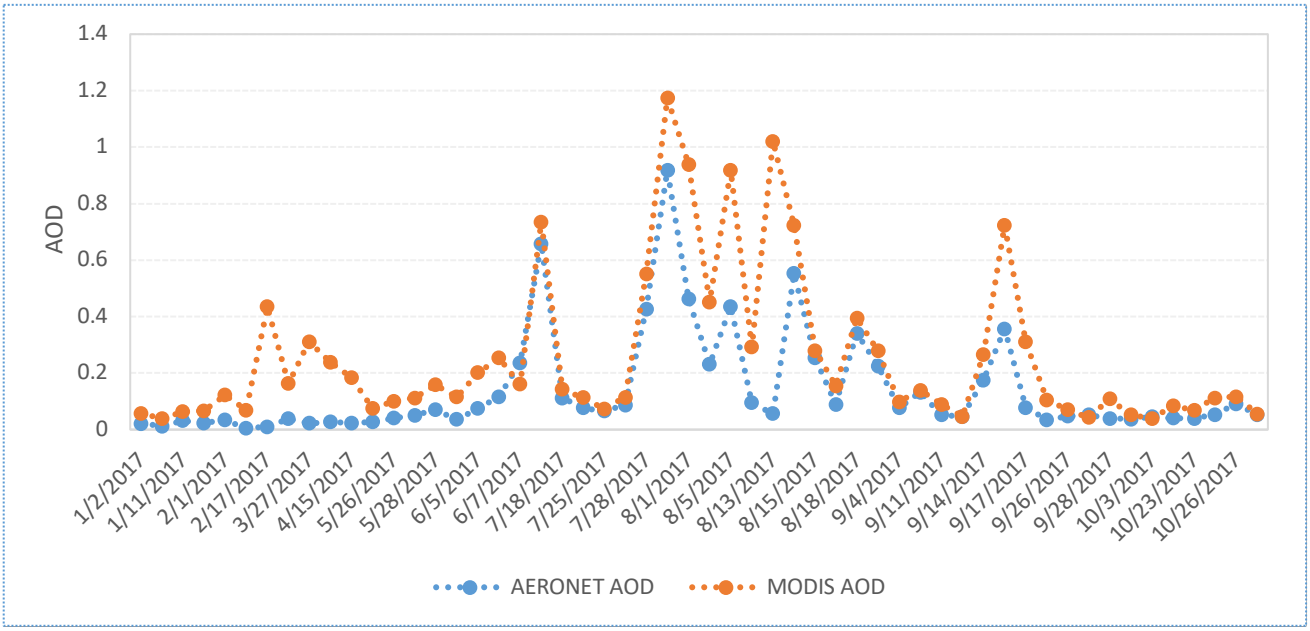

Figure 5.1 Time variations of the MODIS AOD and the AERONET AOD in the Kelowna_UAS site

Figure 5.1 displays 55 collocations in the Kelowna_UAS site through time variations. The AOD values ranging between 0 and 1.4, which is considered to be a reasonable range for both the MODIS AOD and the AERONET AOD (McPhetres & Aggarwal, 2018). Most high AOD values are concentrated in summer, which is the period of severe wildfires. In addition, more fluctuation could be seen during the

summer time. The existence of overestimates is also presented for MODIS AOD products. Furthermore, the number of collocations between the MODIS AOD and the AERONET AOD in winter is smaller than other seasons. There is no collocation in November and December, which might result in biases when assessing the performance of MODIS AOD products.

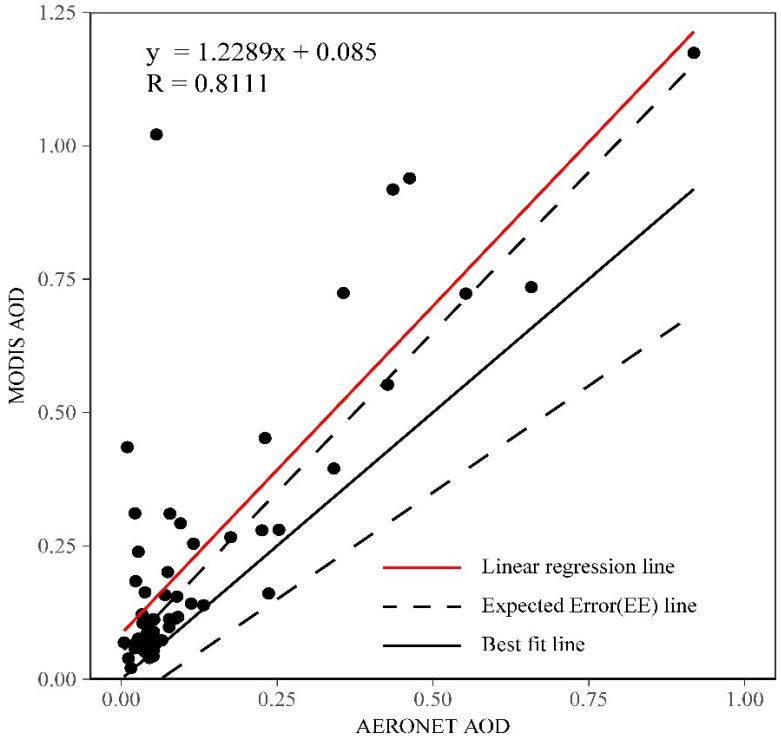

Figure 5.2 Scatter plots of the MODIS AOD against the corresponding AERONET AOD retrievals

Table 5.1 Statistical summaries of the MODIS AOD and the AERONET AOD collocations

Site	N	R	RMSE ($\mu g/m^3$)	MAE ($\mu g/m^3$)	% below EE	% within EE	% above EE
Kelowna_UAS	55	0.81	0.20	0.12	0	58.2	41.8

Figure 5.2 shows the scatter plots of the MODIS AOD against AERONET AOD in the Kelowna_UAS site. The red line represents the linear regression line, the black line denotes the best fit line (y = x), and the two black dash lines represent the expected error (EE) lines for the 3 km MODIS DT products over land with equation EE = ± (0.05 + 0.2$\tau_{AERONET}$). The values of AOD could be divided into

three categories. AOD < 0.5: low aerosol loadings; 0.5 < AOD < 1.0: moderate aerosol loadings; AOD > 1.0: high aerosol loadings (Nichol & Bilal, 2016). From Figure 5.2, it can be seen that most points fall within the range of low aerosol loadings with only a few outliers.

Table 5.1 shows that no collocations lie below the EE line for the Kelowna_UAS site. 58.2% of collocations fall between EE lines, while 41.8% fall above EE lines. This indicates MODIS AOD products tend to overestimate ground-level AOD values. The Pearson correlation coefficient (R) between MODIS and AERONET AOD is 0.81, which suggests a strong correlation between the satellite-derived AOD and the ground-measured AOD. RMSE is used to describe how concentrated the points are around the regression line. The RMSE is 0.20, which represents a close value between the MODIS AOD and the AERONET AOD. MAE represents the mean error between the MODIS AOD and the AERONET AOD. The value of MAE is 0.12, which indicates a relatively small mean error between the MODIS AOD and the AERONET AOD. In summary, the results prove that MODIS AOD products are well correlated with AERONET AOD. Although some biases still exist, the validation results are satisfied overall.

5.2 Results of Multiple Linear Regression Model

Table 5.2 exhibits the statistical results of the MLR model, including mean, coefficient, significance level, and variation inflation factor (VIF). The annual mean ground-level PM2.5 concentration is 14.31 $\mu g/m^3$. The averaged AOD in the 3 km dataset is 0.35. The annual mean of the relative humidity and the planetary boundary layer height are 78.71% and 253.55 m, respectively. The annual mean of the surface pressure is 91519.92 Pa, and the visibility is 19664.27 m in average. In addition, the annual mean of the u wind speed and the v wind speed are 0.24 m/s and -0.27 m/s, respectively. The average temperature is 281.88 K. For the supplementary factors, NDVI and elevation, the annual means are 0.33 and 895.68 m, respectively.

In terms of coefficients, the constant of the MLR model is 88.815. AOD, u wind speed, temperature, NDVI, and elevation have positive coefficients, which means PM2.5 concentrations increase as the values of corresponding variables increase. In contrast, relative humidity, planetary boundary layer height, surface pressure, visibility, and v wind speed have negative coefficients, which means PM2.5 concentrations decrease as the values of corresponding variables increase. This result shows that the explanations between PM2.5 and meteorological factors display the same trend as described in Section 2.3.1.

Table 5.2 Statistical results of the MLR model

Variables	Mean	Coefficient	Significance Level	VIF
PM2.5 ($\mu g/m^3$)	14.31			
Constant		88.815	0.009	1.433
AOD	0.35	25.16	0.000	1.462
Relative Humidity (%)	78.71	-0.204	0.000	1.516
Planetary Boundary Layer height (m)	253.55	-0.0052	0.009	3.524
Surface Pressure (Pa)	91519.92	-0.0016	0.000	1.335
Visibility (m)	19664.27	-0.00036	0.000	1.673
U Wind Speed (m/s)	0.24	0.48	0.218	1.424
V Wind Speed (m/s)	-0.27	-1.65	0.000	1.274
Temperature (K)	281.88	0.31	0.003	1.468
NDVI	0.33	7.18	0.014	2.144
Elevation (m)	895.68	0.0015	0.315	1.433

Note: Mean: the average annual values of each variable, Coefficient: the coefficient of each independent variable, Significance level: p value at 95% confidence level, and VIF: variation inflation factor.

The confidence level for MLR is 95% ($\alpha = 0.05$) in this study. The p value smaller than 0.05 is considered to be statistically significant to the model. From Table 5.2, it can be seen that except the u wind speed and the elevation, the rest variables contribute statistically significantly to the model. The p values of u wind speed and elevation are 0.218 and 0.315 at 95% confidence level, respectively, which are greater than 0.05. Thus, these two variables are not statistically significant to the model in this study.

The variation inflation factor (VIF) is used to measure the multicollinearity among numerous multiple regression variables, or in another word, to assess if the variables are correlated to each other. In general, if VIF is greater than 10, it indicates the existence of a significant multicollinearity between variables. Variables with significant multicollinearity need to be removed, otherwise the accuracy of the model will be seriously affected. The VIF of all variables in this study is smaller than 10, which proves that there is no significant multicollinearity between different variables.

A 10-fold cross validation was conducted to assess whether the MLR was over-fitted or not. Figure 5.3 displays the scatter plots of the satellite-estimated PM2.5 using the MLR and its corresponding 10-fold CV model against the ground measured PM2.5. The R^2 of the MLR model is 0.53, which indicates that the MLR model could explain 53% of the variability. The R^2 of the 10-fold CV MLR is 0.51, which is only 0.02 lower than the MLR model. It indicates that the MLR is not over-fitted. The detailed comparison between the MLR and other two models is discussed in Section 5.5.

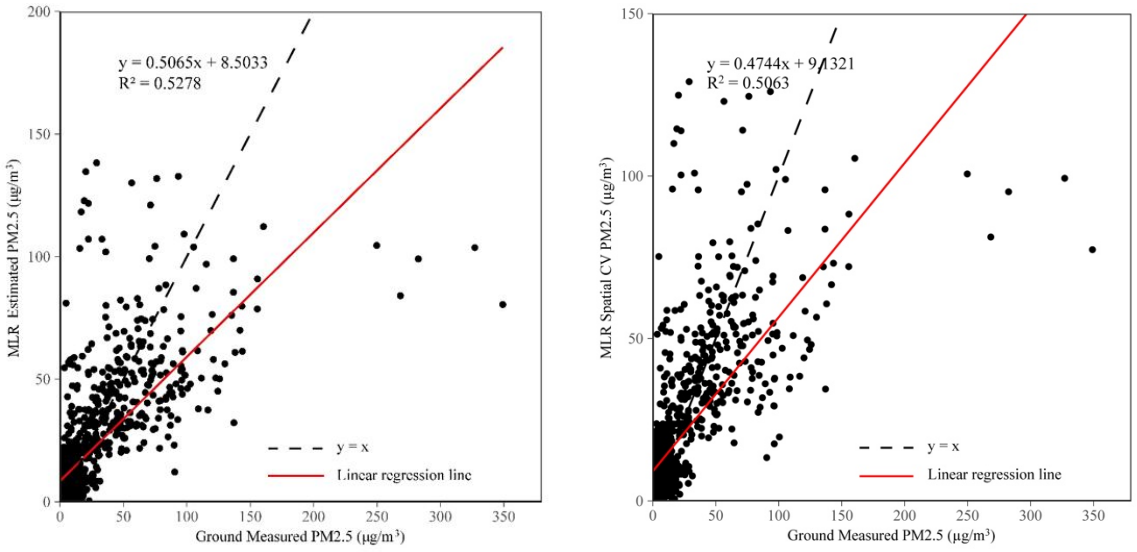

(a) (b)

Figure 5.3 Scatter plots of satellite-estimated PM2.5 using (a) MLR and (b) its corresponding 10-fold CV model against ground measured PM2.5

5.3 Results of Geographically Weighted Regression Model

The statistical results including N, AICc, R^2, RMSE, and Moran's I of the GWR model are presented in Table 5.3. The statistical results of a 10-fold CV for the GWR model using the same datasets are also shown

in the same table. In addition, the results of a global regression model, which is used to compare with the local GWR model, are also displayed in Table 5.3.

Table 5.3 Statistical results of the GWR model, 10-fold CV for the GWR model, and the corresponding global regression model

Model	N	AICc	R^2	RMSE ($\mu g/m^3$)	MAPE (%)	Moran's I
GWR	1914	15612.71	0.76	13.45	16.75	-0.014
10-fold CV for GWR	1914		0.74	14.26	18.94	-0.016
Global Regression Model	1914	16638.17	0.53	29.44	35.45	

The Moran's I values for the residuals of the GWR model and the 10-fold CV for GWR model are -0.014 and -0.016, respectively, which are all close to 0. It indicates the spatial autocorrelation barely exists among the residuals, and the observations are independent with each other. Otherwise, the GWR model might not be suitable for the study, and other spatial models such as the spatial lag model need to be used to replace the GWR model. The spatial lag model assumes the existence of autocorrelation among observations. As a result, the GWR model is suitable for this study for the analysis.

The training samples for the three models are all 1914. Regarding AICc, the values of AICc for the GWR model and the global regression model are 15612.71 and 16638.17, respectively. As described in Section 4.4.2, AICc is used to evaluate the relative quality between different models. According to You et al. (2016), if the difference of AICc between two models is larger than 3, then the model with smaller AICc has better performance and quality. Therefore, since the GWR model's AICc is much lower than the global regression model, the GWR model generates better performance result than the global regression model.

R^2 is called the coefficient of determination, which is an important indicator for the fitness of models. It reflects how close the data are to the fitted regression line. If the R^2 equals to 1, which means the predicted values are equal to the observed values. The R^2 of the GWR model is 0.76, which means the model is able to explain 76% variation of response data. In contrast, the global regression model only has an R^2 of 0.53, which is much lower than the GWR model. The 10-fold cross validation was conducted to assess whether the model is over-fitted or not. Normally, the overfitting means a model only fits a limited

set of data, while it is not suitable for other datasets. Figure 5.4 displays the scatter plots of the GWR and its corresponding 10-fold CV model. It can be seen that the 10-fold CV for GWR has R^2 of 0.74, which is only 0.02 lower than the GWR model. It implies that the model is not over-fitted.

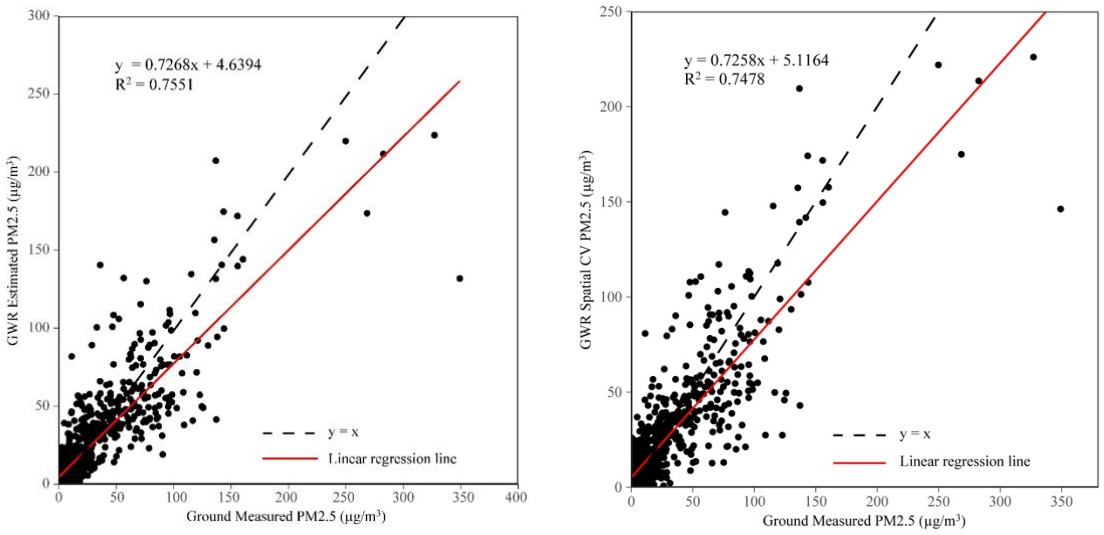

(a) (b)

Figure 5.4 Scatter plots of the satellite-estimated PM2.5 using (a) GWR and (b) its corresponding 10-fold CV model against ground measured PM2.5

In terms of RMSE and mean absolute percentage error (MAPE), they are both used to indicate the accuracy of predicted values. The GWR model has the lowest values for both RMSE and MAPE, which are 13.45 μg/m^3 and 16.75%, respectively. The results all show that the GWR model is not overfitted.

5.4 Results of the Theoretical Model

After using the equation in Section 4.4.3, PM2.5 concentrations were generated using the theoretical model. Unlike statistical models, there is no 'overfitting' issue exists in the theoretical model, since no training samples are required for the theoretical model to calculate the coefficients. Therefore, the validation of the theoretical model was conducted by comparing with ground-level PM2.5 concentrations.

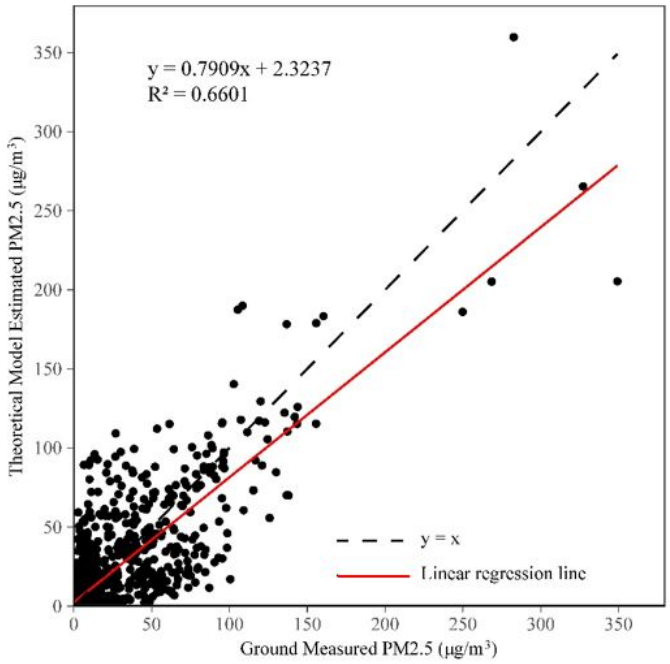

Figure 5.5 Scatter plots of the theoretical model estimated PM2.5 against ground-measured PM2.5

From Figure 5.6, it can be seen that the R^2 of the theoretical model is 0.66, which indicates that the model could explain 66% of the response data. The best fit line y = x and the linear regression line are also presented in Figure 5.6. The points are scattered along with the linear regression linear, which might result in large errors between predicted and observed values. The detailed comparison between the theoretical model and the other two models is discussed in the next section.

5.5 Comparison of Three Models

After conducting and validating three models, the statistical results of the three models are presented in Table 5.4. The training samples for all models are 1914 in order to make a better comparison among the three models. In terms of R^2, the GWR model denotes the highest value of 0.76, while the MLR model has the lowest R^2 of 0.53. It indicates that the GWR model could explain the most variability of the response data around its mean. The theoretical model has an R^2 value of 0.66, which is lower than the GWR model but higher than the MLR model.

Table 5.4 Statistical results of MLR, 10-fold CV MLR, GWR, 10-fold CV GWR, and theoretical models

Model	N	R^2	RMSE ($\mu g/m^3$)	MAPE (%)
MLR	1914	0.53	29.44	35.45
10-fold CV for MLR	1914	0.51	33.53	39.64
GWR	1914	0.76	13.45	16.75
10-fold CV for GWR	1914	0.74	14.26	18.94
Theoretical	1914	0.66	19.74	25.48

The GWR and its corresponding 10-fold CV model show the lowest RMSE values, with 13.45 $\mu g/m^3$ and 14.26$\mu g/m^3$, respectively. It indicates that the average magnitudes of the predicted errors for the two models are 13.45 $\mu g/m^3$ and 14.26 $\mu g/m^3$, respectively. From Table 5.4, it can be seen that the model with the highest coefficient of determination values has the lowest value of RMSE. The ranking of RMSE values are related to their R^2 and shows the same patterns.

MAPE is used to describe the percentage of the overestimation or the underestimation part among the predicted values. The predicted PM2.5 concentrations using the GWR and its corresponding 10-fold model have MAPE values of 16.75% and 18.94%, respectively. The MLR-predicted PM2.5 values generate the highest MAPE value of 35.45%, which indicates the percentage of PM2.5 predicted errors account for the highest part among the three models.

In conclusion, the GWR model generates the best predicted results of PM2.5 concentrations compared to the MLR and the theoretical model. The theoretical model displays the moderate performance, which is better than the MLR model, but worse than the GWR model. Therefore, the GWR was chosen to generate PM2.5 distribution maps on annual, seasonal, and monthly scales.

5.6 PM2.5 Distribution Maps

After comparing the three models, annual, seasonal, and monthly PM2.5 distribution maps were generated using the GWR model.

5.6.1 Annual Model

The observations from ground stations show a strong heterogeneity of PM2.5 concentrations based on discrete ground stations, while the spatial distribution map generated by the satellite-derived AOD exhibits continuous surfaces regarding PM2.5 concentrations.

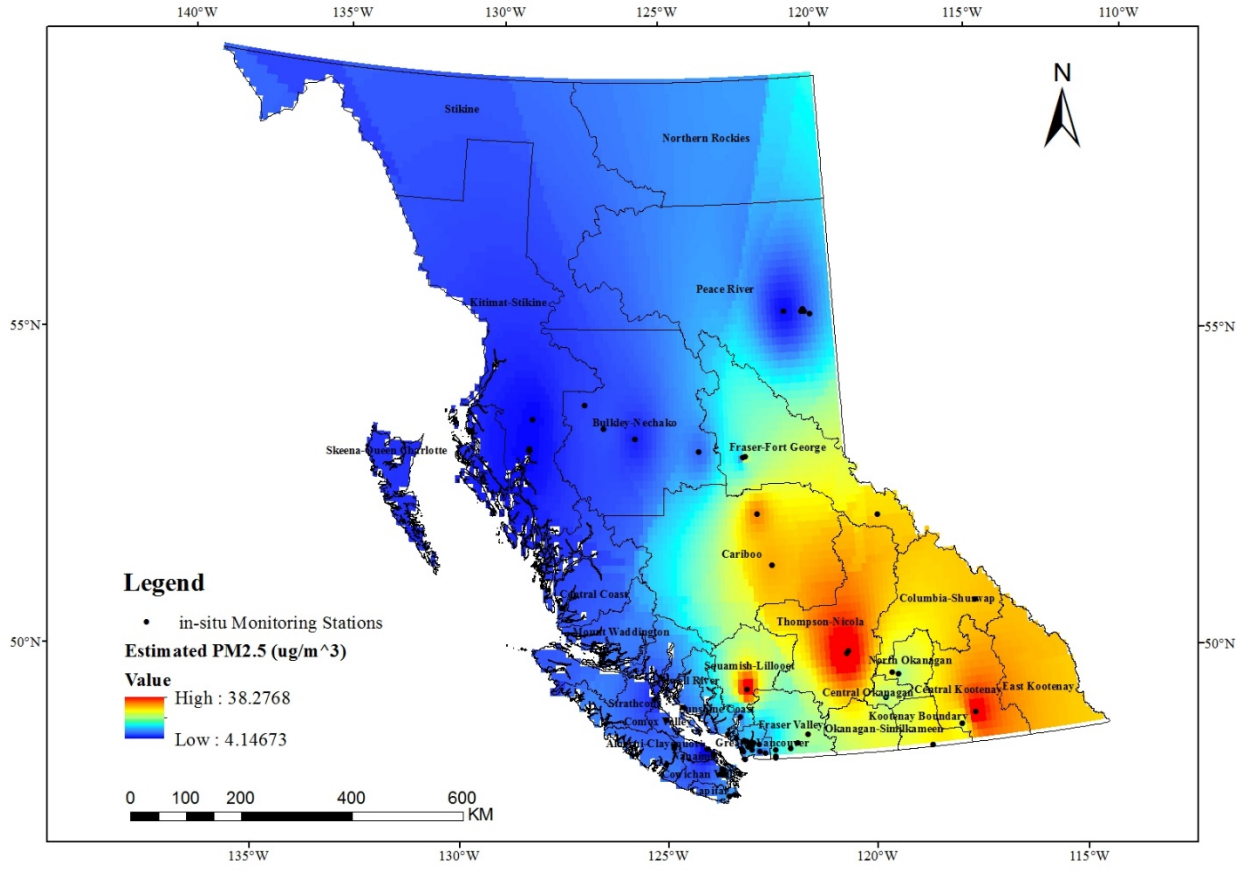

Figure 5.6 Estimated PM2.5 distribution map generated by the GWR model in 2017

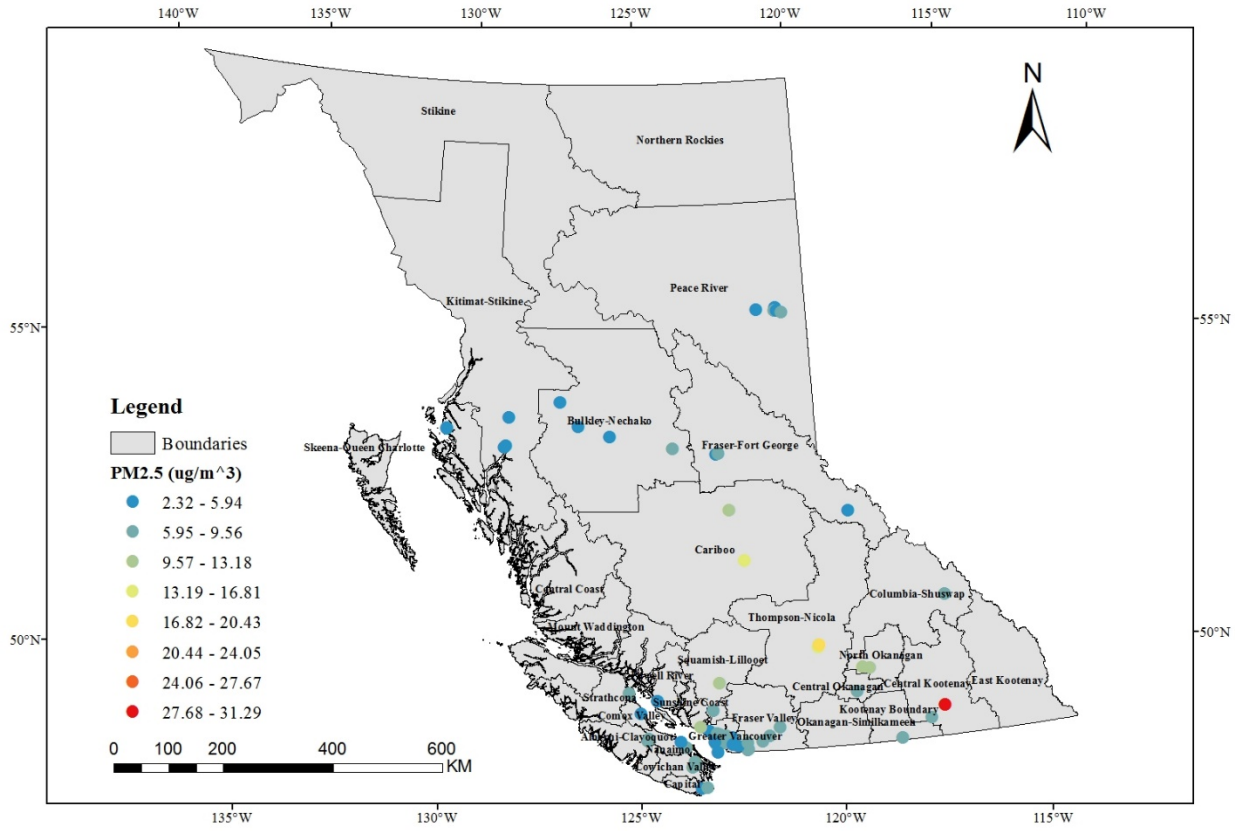

Figure 5.7 Annual mean ground station measured PM2.5 concentrations

The annual PM2.5 concentrations generated by the GWR model are presented in Figure 5.6. The annual ground station measured PM2.5 distribution map is also generated to compare with the annual distribution map generated by the GWR model. The highest predicted PM2.5 value of the GWR model is 38.28 μg/m^3, while for the annual ground station distribution map, the highest value is 31.29 μg/m^3. By looking at Figures 5.6 and 5.7, the GWR model presents the similar spatial distribution of PM2.5 concentrations as ground stations. The regions with the highest PM2.5 values are concentrated in the Central Kootenay. The ground station in the Central Kootenay has the highest annual mean PM2.5 concentrations. The GWR model tends to overestimate PM2.5 concentrations in some regions, such as Thompson-Nicola and Cariboo regional districts in a reasonable range. Both districts have higher PM2.5 concentrations than the surrounding area. For the rest area of BC, the annual PM2.5 concentrations are under both CAAQS and BC's annual standards. In addition, the GWR model is able to provide more variations than ground stations. This comparison also indicates that the GWR model shows a high accuracy in predicting PM2.5 concentrations, which could be used for further analysis.

5.6.2 Seasonal Model

After generating the annual model, seasonal models were also conducted to examine PM2.5 concentrations in four seasons. Due to the lack of training samples in winter (i.e., only 19 samples), the GWR model in winter was failed to construct. The statistics of the other three seasonal models are presented in Table 5.5.

Table 5.5 Statistical results of seasonal GWR models

	N	R^2	RMSE ($\mu g/m^3$)	MAPE (%)	Moran's I
Spring	240	0.43	37.46	57.54	0.018
Summer	1185	0.79	8.17	18.23	-0.022
Fall	469	0.56	25.87	35.54	-0.052
Winter	Failed to construct due to lack of training samples				

The summer model has the most training samples (1185), fall and spring models have 469 and 240 training samples, respectively. As indicated before, winter model was failed to conduct due to the lack of training samples. In terms of R^2, it can be seen that the spring model has the lowest R^2 value of 0.43, while the summer model displays the highest R^2 value of 0.79. The reason for this might due to the difference in the number of training samples. Normally a model with more training samples as input will generate better results. The summer model has a lower RMSE value than the spring and winter model, which means the average magnitude error for the predicted values is lower than other two models. The spring model reveals the highest values of RMSE and MAPE, which proves it to be the worst model among three seasonal models. In terms of Moran's I, it can be seen that the values for three models are all close to 0, which indicates no spatial autocorrelation exists among the residuals.

Figure 5.8 displays the box plots of local R^2 derived from seasonal GWR models. Although the spring model has a relatively clustered range, it still generates worse results than other two seasonal models due to the low values of local R^2 (0.36-0.48). This suggests that the GWR model might not be suitable for estimating PM2.5 concentrations in spring. It also indicates that GWR-predicted PM2.5 concentrations might exist bias. The local R^2 for the summer model ranges from 0.56 to 0.88, which demonstrates the best performance of the three models. There are outliers in both spring and summer models, while no outlier exists in the fall model. It could be carefully concluded that both spring and summer models have a higher probability to overestimate the PM2.5 concentrations than the fall model.

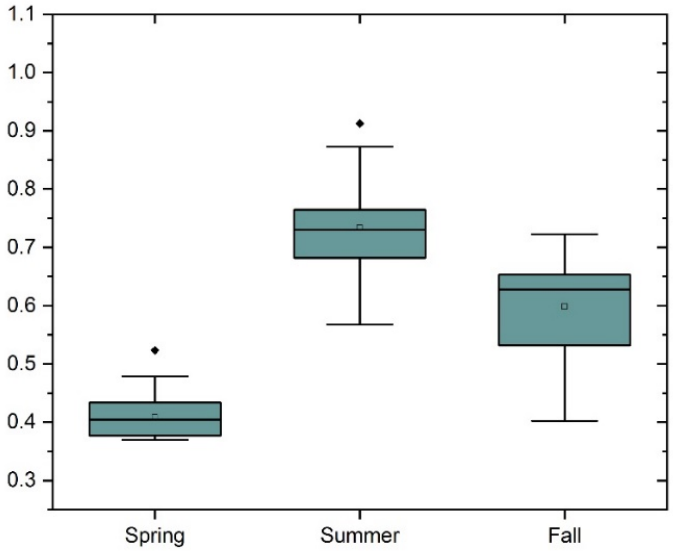

Figure 5.8 Box-plots of local R^2 derived from seasonal GWR models

Figures 5.9, 5.10, and 5.11 show the spatial distribution maps in spring, summer, and fall, as well as their corresponding averaged PM2.5 concentrations from ground stations. For the spring distribution map, it can be seen that the highest PM2.5 concentration is 7.67 μg/m^3 centered in the southwest part of BC. By comparing to ground monitoring stations, PM2.5 concentrations are underestimated in the Thompson-Nicola region, and are overestimated in the Vancouver Island, which indicating significant differences between the predicted and observed values using the spring GWR model, since the R^2 is only 0.43. The summer model has the best performance. The highest PM2.5 concentrations in summer generated by the GWR and ground stations are 53.95 μg/m^3 and 46.94 μg/m^3, respectively. Regions with high PM2.5 concentrations are greater than that in spring and fall, especially centered on the area with wildfires. Since summer is the season with highest occurrence possibility of wildfires, which implies that wildfires could release much more PM2.5 than spring and fall, and could be considered as the main source of rapid rising PM2.5 concentrations in summer. According to the spatial distribution map of PM2.5 in summer, it can be concluded that the GWR is able to predict PM2.5 concentrations, because the trends of PM2.5 distributions are almost the same in two maps. For the PM2.5 distribution maps in fall, it can be seen that the highest PM2.5 concentrations are 23.01 μg/m^3 and 31.13 μg/m^3, respectively, which means the fall GWR model underestimates PM2.5 concentrations in some instances. As defined before, September belongs to fall, which is still under BC's state of emergency period during the wildfire season in 2017. Therefore, PM2.5 concentrations in fall are higher than that in spring, but lower than that in summer. Some underestimations exist in the fall spatial distribution map compared to the ground station monitored PM2.5 concentrations.

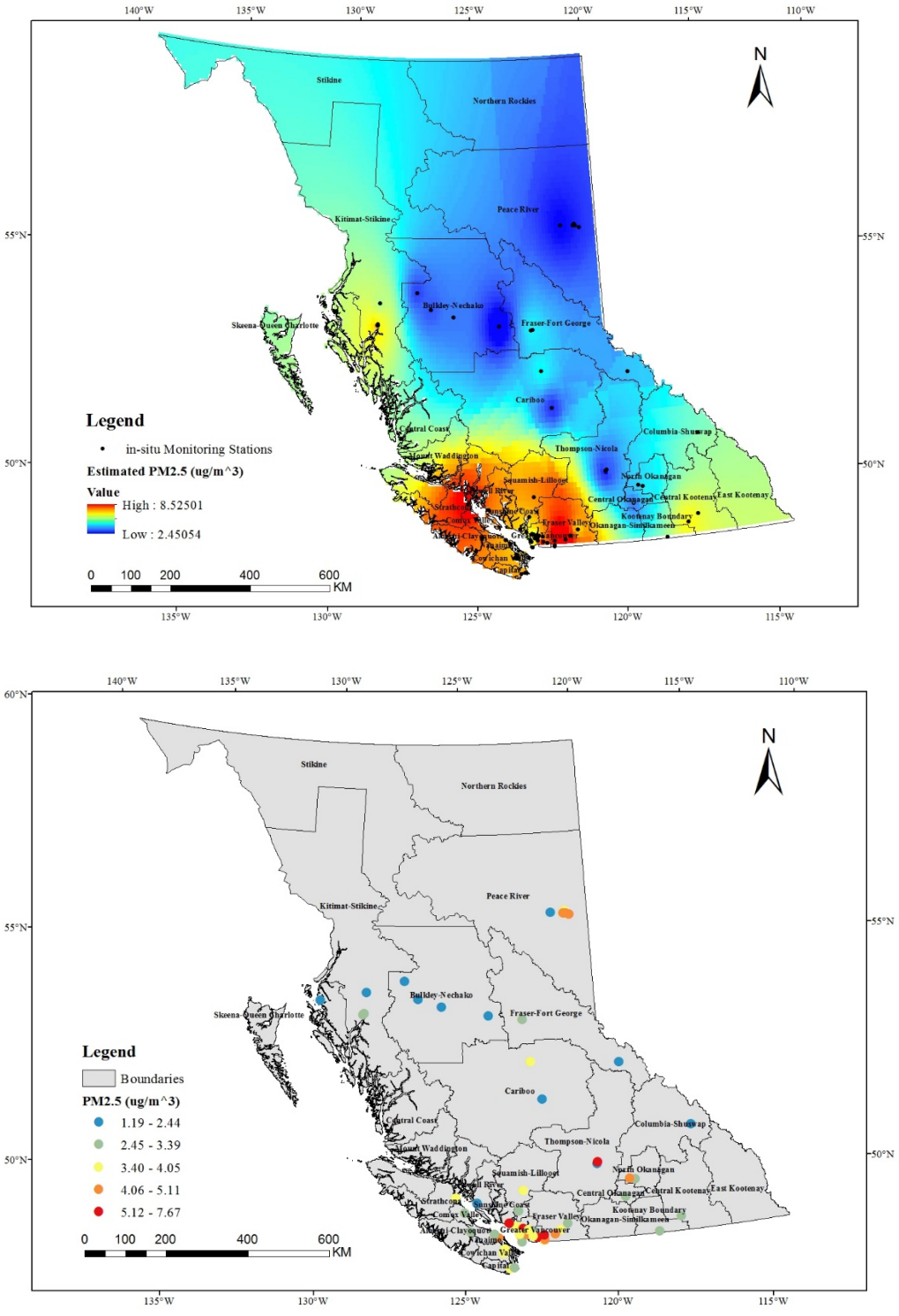

Figure 5.9 Estimated PM2.5 generated by the seasonal GWR model in spring (top), and averaged PM2.5 concentrations from ground monitoring stations in spring (bottom)

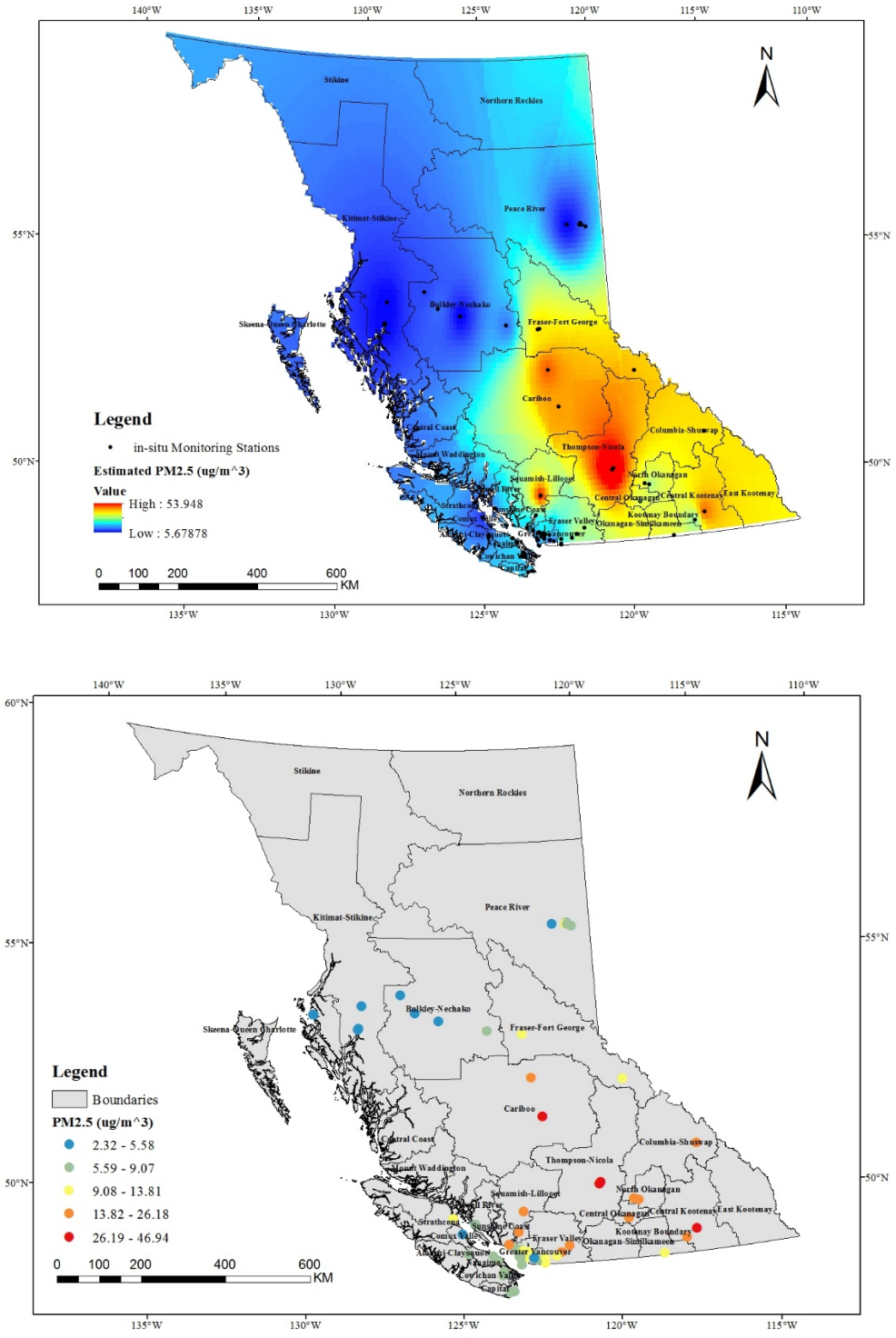

Figure 5.10 Estimated PM2.5 generated by the seasonal GWR model in summer (top), and averaged PM2.5 concentrations from ground monitoring stations in summer (bottom)

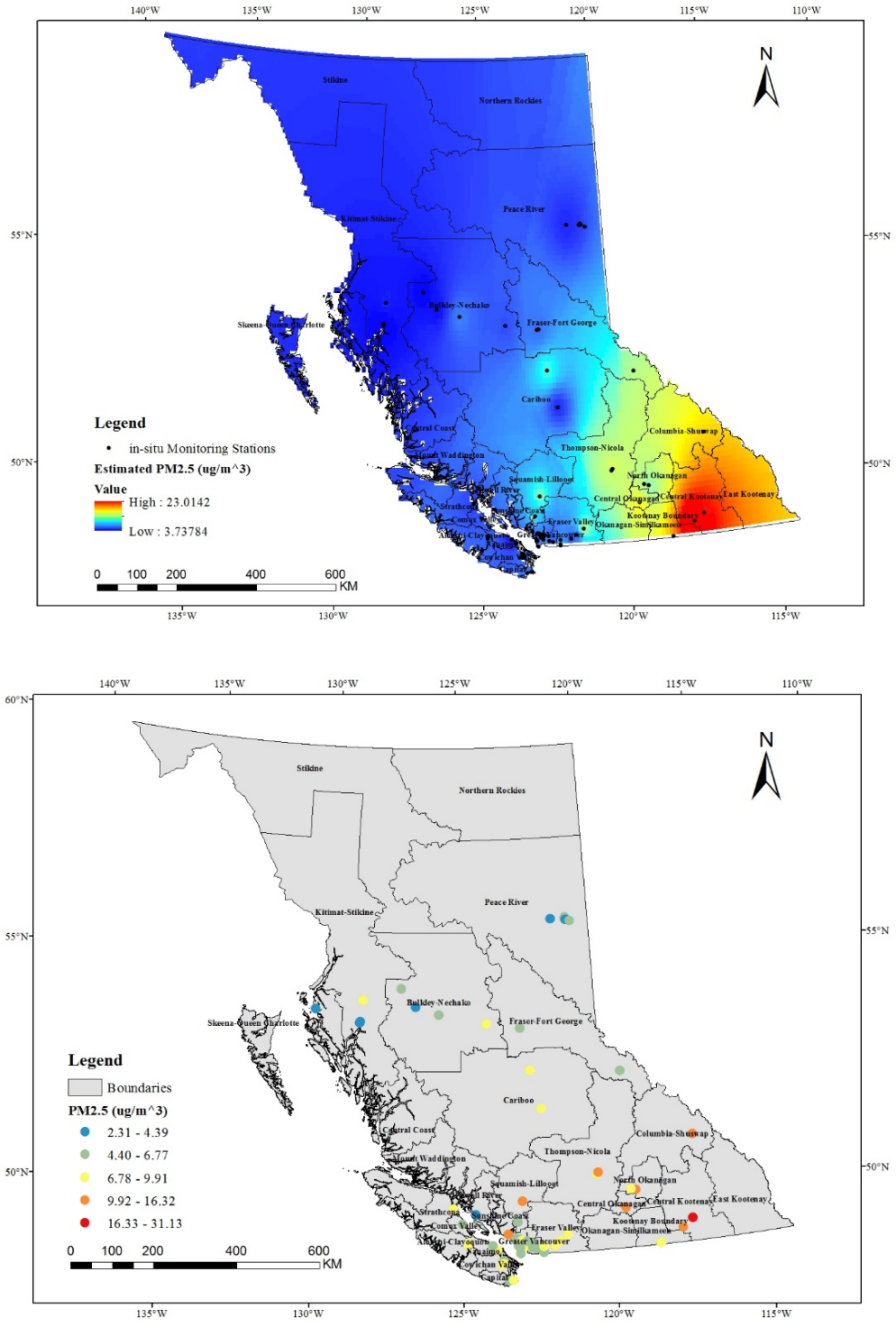

Figure 5.11 Estimated PM2.5 generated by the seasonal GWR model in fall (top), and averaged PM2.5 concentrations from ground monitoring stations in fall (bottom)

5.6.3 Monthly Model

After seasonal models were conducted, monthly models were built during the BC's state of emergency wildfire season between July and September to estimate PM2.5 concentrations. Table 5.6 summarizes the statistical results of monthly GWR models.

Table 5.6 Statistical results of monthly GWR models

	N	R^2	RMSE ($\mu g/m^3$)	MAPE (%)	Moran's I
July	421	0.85	3.26	5.35	-0.032
August	540	0.81	7.69	11.31	-0.046
September	271	0.75	8.45	12.68	-0.11

The training samples for three monthly models are 421, 540, and 271, respectively. All three models perform high values of R^2, and the July model has the highest R^2 with 0.85, which demonstrates that the GWR is suitable for conducting monthly models in July, August, and September. The RMSE for three models are 3.26 $\mu g/m^3$, 11.31 $\mu g/m^3$, and 12.68 $\mu g/m^3$, respectively. The July model has the lowest RMSE value, as well as the MAPE value (5.35%), which indicates that the July model has the best performance compared to other two monthly models. The average magnitude error for predicted values in July is 3.26 $\mu g/m^3$, which is the lowest among annual, seasonal, and monthly GWR models. The trends of RMSE and MAPE regarding R^2 are the same for all three models, which is: RMSE and MAPE increase as R^2 increases. In addition, Moran's I was also conducted for the residuals of three models to examine the spatial autocorrelation. From Table 5.6, it can be seen that Moran's I values for the residuals of three models are all near 0, which indicates there is no significant spatial autocorrelation exists.

The same as seasonal models, a box plot of local R^2 for monthly models is presented in Figure 5.12. It can be seen that the medians of the three models are almost the same. No outlier exists in the three models. In addition, the July model has the most clustered distribution, which suggests that it has the best performance. Although the September model has the highest local R^2, the variability of its distribution regarding local R^2 is large (0.42-0.97). The "whiskers" for the July model is the shortest, while for the September model is the longest. It can be interpreted that the local R^2 values vary more widely for the September model, while the local R^2 values are centered on the mean values for the July model.

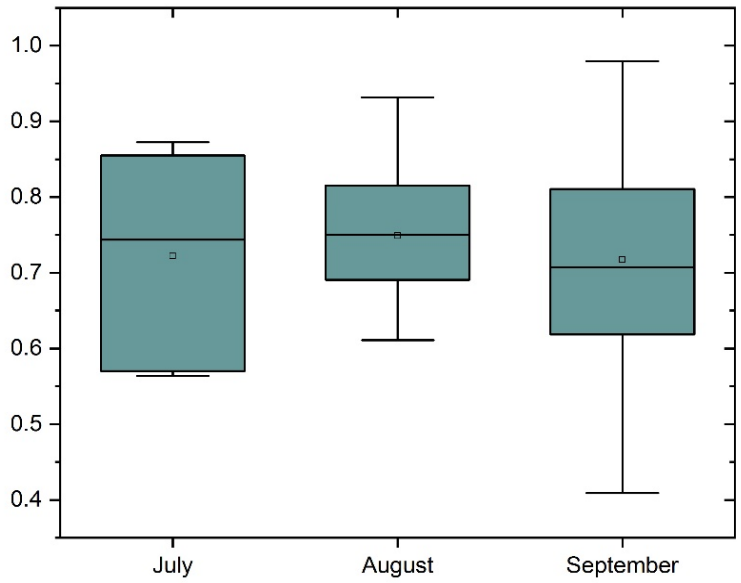

Figure 5.12 Box-plots of local R^2 derived from monthly GWR models

Figures 5.13, 5.14, and 5.15 show the spatial distribution maps generated by the monthly GWR models, as well as their corresponding distribution maps generated by ground monitoring stations. In July, the estimated PM2.5 values range between 1.43 and 35.28 $\mu g/m^3$. The regions with high PM2.5 concentrations are centered on the Cariboo district. The ground-level PM2.5 concentrations agree with the estimated PM2.5 concentrations. It can be seen that August has the most severe PM2.5 concentrations, with the highest value over 100 $\mu g/m^3$ based on the ground station measurements. For estimated PM2.5 concentrations generated by the August GWR model, PM2.5 reaches its highest point at 83.37 $\mu g/m^3$. In order to examine the accuracy of prediction values, an active wildfire map of BC in August, 2017 is also presented in Figure 5.14. It can be observed that most regions with active wildfire exhibit the highest values of PM2.5 concentrations. However, for the area that is lack of ground monitoring stations, the PM2.5 concentrations are underestimated due to the insufficient number of control points. Therefore, more ground stations are helpful for increasing the accuracy of estimation. It could also be concluded that there is a strong correlation between wildfires and PM2.5 concentrations. Regarding PM2.5 concentrations in September, some underestimations are revealed. The main reason for this is due to the lowest value of R^2 for the September model. Therefore, by comparing three monthly models, it can be viewed that there is an obvious rising trend in PM2.5 concentrations during the wildfire season, especially in August.

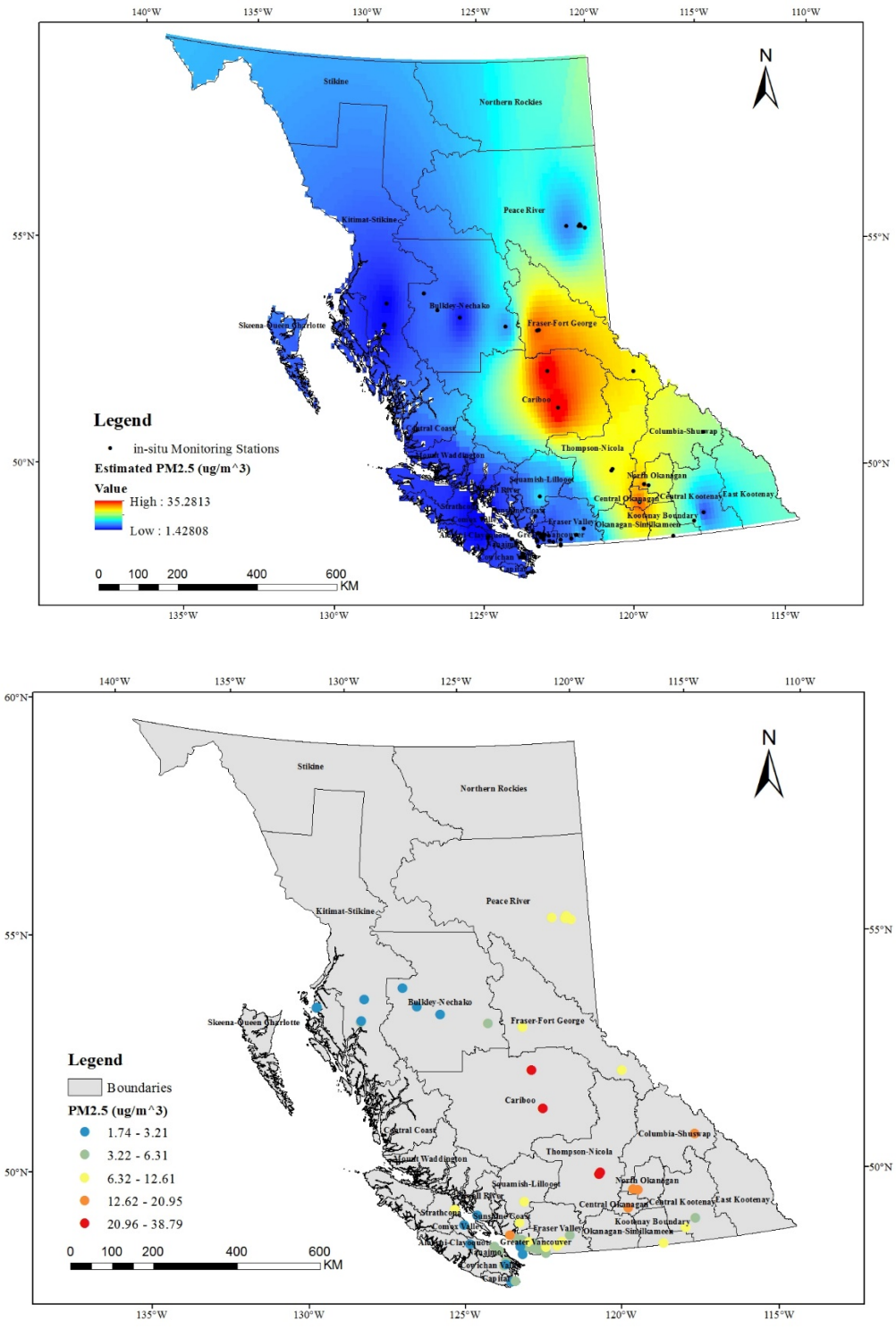

Figure 5.13 Estimated PM2.5 generated by the seasonal GWR model in July (top), and averaged PM2.5 concentrations from ground monitoring stations in July (bottom)

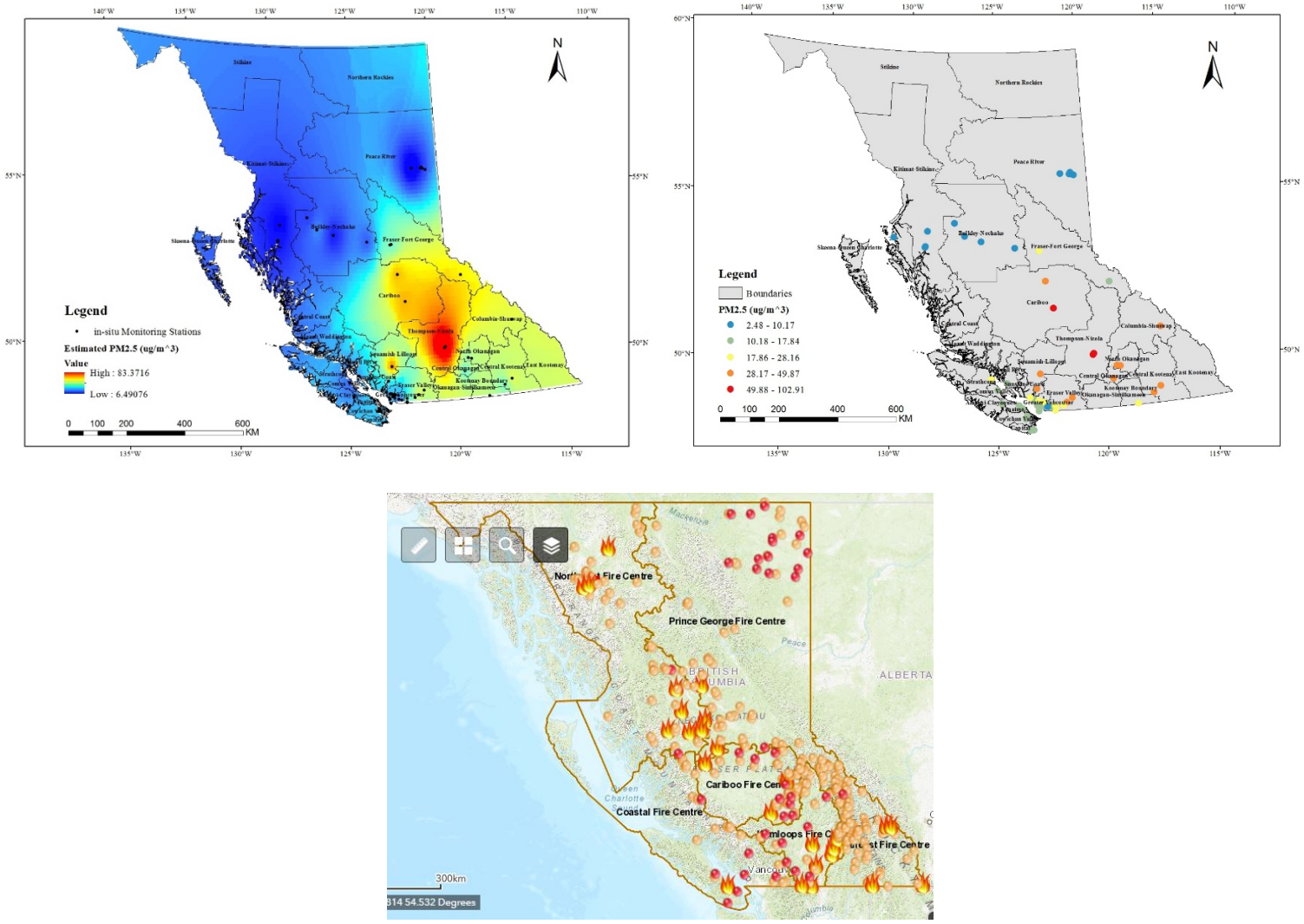

Figure 5.14 Estimated PM2.5 generated by the seasonal GWR model in August (top left), averaged PM2.5 concentrations from ground monitoring stations in August (top right), and BC's active wildfire distribution map (bottom) in August 2017

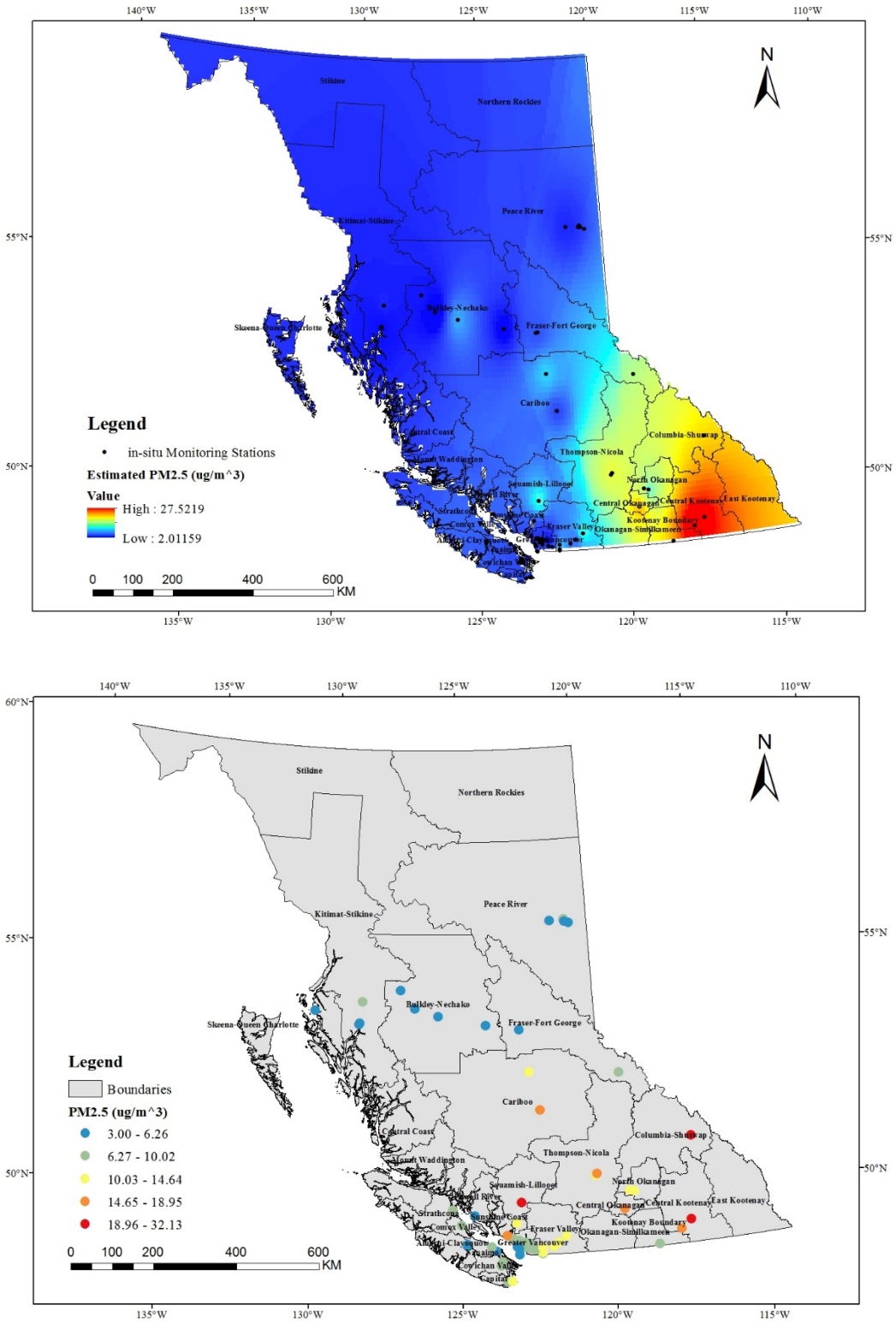

Figure 5.15 Estimated PM2.5 generated by the seasonal GWR model in September (top), and averaged PM2.5 concentrations from ground monitoring stations in September (bottom)

5.7 Chapter Summary

This chapter summarizes major results of the study. Firstly, MODIS AOD was validated with AERONET AOD, and the result showed that there was a strong correlation between the MODIS AOD and the AERONET AOD with R value of 0.81. The 3 km MODIS AOD products tended to overestimate AOD values since 41.8% of total points fell above the EE line. Secondly, the comparison results of the MLR, GWR and theoretical model were presented and discussed. The GWR model exhibited the highest R^2 value of 0.75, while for the MLR and theoretical model, the R^2 values were 0.53 and 0.66, respectively. Therefore, the GWR was selected to generate PM2.5 spatial distribution maps at annual, seasonal, and monthly maps due to its best performance in response to variability explanations. Thirdly, annual, seasonal, and monthly PM2.5 spatial distribution maps were generated using the GWR model. The spring model displayed the lowest R^2, while the July model had the highest R^2. The results showed that the accuracy of PM2.5 concentrations generated by the GWR model was high, although some underestimations and overestimations were revealed. The results also demonstrated that there was an obvious rising trend in PM2.5 during BC's wildfire season.

Chapter 6 Conclusions and Recommendations

Chapter 6 presents key findings and limitations of the study, as well as the recommendations for future studies.

6.1 Key Findings of the Study

The main purpose of this study is to estimate PM2.5 in BC using 3 km MODIS AOD products integrating meteorological and supplementary data. Some key findings regarding the specific objectives are summarized.

6.1.1 Objective 1: MODIS AOD Validation with AERONET AOD

The 3km MODIS AOD products were validated with the AERONET AOD, and a strong correlation was observed between the MODIS AOD and the AERONET AOD. Based on the results, it was also found that the 3 km MODIS AOD products tended to overestimate ground-level AOD values, but most values fell within a reasonable range regarding AERONET AOD. It indicated that the 3 km MODIS AOD products were qualified to use for PM2.5 estimations. For regions that are lack of AEORNET sites, MODIS AOD products could be considered as a substitute for further studies.

6.1.2 Objective 2: Comparison of the MLR, GWR, and Theoretical Models

The MLR, GWR, and theoretical models were conducted for evaluation. The MLR exhibited the worst prediction performance, while the GWR generated the best performance. 10-fold cross validations were conducted for two statistical models, and both models were not over-fitted. The GWR model put spatial variation into account, which improved its accuracy regarding PM2.5 predictions. The theoretical model took aerosol characteristics into consideration, and achieved a moderate performance, which was better than the MLR model. Although the application of the theoretical is relatively limited compared to statistical models, it can be used as a reference model to validate results with traditional models.

6.1.3 Objective 3: Spatial Distribution Analysis of PM2.5

PM2.5 spatial distribution maps were generated using the GWR model. After comparing with ground station PM2.5 concentrations, it can be concluded that PM2.5 concentrations predicted by the GWR model nearly followed the same trend as PM2.5 concentrations measured by ground stations. The summer model generated the best performance among the three seasonal models. The winter model was failed to conduct due to the lack of training samples. Three monthly models all performed high values of R^2. Except for the

spring and fall models, the rest GWR models were able to generate accurate PM2.5 distribution maps that followed the same trend as the PM2.5 concentrations measured by ground stations.

6.1.4 Objective 4: Application Feasibility of MODIS AOD Products and the GWR Model

After examining PM2.5 concentrations during the wildfire season, it was found that there was a rapid increasing trend in PM2.5 concentrations. According to the spatial distribution map generated by the August model, PM2.5 concentrations were the highest in August, especially in regions with active wildfires. It can be concluded that the integration of MODIS AOD products and the GWR model was capable of estimating PM2.5 concentrations accurately during BC's wildfire season, which indicated a high application feasibility for the future studies in other regions. This study is also valuable for the Government of BC to conduct research related to air pollution and public health perspectives.

6.2 Limitations of the Study

Although this study achieved its main objectives and made some contributions to its relevant field, some limitations and uncertainties still exist. Since most similar studies were conducted in developing countries with severe air pollution, there are not enough research could be used as references in developed countries with high air quality such as Canada.

Firstly, this study only adopted Aqua MODIS AOD datasets, while Terra MODIS AOD datasets are not used. For retrieval days without AOD data, Terra MODIS might be used to reduce the number of non-retrieval days of AOD and improve estimation accuracy and spatial coverage. In addition, in order to match Aqua's overpassing time at 13:30, meteorological data were retrieved at the same time. The estimated PM2.5 concentrations in this study were based on 13:30, while PM2.5 concentrations at other times are not evaluated.

Secondly, due to the lack of collocations between MODIS AOD and the AOD from the Saturn_Island AERONET site, there might exist some bias regarding AOD validation and PM2.5 estimation. Also, as stated in the previous paragraph, the lack of AOD retrieval data would be another reason for inaccurate AOD validation and PM2.5 estimation. The unevenly distribution of PM2.5 ground stations would also affect PM2.5 estimation in this study.

Thirdly, the GWR model was failed to conduct in winter due to the lack of training samples. The theoretical model was built based on several assumptions. It assumes the distribution of aerosols is even in the atmospheric vertical direction, and the shape of aerosol particles is all spherical.

Lastly, the meteorological and supplementary data used in this study were just for model constructions. The impact of each parameter on PM2.5 estimation is not discussed. The dispersion and accumulation of PM2.5 concentrations are not presented. In addition, the meteorological and supplementary factors adopted in this study were based on previous studies conducted in developing countries. Additional factors are not considered.

6.3 Recommendations for Future Studies

Based on limitations that mentioned before, several recommendations are made:

Firstly, AOD products from other sensors such as Terra, MISR, and SeaWIFS could be combined to increase the number of available AOD retrieval days for more accurate predictions.

Secondly, spatial regression models could be conducted to analyze the spatial relationships between AOD and PM2.5 concentrations. By combining with AOD products from other sensors, it is able to increase AOD matchings for the AOD validation. Furthermore, more ground stations need to be built in rural area and to follow a more even distribution pattern, in order to increase the accuracy of PM2.5 estimation using remote sensing techniques.

Thirdly, the vertical structure of aerosols could be taken into considerations using different remote sensing techniques, such as LiDAR. Also, the improvement of algorithms could also contribute to a higher accuracy of the theoretical model.

Lastly, more factors could be added into the model to increase the accuracy of the model's performance. The accumulation and dispersion trends of PM2.5 could be identified on a relatively large scale, such as a national or global scale.

References

AirNow. (2018). *International air quality*. https://www.airnow.gov/index.cfm?action=airnow.international. Last accessed on April 12, 2019.

Alhaj Mohamad, F. (2015). *Retrieval of aerosol optical depth from MODIS data at 500m resolution compared with ground measurement in the states of Indiana* (Doctoral dissertation, Indianan University). https://scholarworks.iupui.edu/bitstream/handle/1805/7936/Thesis.pdf;sequence=1. Last accessed on April 12, 2019.

Ångström, A. (1964). The parameters of atmospheric turbidity. *Tellus*, *16*(1), 64-75.

Augustine, J. A., DeLuisi, J. J. & Long, C. N. (2000). SURFRAD–A national surface radiation budget network for atmospheric research. *Bulletin of the American Meteorological Society*, *81*(10), 2341-2358.

Ayers, G. P., Keywood, M. D. & Gras, J. L. (1999). TEOM vs. manual gravimetric methods for determination of PM2.5 aerosol mass concentrations. *Atmospheric Environment*, *33*(22), 3717-3721.

Bell, T. & Adams, M. (2008). Smoke from wildfires and prescribed burning in Australia: effects on human health and ecosystems. *Developments in Environmental Science*, *8*, 289-316.

Beverly, J. L. & Bothwell, P. (2011). Wildfire evacuations in Canada 1980–2007. *Natural Hazards*, *59*(1), 571-596.

Bilal, M., Nichol, J. E., Bleiweiss, M. P. & Dubois, D. (2013). A simplified high resolution MODIS Aerosol Retrieval Algorithm (SARA) for use over mixed surfaces. *Remote Sensing of Environment*, *136*, 135-145.

Bilal, M., Nichol, J. E. & Wang, L. (2017). New customized methods for improvement of the MODIS C6 Dark Target and Deep Blue merged aerosol product. *Remote Sensing of Environment*, *197*, 115-124.

Bilal, M., Qiu, Z., Campbell, J., Spak, S., Shen, X. & Nazeer, M. (2018). A new MODIS C6 Dark Target and Deep Blue merged aerosol product on a 3 km spatial grid. *Remote Sensing*, *10*(3), 463.

Black, C., Tesfaigzi, Y., Bassein, J. A. & Miller, L. A. (2017). Wildfire smoke exposure and human health: Significant gaps in research for a growing public health issue. *Environmental Toxicology and Pharmacology*, *55*, 186-195.

Breiman, L. (2001). Random forests. *Machine Learning*, *45*(1), 5-32.

Brunsdon, C., Fotheringham, A. S. & Charlton, M. E. (1996). Geographically weighted regression: a method for exploring spatial nonstationarity. *Geographical Analysis*, *28*(4), 281-298.

Campanelli, M., Estelles, V., Diemoz, H., Kouremeti, N., Kazadzis, S., Becker, R. & Vergari, S. (2016). The SKYNET radiometer network: aerosol optical depth retrieval performance at the FRC-IV campaign and long-term comparison against GAW-PFR and AERONET standard instruments. https://www.wmo.int/pages/prog/www/IMOP/publications/IOM_125_TECO_2016/Session_3/P3(29)_Campanelli.pdf. Last accessed on April 12, 2019.

Che, H., Zhang, X., Li, Y., Zhou, Z. & Qu, J. J. (2007). Horizontal visibility trends in China 1981–2005. *Geophysical Research Letters*, *34*(24), L24706.

Che, H. Z., Shi, G. Y., Uchiyama, A., Yamazaki, A., Chen, H., Goloub, P. & Zhang, X. (2008). Intercomparison between aerosol optical properties by a PREDE skyradiometer and CIMEL sunphotometer over Beijing, China. *Atmospheric Chemistry and Physics*, *8*(12), 3199-3214.

Chen, S., Russell, L. M., Cappa, C. D., Zhang, X., Kleeman, M. J., Kumar, A. & Ramanathan, V. (2019). Comparing black and brown carbon absorption from AERONET and surface measurements at wintertime Fresno. *Atmospheric Environment*, *199*, 164-176.

Chen, Y., Qin, H. & Zhou, Z. (2014). A comparative study on multi-regression analysis and bp neural network of PM2.5 index. In *2014 10th International Conference on Natural Computation (ICNC)*, 155-159.

Choi, M., Kim, J., Lee, J., Kim, M., Park, Y. J., Jeong, U. & Song, C. H. (2016). GOCI Yonsei Aerosol Retrieval (YAER) algorithm and validation during the DRAGON-NE Asia 2012 campaign. *Atmospheric Measurement Techniques*, *9*(3), 1377-1398.

Chu, D. A. (2006). Analysis of the relationship between MODIS aerosol optical depth and PM 2.5 in the summertime US. In *Remote Sensing of Aerosol and Chemical Gases, Model Simulation/Assimilation, and Applications to Air Quality*, *6299,* 629903.

Chu, D. A., Kaufman, Y. J., Ichoku, C., Remer, L. A., Tanré, D. & Holben, B. N. (2002). Validation of MODIS aerosol optical depth retrieval over land. *Geophysical Research Letters*, *29*(12), MOD2-1.

Chu, Y., Liu, Y., Li, X., Liu, Z., Lu, H., Lu, Y. & Liu, F. (2016). A review on predicting ground PM2.5 concentration using satellite aerosol optical depth. *Atmosphere*, *7*(10), 129.

Cordero, L., Wu, Y., Gross, B. M. & Moshary, F. (2013). Assessing satellite AOD based and WRF/CMAQ output PM2.5 estimators. In *Sensing Technologies for Global Health, Military Medicine, and Environmental Monitoring III*, *8723,* 872319.

Crouse, D. L., Philip, S., van Donkelaar, A., Martin, R. V., Jessiman, B., Peters, P. A. & Burnett, R. T. (2016). A new method to jointly estimate the mortality risk of long-term exposure to fine particulate matter and its components. *Scientific Reports*, *6*, 18916.

Dabek-Zlotorzynska, E., Dann, T. F., Martinelango, P. K., Celo, V., Brook, J. R., Mathieu, D. & Austin, C. C. (2011). Canadian National Air Pollution Surveillance (NAPS) PM2.5 speciation program: Methodology and PM2.5 chemical composition for the years 2003–2008. *Atmospheric Environment*, *45*(3), 673-686.

de Leeuw, G., Sogacheva, L., Rodriguez, E., Kolmonen, P., Virtanen, T. & Saponaro, G. (2016). Aerosol retrieval using the (Advanced) Along Track Scanning Radiometer. *Kaufman Symposium.* https://aerocenter.gsfc.nasa.gov/uploads/images_db/deLeeuw-KaufmanSymp2016.pdf. Last accessed on April 12, 2019.

de Leeuw, G., Sogacheva, L., Rodriguez, E., Kourtidis, K., Georgoulias, A. K., Alexandri, G. & Xue, Y. (2018). Two decades of satellite observations of AOD over mainland China using ATSR-2, AATSR and MODIS/Terra: data set evaluation and large-scale patterns. *Atmospheric Chemistry and Physics*, *18*(3), 1573.

Dark Target Aerosol Retrieval Algorithm. (n.d.). *Modifications for the 3 km algorithm.* https://darktarget.gsfc.nasa.gov/algorithm/land-3. Last accessed on April 12, 2019.

Department for Environment Food & Rural Affairs. (2016). *Public Health: Sources and Effects of PM2.5*. https://laqm.defra.gov.uk/public-health/pm25.html. Last accessed on April 12, 2019.

Dreessen, J., Sullivan, J. & Delgado, R. (2016). Observations and impacts of transported Canadian wildfire smoke on ozone and aerosol air quality in the Maryland region on June 9–12, 2015. *Journal of the Air & Waste Management Association*, *66*(9), 842-862.

Du, C., Liu, S., Yu, X., Li, X., Chen, C., Peng, Y. & Wang, F. (2013). Urban boundary layer height characteristics and relationship with particulate matter mass concentrations in Xi'an, central China. *Aerosol Air Quality Research*, *13*(5), 1598-1607.

EARTHDATA. (n.d.). *SeaWiFS.* https://oceancolor.gsfc.nasa.gov/data/seawifs/. Last accessed on April 12, 2019.

Environment and Climate change Canada. (2016). Canadian Environmental Sustainability Indicators: Air Quality. http://www.ec.gc.ca/indicateurs-indicators/7DCC2250-A982-4286-B466-70681EBC994B/AirQuality_EN.pdf. Last accessed on April 12, 2019.

Environment and Climate Change Canada. (2017). *Air pollution: drivers and impacts.* http://www.ec.gc.ca/indicateurs-indicators/default.asp?lang=en&n=D189C09D-1. Last accessed on April 12, 2019.

Environment and Natural Resources. (2013). *National air pollution surveillance program.* https://www.canada.ca/en/environment-climate-change/services/air-pollution/monitoring-networks-data/national-air-pollution-program.html. Last accessed on April 12, 2019.

EPA. (2017). *Introduction to indoor air pollution.* https://www.epa.gov/indoor-air-quality-iaq/introduction-indoor-air-quality. Last accessed on April 12, 2019.

EPA. (2018). *Criteria air pollutants.* https://www.epa.gov/criteria-air-pollutants. Last accessed on April 12, 2019.

Etchie, T. O., Sivanesan, S., Adewuyi, G. O., Krishnamurthi, K., Rao, P. S., Etchie, A. T. & Pillarisetti, A. (2017). The health burden and economic costs averted by ambient PM2.5 pollution reductions in Nagpur, India. *Environment International*, 102, 145-156.

Fan, A., Chen, W., Liang, L., Sun, W., Lin, Y., Che, H. & Zhao, X. (2017). Evaluation and Comparison of Long-Term MODIS C5. 1 and C6 Products against AERONET Observations over China. *Remote Sensing*, *9*(12), 1269.

Feng, S., Gao, D., Liao, F., Zhou, F. & Wang, X. (2016). The health effects of ambient PM2.5 and potential mechanisms. *Ecotoxicology and Environmental Safety*, *128*, 67-74.

Freemantle, J., O'Neill, N., Royer, A., McArthur, B. & Abboud, I. (2005). AEROCAN: The Canadian Sunphotometer Network. In *Remote Sensing of Atmospheric Aerosols, 2005. IEEE Workshop on* 32-35.

Fuzzi, S., Baltensperger, U., Carslaw, K., Decesari, S., Denier Van Der Gon, H., Facchini, M. C. & Nemitz, E. (2015). Particulate matter, air quality and climate: lessons learned and future needs. *Atmospheric Chemistry and Physics*, *15*(14), 8217-8299.

Gao, L., Li, J., Chen, L., Zhang, L. & Heidinger, A. K. (2016). Retrieval and validation of atmospheric aerosol optical depth from AVHRR over China. *IEEE Transactions on Geoscience and Remote Sensing*, *54*(11), 6280-6291.

Garay, M. J., Kalashnikova, O. V. & Bull, M. A. (2017). Development and assessment of a higher-spatial-resolution (4.4 km) MISR aerosol optical depth product using AERONET-DRAGON data. *Atmospheric Chemistry and Physics*, *17*(8), 5095-5106.

Ghoussoub, M. (2017). As evacuation orders are downgraded and evacuees return home, the situation remains unpredictable. *CBC News.* https://www.cbc.ca/news/canada/british-columbia/b-c-

surpasses-worst-wildfire-season-on-record-and-threat-is-far-from-over-1.4249435. Last accessed on April 12, 2019.

GOES R series. (n.d.). *Baseline product: aerosol optical depth.* https://www.goes-r.gov/products/baseline-aerosol-opt-depth.html. Last accessed on April 12, 2019.

Gralewicz, N. J., Nelson, T. A. & Wulder, M. A. (2012). Factors influencing national scale wildfire susceptibility in Canada. *Forest Ecology and Management*, *265*, 20-29.

Grell, G. A., Peckham, S. E., Schmitz, R., McKeen, S. A., Frost, G., Skamarock, W. C. & Eder, B. (2005). Fully coupled "online" chemistry within the WRF model. *Atmospheric Environment*, *39*(37), 6957-6975.

Grivas, G., Cheristanidis, S., Chaloulakou, A., Koutrakis, P. & Mihalopoulos, N. (2018). Elemental composition and source apportionment of fine and coarse particles at traffic and urban background locations in Athens, Greece. *Aerosol and Air Quality Research*, *18*, 1642-1659.

Grover, B. D., Kleinman, M., Eatough, N. L., Eatough, D. J., Hopke, P. K., Long, R. W. & Ambs, J. L. (2005). Measurement of total PM2.5 mass (nonvolatile plus semivolatile) with the Filter Dynamic Measurement System tapered element oscillating microbalance monitor. *Journal of Geophysical Research: Atmospheres*, *110,* D07S03.

Gupta, P., Christopher, S. A., Wang, J., Gehrig, R., Lee, Y. C. & Kumar, N. (2006). Satellite remote sensing of particulate matter and air quality assessment over global cities. *Atmospheric Environment*, *40*(30), 5880-5892.

Gupta, P. & Christopher, S. A. (2009). Particulate matter air quality assessment using integrated surface, satellite, and meteorological products: Multiple regression approach. *Journal of Geophysical Research: Atmospheres*, *114*, D14205.

Gupta, P., Remer, L. A., Levy, R. C. & Mattoo, S. (2018). Validation of MODIS 3 km land aerosol optical depth from NASA's EOS Terra and Aqua missions. *Atmospheric Measurement Techniques*, *11*(5), 3145.

Han, Y., Wu, Y., Wang, T., Zhuang, B., Li, S. & Zhao, K. (2015). Impacts of elevated-aerosol-layer and aerosol type on the correlation of AOD and particulate matter with ground-based and satellite measurements in Nanjing, southeast China. *Science of the Total Environment*, *532*, 195-207.

Hauck, H., Berner, A., Gomiscek, B., Stopper, S., Puxbaum, H., Kundi, M. & Preining, O. (2004). On the equivalence of gravimetric PM data with TEOM and beta-attenuation measurements. *Journal of Aerosol Science*, *35*(9), 1135-1149.

Hauser, A., Oesch, D. & Wunderle, S. (2004). NOAA AVHRR derived Aerosol Optical Depth (AOD) over Land: A comparison with AERONET data. *Optica Puray Aplicada*, *37*, 3131-3135.

Health Canada. (2017). *Health impacts of air pollution in Canada: an estimation of premature mortalities.* http://publications.gc.ca/site/archivee-archived.html?url=http://publications.gc.ca/collections/collection_2018/sc-hc/H144-51-2017-eng.pdf. Last accessed on April 12, 2019.

Hernandez, R. A. (2015). Prevention and control of air pollution in China: a research agenda for science and technology studies. *SAPI EN. S. Surveys and Perspectives Integrating Environment and Society*, *8*(1), 1734-1742.

Hogrefe, C. (2012). Emissions versus climate change. https://cfpub.epa.gov/si/si_public_file_download.cfm?p_download_id=508126. Last accessed on April 12, 2019.

Hong Kong Observatory. (2016). *Polar-orbiting meteorological satellite images.* http://gb.weather.gov.hk/m/article_e.htm?title=ele_00203. Last accessed on April 12, 2019.

Holben, B. N., Eck, T. F., Slutsker, I., Tanre, D., Buis, J. P., Setzer, A. & Lavenu, F. (1998). AERONET—A federated instrument network and data archive for aerosol characterization. *Remote Sensing of Environment*, *66*(1), 1-16.

Holben, B. N., Eck, T., Schafer, J., Giles, D. & Sorokin, M. (2011). Distributed Regional Aerosol Gridded Observation Networks (DRAGON) White Paper. https://aeronet.gsfc.nasa.gov/new_web/Documents/DRAGON_White_Paper_A_system_of_experiment.pdf. Last accessed on April 12, 2019.

Hsu, N. C., Gautam, R., Sayer, A. M., Bettenhausen, C., Li, C., Jeong, M. J. & Holben, B. N. (2012). Global and regional trends of aerosol optical depth over land and ocean using SeaWiFS measurements from 1997 to 2010. *Atmospheric Chemistry. 12(*17), 8037-8053.

Hsu, N. C., Jeong, M. J., Bettenhausen, C., Sayer, A. M., Hansell, R., Seftor, C. S. & Tsay, S. C. (2013). Enhanced Deep Blue aerosol retrieval algorithm: The second generation. *Journal of Geophysical Research: Atmospheres*, 118(16), 9296-9315.

Hsu, N. C., Lee, J., Sayer, A. M., Carletta, N., Chen, S. H., Tucker, C. J. & Tsay, S. C. (2017). Retrieving near-global aerosol loading over land and ocean from AVHRR. *Journal of Geophysical Research: Atmospheres*, *122*(18), 9968-9989.

Hsu, N. C., Tsay, S. C., King, M. D. & Herman, J. R. (2004). Aerosol properties over bright-reflecting source regions. *IEEE Transactions on Geoscience and Remote Sensing*, *42*(3), 557-569.

Hu, X., Waller, L. A., Al-Hamdan, M. Z., Crosson, W. L., Estes Jr, M. G., Estes, S. M. & Liu, Y. (2013). Estimating ground-level PM2.5 concentrations in the southeastern US using geographically weighted regression. *Environmental Research*, *121*, 1-10.

Hu, X., Waller, L. A., Lyapustin, A., Wang, Y., Al-Hamdan, M. Z., Crosson, W. L. & Liu, Y. (2014). Estimating ground-level PM2.5 concentrations in the Southeastern United States using MAIAC AOD retrievals and a two-stage model. *Remote Sensing of Environment*, *140*, 220-232.

Hystad, P., Demers, P. A., Johnson, K. C., Brook, J., van Donkelaar, A., Lamsal, L. & Brauer, M. (2012). Spatiotemporal air pollution exposure assessment for a Canadian population-based lung cancer case-control study. *Environmental Health*, *11*(1), 22.

Hystad, P., Setton, E., Cervantes, A., Poplawski, K., Deschenes, S., Brauer, M. & Demers, P. (2011). Creating national air pollution models for population exposure assessment in Canada. *Environmental Health Perspectives*, *119*(8), 1123-1129.

Jayarathne, T., Stockwell, C. E., Bhave, P. V., Praveen, P. S., Rathnayake, C. M., Islam, M. & DeCarlo, P. F. (2018). Nepal Ambient Monitoring and Source Testing Experiment (NAMaSTE): emissions of particulate matter from wood-and dung-fueled cooking fires, garbage and crop residue burning, brick kilns, and other sources. *Atmospheric Chemistry and Physics*, *18*(3), 2259-2286.

Jerez, S. B., Zhang, Y., McClure, J. W., Jacobson, L., Heber, A., Hoff, S. & Beasley, D. (2006). Comparison of measured total suspended particulate matter concentrations using tapered element oscillating microbalance and a total suspended particulate sampler. *Journal of the Air & Waste Management Association*, *56*(3), 261-270.

Jiang, P., Yang, J., Huang, C. & Liu, H. (2018). The contribution of socioeconomic factors to PM2.5 pollution in urban China. *Environmental Pollution*, *233*, 977-985.

Jiang, W., Wang, Y., Tsou, M. H. & Fu, X. (2015). Using social media to detect outdoor air pollution and monitor air quality index (AQI): a geo-targeted spatiotemporal analysis framework with Sina Weibo (Chinese Twitter). *PloS one*, *10*(10), e0141185.

Kahn, R. A., Gaitley, B. J., Garay, M. J., Diner, D. J., Eck, T. F., Smirnov, A. & Holben, B. N. (2010). Multiangle Imaging SpectroRadiometer global aerosol product assessment by comparison with the Aerosol Robotic Network. *Journal of Geophysical Research: Atmospheres*, *115,* D23209.

Kanada, M., Dong, L., Fujita, T., Fujii, M., Inoue, T., Hirano, Y. & Geng, Y. (2013). Regional disparity and cost-effective SO_2 pollution control in China: A case study in 5 mega-cities. *Energy policy*, *61*, 1322-1331.

Karagulian, F., Belis, C. A., Dora, C. F. C., Prüss-Ustün, A. M., Bonjour, S., Adair-Rohani, H. & Amann, M. (2015). Contributions to cities' ambient particulate matter (PM): A systematic review of local source contributions at global level. *Atmospheric Environment*, *120*, 475-483.

Karagulian, F., Belis, C. A., Lagler, F., Barbiere, M. & Gerboles, M. (2012). Evaluation of a portable nephelometer against the Tapered Element Oscillating Microbalance method for monitoring PM 2.5. *Journal of Environmental Monitoring*, *14*(8), 2145-2153.

Kaskaoutis, D. G., Sifakis, N., Retalis, A. & Kambezidis, H. D. (2010). Aerosol monitoring over Athens using satellite and ground-based measurements. *Advances in Meteorology*, *2010*(5), 147910.

Kazadzis, S., Kouremeti, N., Diémoz, H., Gröbner, J., Forgan, B. W., Campanelli, M. & Cuevas Agulló, E. (2018). Results from the Fourth WMO Filter Radiometer Comparison for aerosol optical depth measurements. *Atmospheric Chemistry and Physics, 18,* 3185-3201.

Khanna, I., Khare, M., Gargava, P. & Khan, A. A. (2018). Effect of PM2.5 chemical constituents on atmospheric visibility impairment. *Journal of the Air & Waste Management Association*, *68*(5), 430-437.

Kloog, I., Koutrakis, P., Coull, B. A., Lee, H. J. & Schwartz, J. (2011). Assessing temporally and spatially resolved PM2.5 exposures for epidemiological studies using satellite aerosol optical depth measurements. *Atmospheric Environment*, *45*(35), 6267-6275.

Kolmonen, P., Sogacheva, L., Virtanen, T. H., de Leeuw, G. & Kulmala, M. (2016). The ADV/ASV AATSR aerosol retrieval algorithm: current status and presentation of a full-mission AOD dataset. *International Journal of Digital Earth*, *9*(6), 545-561.

Kulkarni, P., Baron, P. A. & Willeke, K. (Eds.). (2011). *Aerosol Measurement: Principles, Techniques, and Applications*. John Wiley & Sons. https://onlinelibrary.wiley.com/doi/book/10.1002/9781118001684. Last accessed on April 12, 2019.

Kumar, N., Chu, A. & Foster, A. (2007). An empirical relationship between PM2.5 and aerosol optical depth in Delhi Metropolitan. *Atmospheric Environment*, *41*(21), 4492-4503.

Kumar, P., Fennell, P., Langley, D. & Britter, R. (2008). Pseudo-simultaneous measurements for the vertical variation of coarse, fine and ultrafine particles in an urban street canyon. *Atmospheric Environment*, *42*(18), 4304-4319.

Kumar, S., Devara, P. C. S., Dani, K. K., Sonbawne, S. M. & Saha, S. K. (2011). Sun-sky radiometer–derived column-integrated aerosol optical and physical properties over a tropical urban station during 2004–2009. *Journal of Geophysical Research: Atmospheres*, *116,* D10201.

Kunzli, N., Avol, E., Wu, J., Gauderman, W. J., Rappaport, E., Millstein, J. & Lurmann, F. (2006). Health effects of the 2003 Southern California wildfires on children. *American Journal of Respiratory and Critical Care Medicine*, *174*(11), 1221-1228.

LAADS DAAC. (2018a). *Envisat Medium Resolution Imaging Spectrometer (MERIS).* https://ladsweb.modaps.eosdis.nasa.gov/missions-and-measurements/meris/. Last accessed on April 12, 2019.

LAADS DAAC. (2018b). *Aerosol products.* https://ladsweb.modaps.eosdis.nasa.gov/missions-and-measurements/products/aerosol/MOD04_3K/. Last accessed on April 12, 2019.

Lee, H. J., Liu, Y., Coull, B. A., Schwartz, J. & Koutrakis, P. (2011). A novel calibration approach of MODIS AOD data to predict PM 2.5 concentrations. *Atmospheric Chemistry & Physics*, *11*(15), 7991-8002.

Lee, K. H., Li, Z., Cribb, M. C., Liu, J., Wang, L., Zheng, Y. & Li, B. (2010). Aerosol optical depth measurements in eastern China and a new calibration method. *Journal of Geophysical Research: Atmospheres*, *115*, D00K11.

Lee, M., Kloog, I., Chudnovsky, A., Lyapustin, A., Wang, Y., Melly, S. & Schwartz, J. (2016). Spatiotemporal prediction of fine particulate matter using high-resolution satellite images in the Southeastern US 2003–2011. *Journal of Exposure Science and Environmental Epidemiology*, *26*(4), 377.

Li, S., Feng, K. & Li, M. (2017). Identifying the main contributors of air pollution in Beijing. *Journal of Cleaner Production*, *163*, S359-S365.

Li, S., Zhai, L., Zou, B., Sang, H. & Fang, X. (2017). A generalized additive model combining principal component analysis for PM2.5 concentration estimation. *ISPRS International Journal of Geo-Information*, *6*(8), 248.

Li, X. F., Zhang, M. J., Wang, S. J., Zhao, A. F. & Ma, Q. (2012). Variation characteristics and influencing factors of air pollution index in China. *Huan Jing Ke Xue*, *33*(6), 1936-1943.

Li, Y. (2016). *Estimating PM2.5 in the Beijing-Tianjin-Hebei Region Using MODIS AOD Products from 2014 to 2015* (Master's thesis, University of Waterloo). https://uwspace.uwaterloo.ca/handle/10012/10494. Last accessed on April 12, 2019.

Lin, C., Li, Y., Yuan, Z., Lau, A. K., Li, C. & Fung, J. C. (2015). Using satellite remote sensing data to estimate the high-resolution distribution of ground-level PM2.5. *Remote Sensing of Environment*, *156*, 117-128.

Liu, H., Remer, L. A., Huang, J., Huang, H. C., Kondragunta, S., Laszlo, I. & Jackson, J. M. (2014). Preliminary evaluation of S-NPP VIIRS aerosol optical thickness. *Journal of Geophysical Research: Atmospheres*, *119*(7), 3942-3962.

Liu, M. (2018). A satellite-based theoretical method for ground PM2.5 retrieval method in China. *In press.*

Liu, Y., Koutrakis, P. & Kahn, R. (2007). Estimating fine particulate matter component concentrations and size distributions using satellite-retrieved fractional aerosol optical depth: Part 1—Method development. *Journal of the Air & Waste Management Association*, *57*(11), 1351-1359.

Liu, Y., Sarnat, J. A., Kilaru, V., Jacob, D. J. & Koutrakis, P. (2005). Estimating ground-level PM2.5 in the eastern United States using satellite remote sensing. *Environmental Science & Technology*, *39*(9), 3269-3278.

Liu, J. C., Wilson, A., Mickley, L. J., Dominici, F., Ebisu, K., Wang, Y. & Anderson, G. B. (2017). Wildfire-specific Fine Particulate Matter and Risk of Hospital Admissions in Urban and Rural Counties. *Epidemiology (Cambridge, Mass.)*, *28*(1), 77-85.

Liu, Y., Sarnat, J. A., Kilaru, V., Jacob, D. J. & Koutrakis, P. (2005). Estimating ground-level PM2.5 in the eastern United States using satellite remote sensing. *Environmental Science & Technology*, *39*(9), 3269-3278.

Livingston, J. M., Redemann, J., Shinozuka, Y., Johnson, R., Russell, P. B., Zhang, Q. & Ramachandran, S. (2014). Comparison of MODIS 3 km and 10 km resolution aerosol optical depth retrievals over land with airborne sunphotometer measurements during ARCTAS summer 2008. *Atmospheric Chemistry and Physics*, *14*(4), 2015-2038.

Lu, X., Lin, C., Li, W., Chen, Y., Huang, Y., Fung, J. C. & Lau, A. K. (2019). Analysis of the adverse health effects of PM2.5 from 2001 to 2017 in China and the role of urbanization in aggravating the health burden. *Science of the Total Environment*, *652*, 683-695.

Lyapustin, A. & Wang, Y. (2012). Multi-Angle Implementation of Atmospheric Correction (MAIAC) Algorithm. *Remote Sensing of Environment, 127,* 385-393.

Lyapustin, A., Wang, Y., Levy, R. C., Remer, L. A., Hsu, C. & Reid, J. S. (2010). A comparison between MODIS Dark Target, Deep Blue and MAIAC Aerosol Algorithms over Land. In *AGU Fall Meeting Abstracts*.

Ma, Z., Hu, X., Huang, L., Bi, J. & Liu, Y. (2014). Estimating ground-level PM2.5 in China using satellite remote sensing. *Environmental Science and Technology*, *48*(13), 7436-7444.

Ma, Z., Hu, X., Sayer, A. M., Levy, R., Zhang, Q., Xue, Y. & Liu, Y. (2015). Satellite-based spatiotemporal trends in PM2.5 concentrations: China, 2004–2013. *Environmental Health Perspectives*, *124*(2), 184-192.

Maji, K. J., Ye, W. F., Arora, M. & Nagendra, S. S. (2018). PM2.5-related health and economic loss assessment for 338 Chinese cities. *Environment International*, *121*, 392-403.

Mao, L., Qiu, Y., Kusano, C. & Xu, X. (2012). Predicting regional space–time variation of PM 2.5 with land-use regression model and MODIS data. *Environmental Science and Pollution Research*, *19*(1), 128-138.

Martins, N. R. & da Graça, G. C. (2018). Impact of PM2.5 in indoor urban environments: A review. *Sustainable Cities and Society*, *42*, 259-275.

Martonchik, J. V., Diner, D. J., Kahn, R., Gaitley, B. & Holben, B. N. (2004). Comparison of MISR and AERONET aerosol optical depths over desert sites. *Geophysical Research Letters*, *31*, L16102.

McPhetres, A. & Aggarwal, S. (2018). An Evaluation of MODIS-Retrieved Aerosol Optical Depth over AERONET Sites in Alaska. *Remote Sensing*, *10*(9), 1384.

Mei, L. L., Xue, Y., Kokhanovsky, A. A., von Hoyningen-Huene, W., de Leeuw, G. & Burrows, J. P. (2014). Retrieval of aerosol optical depth over land surfaces from AVHRR data. *Atmospheric Measurement Techniques*, *7*(8), 2411-2420.

Metro Vancouver (2018). *Metro Vancouver ambient air quality objectives.* http://www.metrovancouver.org/services/air-quality/AirQualityPublications/CurrentAmbientAirQualityObjectives.pdf. Last accessed on April 12, 2019.

Ministry of Forest. (n.d.). *British Columbia's forests: a geographical snapshot*. https://www.for.gov.bc.ca/hfd/pubs/docs/mr/mr112/BC_Forests_Geographical_Snapshot.pdf. Last accessed on April 12, 2019.

Mirzaei, M., Bertazzon, S. & Couloigner, I. (2018). Modeling Wildfire Smoke Pollution by Integrating Land Use Regression and Remote Sensing Data: Regional Multi-Temporal Estimates for Public Health and Exposure Models. *Atmosphere*, *9*(9), 335.

Mirzaei, M., Bertazzon, S. & Couloigner, I. (2018). OLS and GWR LUR models of wildfire smoke using remote sensing and spatiotemporal data in Alberta. *Spatial Knowledge and Information Canada, 7*(2), 3.

Mitchell, R. M. & Forgan, B. W. (2003). Aerosol measurement in the Australian outback: Intercomparison of sun photometers. *Journal of Atmospheric and Oceanic Technology*, *20*(1), 54-66.

MODIS Atmosphere. (2017). *Collection 6.1 (061) upgrade.* https://modis-atmosphere.gsfc.nasa.gov/documentation/collection-61. Last accessed on April 12, 2019.

Mölders, N., Tran, H. N., Cahill, C. F., Leelasakultum, K. & Tran, T. T. (2012). Assessment of WRF/Chem PM2.5 forecasts using mobile and fixed location data from the Fairbanks, Alaska winter 2008/09 field campaign. *Atmospheric Pollution Research*, *3*(2), 180-191.

Mukherjee, A. & Agrawal, M. (2017). A global perspective of fine particulate matter pollution and its health effects. In *Reviews of Environmental Contamination and Toxicology, 244*, 5-51.

Munchak, L. A., Levy, R. C., Mattoo, S., Remer, L. A., Holben, B. N., Schafer, J. S. & Ferrare, R. A. (2013). MODIS 3 km aerosol product: applications over land in an urban/suburban region. https://www.academia.edu/20361787/MODIS_3_km_aerosol_product_applications_over_land_in_an_urban_suburban_region. Last accessed on April 12, 2019.

Murray, N., Chang, H. H., Holmes, H. & Liu, Y. (2018). Combining satellite imagery and numerical model simulation to estimate ambient air pollution: An ensemble averaging approach. https://arxiv.org/abs/1802.03077. Last accessed on April 12, 2019.

NASA. (n.d.). *What is the difference between dark target and deep blue?* https://darktarget.gsfc.nasa.gov/content/what-difference-between-dark-target-and-deep-blue. Last accessed on April 12, 2019.

NASA Earth Observatory. (n.d.). *Aerosol optical depth.* https://earthobservatory.nasa.gov/global-maps/MODAL2_M_AER_OD. Last accessed on April 12, 2019.

NASA Goddard Space Flight Center. (n.d.). *AEROSOL ROBOTIC NETWORK*. https://aeronet.gsfc.nasa.gov/. Last accessed on April 12, 2019.

NASA MODIS. (n.d.). *Specifications.* https://modis.gsfc.nasa.gov/about/specifications.php. Last accessed on April 12, 2019.

National Snow & Ice Data Center. (n.d.). *Terra vs. Aqua.* https://nsidc.org/data/modis/terra_aqua_differences. Last accessed on April 12, 2019.

Nichol, J. & Bilal, M. (2016). Validation of MODIS 3 km resolution aerosol optical depth retrievals over Asia. *Remote Sensing*, *8*(4), 328.

NSW Government. (2013). *Outdoor air pollution.* https://www.health.nsw.gov.au/environment/air/Pages/outdoor-air-pollution.aspx. Last accessed on April 12, 2019.

Nyeki, S., Wehrli, C., Gröbner, J., Kouremeti, N., Wacker, S., Labuschagne, C. & Brunke, E. G. (2015). The GAW-PFR aerosol optical depth network: The 2008–2013 time series at Cape Point Station, South Africa. *Journal of Geophysical Research: Atmospheres*, *120*(10), 5070-5084.

Ontario Ministry of the Environment, Conservation and Parks. (2010). *Fine particulate matter.* http://www.airqualityontario.com/science/pollutants/particulates.php. Last accessed on April 12, 2019.

Park, M. E., Song, C. H., Park, R. S., Lee, J., Kim, J., Lee, S. & Lee, S. S. (2014). New approach to monitor transboundary particulate pollution over Northeast Asia. *Atmospheric Chemistry and Physics*, *14*(2), 659-674.

Pew, K. L. & Larsen, C. P. S. (2001). GIS analysis of spatial and temporal patterns of human-caused wildfires in the temperate rain forest of Vancouver Island, Canada. *Forest Ecology and Management*, *140*(1), 1-18.

Qu, Y., Han, Y., Wu, Y., Gao, P. & Wang, T. (2017). Study of PBLH and its correlation with particulate matter from one-year observation over Nanjing, southeast China. *Remote Sensing*, *9*(7), 668.

Queensland Government. (2017). *Tapered element oscillating microbalance.* https://www.qld.gov.au/environment/pollution/monitoring/air/air-monitoring/measuring/oscillating-microbalance. Last accessed on April 12, 2019.

Raaschou-Nielsen, O., Beelen, R., Wang, M., Hoek, G., Andersen, Z. J., Hoffmann, B. & Nieuwenhuijsen, M. (2016). Particulate matter air pollution components and risk for lung cancer. *Environment International*, *87*, 66-73.

Remer, L. A., Kaufman, Y. J., Tanré, D., Mattoo, S., Chu, D. A., Martins, J. V. & Eck, T. F. (2005). The MODIS aerosol algorithm, products, and validation. *Journal of the Atmospheric Sciences*, *62*(4), 947-973.

Requia, W. J., Adams, M. D. & Koutrakis, P. (2017). Association of PM2.5 with diabetes, asthma, and high blood pressure incidence in Canada: A spatiotemporal analysis of the impacts of the energy generation and fuel sales. *Science of the Total Environment*, *584,* 1077-1083.

Safarpour, S., Abdullah, K., San Lim, H. & Dadras, M. (2014). Accuracy assessment of Terra-MODIS aerosol optical depth retrievals. In *IOP Conference Series: Earth and Environmental Science*, 20(1), 012059.

Sano, I., Mukai, S., Yamano, M., Takamura, T., Nakajima, T. & Holben, B. (2003). Calibration and validation of retrieved aerosol properties based on AERONET and SKYNET. *Advances in Space Research*, *32*(11), 2159-2164.

Sayer, A. M., Hsu, N. C., Bettenhausen, C., Ahmad, Z., Holben, B. N., Smirnov, A. & Zhang, J. (2012). SeaWiFS Ocean Aerosol Retrieval (SOAR): Algorithm, validation, and comparison with other data sets. *Journal of Geophysical Research: Atmospheres*, *117*, D03206.

Sayer, A. M., Hsu, N. C., Bettenhausen, C. & Jeong, M. J. (2013). Validation and uncertainty estimates for MODIS Collection 6 "Deep Blue" aerosol data. *Journal of Geophysical Research: Atmospheres*, *118*(14), 7864-7872.

Sayer, A. M., Hsu, N. C., Lee, J., Bettenhausen, C., Kim, W. V. & Smirnov, A. (2018). Satellite Ocean Aerosol Retrieval (SOAR) algorithm extension to S-NPP VIIRS as part of the "Deep Blue" Aerosol Project. *Journal of Geophysical Research: Atmospheres*, *123*(1), 380-400.

Sayer, A. M., Munchak, L. A., Hsu, N. C., Levy, R. C., Bettenhausen, C. & Jeong, M. J. (2014). MODIS Collection 6 aerosol products: Comparison between Aqua's e-Deep Blue, Dark Target, and "merged" data sets, and usage recommendations. *Journal of Geophysical Research: Atmospheres*, *119*(24), 13-965.

Schweizer, D., Cisneros, R. & Shaw, G. (2016). A comparative analysis of temporary and permanent beta attenuation monitors: The importance of understanding data and equipment limitations when creating PM2.5 air quality health advisories. *Atmospheric Pollution Research*, *7*(5), 865-875.

Shao, P., Xin, J., An, J., Kong, L., Wang, B., Wang, J. & Wu, D. (2017). The empirical relationship between PM2.5 and AOD in Nanjing of the Yangtze River Delta. *Atmospheric Pollution Research*, *8*(2), 233-243.

Sioris, C. E., Abboud, I., Fioletov, V. E. & McLinden, C. A. (2017). AEROCAN, the Canadian sub-network of AERONET: Aerosol monitoring and air quality applications. *Atmospheric Environment*, *167*, 444-457.

Smirnov, A., Duarte, C. M. & Diehl, T. L. (2011). Maritime Aerosol Network as a component of AERONET-first results and comparison with global aerosol models and satellite retrievals. *Atmospheric Measurement Techniques, 4*(3), 583.

Sofowote, U. & Dempsey, F. (2015). Impacts of forest fires on ambient near–real–time PM2.5 in Ontario, Canada: Meteorological analyses and source apportionment of the July 2011–2013 episodes. *Atmospheric Pollution Research*, *6*(1), 1-10.

Sofowote, U., Su, Y., Bitzos, M. M. & Munoz, A. (2014). Improving the correlations of ambient tapered element oscillating microbalance PM2.5 data and SHARP 5030 Federal Equivalent Method in Ontario: A multiple linear regression analysis. *Journal of the Air & Waste Management Association*, *64*(1), 104-114.

Sorek-Hamer, M., Broday, D. M., Chatfield, R., Esswein, R., Stafoggia, M., Lepeule, J. & Kloog, I. (2017). Monthly analysis of PM ratio characteristics and its relation to AOD. *Journal of the Air & Waste Management Association*, *67*(1), 27-38.

Stieb, D. M., Chen, L., Beckerman, B. S., Jerrett, M., Crouse, D. L., Omariba, D. W. R. & Gilbert, N. L. (2015). Associations of pregnancy outcomes and PM2.5 in a national Canadian study. *Environmental Health Perspectives*, *124*(2), 243-249.

Su, Y., Sofowote, U., Debosz, J., White, L. & Munoz, A. (2018). Multi-year continuous PM2. 5 measurements with the federal equivalent method SHARP 5030 and comparisons to filter-based and TEOM measurements in Ontario, Canada. *Atmosphere*, *9*(5), 191.

Sundström, A. M., Kolmonen, P., Sogacheva, L. & de Leeuw, G. (2012). Aerosol retrievals over China with the AATSR dual view algorithm. *Remote Sensing of Environment*, *116*, 189-198.

Tai, A. P., Mickley, L. J. & Jacob, D. J. (2010). Correlations between fine particulate matter (PM2.5) and meteorological variables in the United States: Implications for the sensitivity of PM2.5 to climate change. *Atmospheric Environment*, *44*(32), 3976-3984.

Tao, M., Chen, L., Wang, Z., Tao, J., Che, H., Wang, X. & Wang, Y. (2015). Comparison and evaluation of the MODIS Collection 6 aerosol data in China. *Journal of Geophysical Research: Atmospheres*, *120*(14), 6992-7005.

Tian, J. & Chen, D. (2010). A semi-empirical model for predicting hourly ground-level fine particulate matter (PM2.5) concentration in southern Ontario from satellite remote sensing and ground-based meteorological measurements. *Remote Sensing of Environment*, *114*(2), 221-229.

Urbanski, S. P. (2013). Combustion efficiency and emission factors for wildfire-season fires in mixed conifer forests of the northern Rocky Mountains, US. *Atmospheric Chemistry and Physics*, *13*(14), 7241-7262.

U.S. Environmental Protection Agency. (2005). *The Tapered Element Oscillating Microbalance: A Monitor for Short-Term Measurement of Fine Aaerosol Mass Concentration.* https://cfpub.epa.gov/si/si_public_record_report.cfm?Lab=ORD&dirEntryId=44569. Last accessed on April 12, 2019.

van Donkelaar, A., Martin, R. V., Brauer, M. & Boys, B. L. (2014). Use of satellite observations for long-term exposure assessment of global concentrations of fine particulate matter. *Environmental Health Perspectives*, *123*(2), 135-143.

van Donkelaar, A., Martin, R. V., Brauer, M., Kahn, R., Levy, R., Verduzco, C. & Villeneuve, P. J. (2010). Global estimates of ambient fine particulate matter concentrations from satellite-based aerosol optical depth: development and application. *Environmental health perspectives*, *118*(6), 847-855.

Wagstrom, K. M. & Pandis, S. N. (2011). Contribution of long range transport to local fine particulate matter concerns. *Atmospheric Environment*, *45*(16), 2730-2735.

Wallace, J. & Kanaroglou, P. (2007). An investigation of air pollution in southern Ontario, Canada, with MODIS and MISR aerosol data. In *2007 IEEE International Geoscience and Remote Sensing Symposium*, 4311-4314.

Wang, B. & Chen, Z. (2016). High-resolution satellite-based analysis of ground-level PM2.5 for the city of Montreal. *Science of the Total Environment*, *541*, 1059-1069.

Wang, J. & Christopher, S. A. (2003). Intercomparison between satellite-derived aerosol optical thickness and PM2.5 mass: Implications for air quality studies. *Geophysical Research Letters*, *30*(21), 2095.

Wang, J. & Ogawa, S. (2015). Effects of meteorological conditions on PM2.5 concentrations in Nagasaki, Japan. *International Journal of Environmental Research and Public Health*, *12*(8), 9089-9101.

Wang, K., Sun, X., Zhou, Y. & Zhang, C. (2017). Validation of MODIS-Aqua Aerosol Products C051 and C006 over the Beijing-Tianjin-Hebei Region. *Atmosphere*, *8*(9), 172.

Wang, X., Parisien, M. A., Flannigan, M. D., Parks, S. A., Anderson, K. R., Little, J. M. & Taylor, S. W. (2014). The potential and realized spread of wildfires across Canada. *Global Change Biology*, *20*(8), 2518-2530.

Wang, Y., Yang, W., Han, B., Zhang, W., Chen, M. & Bai, Z. (2016). Gravimetric analysis for PM2.5 mass concentration based on year-round monitoring at an urban site in Beijing. *Journal of Environmental Sciences*, *40*, 154-160.

Wang, Y., Ying, Q., Hu, J. & Zhang, H. (2014). Spatial and temporal variations of six criteria air pollutants in 31 provincial capital cities in China during 2013–2014. *Environment International*, *73*, 413-422.

Wang, Y., Yuan, Q., Li, T., Shen, H., Zheng, L. & Zhang, L. (2019). Evaluation and comparison of MODIS Collection 6.1 aerosol optical depth against AERONET over regions in China with multifarious underlying surfaces. *Atmospheric Environment*, *200*, 280-301.

Watson, J. G., Chow, J. C., Chen, L., Kohl, S., Gasuccio, G. S., Lersch, T. L. & Langston, R. (2012). Elemental and morphological analyses of filter tape deposits from a beta attenuation monitor. *Atmospheric Research*, *106*, 181-189.

Weizhen, H., Zhengqiang, L., Yuhuan, Z., Hua, X., Ying, Z., Kaitao, L. & Yan, M. (2014). Using support vector regression to predict PM10 and PM2.5. In *IOP Conference Series: Earth and Environmental Science*, *17*(1), 012268.

WHO. (2017). *Mortality and burden of disease from ambient air pollution.* https://www.who.int/gho/phe/outdoor_air_pollution/burden/en/. Last accessed on April 12, 2019.

WHO. (2018). *Ambient (outdoor) air quality and health.* https://www.who.int/news-room/fact-sheets/detail/ambient-(outdoor)-air-quality-and-health. Last accessed on April 12, 2019.

Wu, C. F., Woodward, A., Li, Y. R., Kan, H., Balasubramanian, R., Latif, M. T. & Kim, H. (2017). Regulation of fine particulate matter (PM2.5) in the Pacific Rim: Perspectives from the APRU Global Health Program. *Air Quality, Atmosphere & Health*, *10*(9), 1039-1049.

Wu, D., Fung, J. C. H., Yao, T. & Lau, A. K. H. (2013). A study of control policy in the Pearl River Delta region by using the particulate matter source apportionment method. *Atmospheric Environment*, *76*, 147-161.

Wu, Y., Guo, J., Zhang, X. & Li, X. (2011). Correlation between PM concentrations and aerosol optical depth in eastern China based on BP neural networks. In *2011 IEEE International Geoscience and Remote Sensing Symposium*, 3308-3311.

Xiao, Q., Zhang, H., Choi, M., Li, S., Kondragunta, S., Kim, J. & Liu, Y. (2016). Evaluation of VIIRS, GOCI, and MODIS Collection 6 AOD retrievals against ground sunphotometer observations over East Asia. *Atmospheric Chemistry and Physics*, *16*(3), 1255-1269.

Xie, Y., Wang, Y., Zhang, K., Dong, W., Lv, B. & Bai, Y. (2015). Daily estimation of ground-level PM2.5 concentrations over Beijing using 3 km resolution MODIS AOD. *Environmental Science & Technology*, *49*(20), 12280-12288.

Xing, Y. F., Xu, Y. H., Shi, M. H. & Lian, Y. X. (2016). The impact of PM2.5 on the human respiratory system. *Journal of Thoracic Disease*, *8*(1), E69.

Yang, F., Wang, Y., Tao, J., Wang, Z., Fan, M., de Leeuw, G. & Chen, L. (2018). Preliminary investigation of a new ahi aerosol optical depth (AOD) retrieval algorithm and evaluation with multiple source aod measurements in China. *Remote Sensing*, *10*(5), 748.

Yang, H., Chen, W. & Liang, Z. (2017). Impact of land use on PM2.5 pollution in a representative city of middle China. *International Journal of Environmental Research and Public Health*, *14*(5), 462.

Yang, Q., Yuan, Q., Yue, L., Li, T., Shen, H. & Zhang, L. (2018). The relationships between PM2.5 and AOD in China: About and behind spatiotemporal variations. *Environmental Pollution*, *248,* 526-535.

Zhang, G., Rui, X. & Fan, Y. (2018). Critical Review of Methods to Estimate PM2.5 Concentrations within Specified Research Region. *ISPRS International Journal of Geo-Information*, *7*(9), 368.

Zhang, R., Wang, G., Guo, S., Zamora, M. L., Ying, Q., Lin, Y. & Wang, Y. (2015). Formation of urban fine particulate matter. *Chemical Reviews*, *115*(10), 3803-3855.

Zhang, Y. & Jiang, W. (2018). Pollution characteristics and influencing factors of atmospheric particulate matter (PM2.5) in Chang-Zhu-Tan area. In *IOP Conference Series: Earth and Environmental Science*, *108*(4), 042047.

Zhang, Y. & Li, Z. (2015). Remote sensing of atmospheric fine particulate matter (PM2.5) mass concentration near the ground from satellite observation. *Remote Sensing of Environment*, *160*, 252-262.

Zhang, Y. L. & Cao, F. (2015). Fine particulate matter (PM 2.5) in China at a city level. *Scientific Reports*, *5*, 14884.

Zhang, Z., Fan, M., Wu, W., Wang, Z., Tao, M., Wei, J. & Wang, Q. (2019). A simplified aerosol retrieval algorithm for Himawari-8 Advanced Himawari Imager over Beijing. *Atmospheric Environment*, *199*, 127-135.

Zheng, Y., Xue, T., Zhang, Q., Geng, G., Tong, D., Li, X. & He, K. (2017). Air quality improvements and health benefits from China's clean air action since 2013. *Environmental Research Letters*, *12*(11), 114020.

Zheng, Y., Zhang, Q., Liu, Y., Geng, G. & He, K. (2016). Estimating ground-level PM2.5 concentrations over three megalopolises in China using satellite-derived aerosol optical depth measurements. *Atmospheric Environment*, *124*, 232-242.

Zhu, Y., Smith, T. J., Davis, M. E., Levy, J., Herrick, R. & Jiang, H. (2011). Comparing Gravimetric and Real-Time Sampling of PM2.5 Concentrations Inside Truck Cabins. *Journal of Occupational and Environment Hygiene, 8*(11), 662-672.

Appendix A

Table A. Information of ground monitoring stations in BC

Station Name	EMS_ID	Longitude	Latitude	Annual Mean PM2.5 Concentrations ($\mu g/m^3$)
Abbotsford A Columbia Street	E289309	-122.3266	49.0215	6.06
Abbotsford Central	E238212	-122.3097	49.0428	6.66
Agassiz Municipal Hall	E293810	-121.762334	49.23803	7.65
Burnaby Kensington Park	310177	-122.9711	49.2794	6.47
Burnaby South	E207418	- 122.9856	49.2153	6 .58
Burns Lake Fire Centre	E225267	- 125.7643	5 4.2307	3. 89
Castlegar Zinio Park	E286369	-117.661527	4 9.3177	9. 19
Chilliwack Airport	E220891	-121.9406	49 .1561	7. 12
Colwood City Hall	E240337	-123.49278	48 .42389	5. 29
Courtenay Elementary School	E285829	-124.996222	49. 6826	5. 36
Crofton Georgia Hts	E296370	-123.637041	48.84964	5.57
Crofton Substation	E220217	-123.653929	48.87453	5.95
Duncan Cairnsmore	E277329	-123.715846	48.78485	6.76
Duncan Deykin Avenue	E234670	-123.646402	48.80255	6.64
Elk Falls Dogwood	E222520	-125.2844	50.01843	7.43
Fort St John 85th Avenue	E304550	-120.853895	56.23179	4.51

Fort St John Key Learning Centre	E299830	-120.856111	56.24472	4.72
Fort St John North Camp B_Amb	E306480	-120.9026	56.201	6.64
Fort St John Old Fort	E304470	-120.825713	56.20059	5.11
Golden Helipad	E292149	-116.966	51.2975	9.45
Grand Forks City Hall	E263701	-118.439088	49.03117	7.74
Harmac Cedar Woobank	E225377	-123.850165	49.11417	7.4
Hope Airport	E223756	-121.4994	49.3697	6.94
Horseshoe Bay	E275843	-123.2766	49.3686	5.32
Houston Firehall	M107004	-126.645	54.3972	3.89
Kamloops Aberdeen	E303935	-120.37207	50.63694	13.4
Kamloops Federal Building	605008	-120.334016	50.67477	18.33
Kelowna College	500886	-119.477367	49.86234	9.41
Kitimat Haul Road	E223616	-128.70269	54.02919	3.54
Kitimat Riverlodge	E216670	-128.671436	54.05389	3.89
Langdale Elementary	E222778	-123.479185	49.43885	12.62
Langley Central	E209178	-122.5669	49.0956	5.73
Lavington Baptist Church	E304590	-119.10674	50.23081	10.44
Mission School Works Yard	E302130	-122.311078	49.14149	8.62
Nanaimo Labieux Road	E229797	-123.99389	49.20083	5.57
Nelson Kutenai Place	E258315	-117.2952	49.4908	31.29

New Westminster Sapperton Park	E308566	-122.894487	49.22705	7.3
North Delta	E207723	-122.9017	49.1583	6.81
North Vancouver Mahon Park	E209177	-123.0836	49.3239	6.29
North Vancouver Second Narrows	310179	-123.0203	49.3017	8.28
Peace Valley Attachie Flat Upper Terrace	E304453	-121.41944	56.23121	2.91
Pitt Meadows Meadowlands School	E232244	-122.7089	49.2453	5.49
Port Alberni Elementary	E273483	-124.806628	49.26101	7.32
Port Alberni Port Authority	E310612	-124.81254	49.2278	7.8
Port Moody Rocky Point Park	310162	-122.8492	49.2808	6.68
Powell River James Thomson School	E271963	-124.5624	49.8893	2.56
Powell River Wildwood	220205	-124.558104	49.88689	3.05
Prince George 18th Avenue MAML	E309666	-122.79525	53.90682	5.72
Prince George Plaza 400	450307	-122.74194	53.91472	6.91
Prince Rupert Fairview	E312331	-130.352188	54.29262	2.32
Prince Rupert Pineridge Elementary	E312330	-130.337676	54.29855	2.39

Quesnel Senior Secondary	E208096	-122.493227	52.98169	11.86
Richmond South	E207417	-123.1083	49.1414	6.16
Smithers St Josephs	E206589	-127.177324	54.78331	4.1
Squamish Elementary	E304570	-123.15133	49.70516	8.21
Surrey East	E206271	-122.6942	49.1328	5.22
Taylor Lone Wolf Golf Course	E304685	-120.67594	56.16013	6.35
Terrace Skeena Middle School	E300350	-128.6075	54.52167	4.22
Tsawwassen	E283549	-123.082	49.0099	4.39
Valemount	E234293	-119.269821	52.83246	5.07
Vancouver International Airport #2	E232246	-123.1522	49.1864	5.4
Vanderhoof Courthouse	E269223	-124.0061	54.0163	7.02
Vernon Science Centre	E249492	-119.270723	50.26062	10.49
Victoria Topaz	E231866	-123.363165	48.44194	6.33
Whistler Meadow Park	E227431	-122.960402	50.14429	10.57
Williams Lake Columneetza School	550502	-122.150391	52.14428	14.66